TECHNISCHE UNIVERSITÄT MÜNCHEN
Fakultät für Chemie
Professur für Anorganische Chemie

Decomposition of Nitrous Oxide by Supported Transition Metal Catalysts: Structure-Activity Relationships

Xiaoqiao Zhang

Vollständiger Abdruck der von der Fakultät für Chemie der Technischen Universität München zur Erlangung des akademischen Grades eines

Doktors der Naturwissenschaften

genehmigten Dissertation

Vorsitzender:	Prof. Dr. Lukas Hintermann
Prüfer der Dissertation:	1. Prof. Dr. Klaus Köhler
	2. Hon.-Prof. Dr. Richard W. Fischer

Die Dissertation wurde am 16.07.2019 bei der Technischen Universität München eingereicht und durch die Fakultät für Chemie am 30.07.2019 angenommen.

Acknowledgements

Firstly, I would like to express my sincere gratitude to **Prof. Dr. Klaus Köhler** for giving me the opportunity to perform my PhD work in his group, for providing the challenging and interesting topic, for his supervision, guidance, help, and ongoing support throughout the years. I feel really grateful and lucky to have had him as my advisor. With his continuous support, encouragement, and immense knowledge, he provided my first exposure to the world of advanced scientific research and guided me throughout my Ph.D. work. Without his input it would not have been possible to complete this thesis.

I want to thank **Prof. Dr. Lukas Hintermann** for accepting to be my mentor.

During my work for doctoral thesis, I have obtained the supports from the students who ever worked with me. They have transferred their talents and enthusiasms into their theses or internship works. The master student **Max Johannes Hiller** is acknowledged for his master thesis work. The master student **Michael Johannes Sauer** is acknowledged for his research practical work. I thank all of the students who contributed to this work with high motivation during their bachelor's theses: **Catherine Ongko, Kim Dong Hyun, Spencer Ng Say Kiat and Sharaf Yar Khan.**

I would also like to express my thanks to the whole team for their wonderful support regarding the technical equipment (especially the Fourier-transform infrared spectroscopy) and the useful talks. I thank in particular **Dr. Chengyang Wang** who introduced and helped me to initiate my thesis project. I learned many experimental skills and knowledge from him. I would like to give the gratitude to **Dr. Oliver Thomys**, **Dr. Florian Boch** and **Franz Bannert** for their help, useful discussions and the introduction to the preparation and testing of catalysts. **Andrea Abram, Hannah Augenstein, Dr. Florian Boch, Patrick Bretzler, Tobias Bruhm, Dr. Oliver Dachwald, Dr. Christoph Dörfelt, Christoph Gnad, Dr. Carmen Haeßner** are acknowledged for supportive helps in the lab**.** My special thanks also go to **Mrs. Renate Schuhbauer-Gerl** for all her administrative work and kind help.

I want to say many thanks to **Thomas Burger** for supporting me regarding the Quantachrome devices in the CRC. I also would like to mention **Dr. Eliza Gemel** for her help regarding the complete central analytic lab.

The **China Scholarship Council (CSC)** and **TUM Graduate School** are acknowledged for the grant and the financial support in this work.

Last but not the least, I would like to thank my parents with all my heart. With their unconditional support and encouragement, my world is full of love.

Abstract

Decomposition of Nitrous Oxide by Supported Transition Metal Catalysts: Structure-Activity Relationships

Ruthenium catalysts on various supports were developed to enlighten support influence and reaction mechanism of N_2O decomposition. The metals Rh, Ru, Pd, Fe and Ni supported on cerium(IV) oxide, CeO_2, stoichiometrically reduce N_2O at room temperature after reductive pre-treatment. A catalytic reduction of N_2O by hydrogen at mild conditions is possible over Rh/CeO_2 and Ru/CeO_2 catalysts. The influence of light irradiation on N_2O decomposition of by Ru and Ag catalysts was investigated.

Zusammenfassungen

Zersetzung von Distickstoffmonoxid durch geträgerte Übergangsmetallkatalysatoren: Struktur-Aktivitäts-Beziehungen

Der Einfluss des Trägers und der Reaktionsmechanismus der N_2O-Zersetzung mit Ruthenium-Katalysatoren auf verschiedensten Trägern wurde untersucht. Die Metalle Rh, Ru, Pd, Fe und Ni auf Cer(IV)oxid reduzieren N_2O bei Raumtemperatur stöchiometrisch nach reduktiver Vorbehandlung. Katalytisch wird N_2O mit Wasserstoff unter milden Bedingungen über Rh/CeO_2 und Ru/CeO_2 reduziert. Der Einfluss von Licht auf die Zersetzung von N_2O über Ru- und Ag-Katalysatoren wurde untersucht.

Table of contents

1 Introduction 1

1.1 Origins and effects of nitrous oxide 2

1.2 N_2O Abatement Technologies 3

1.3 Catalysts for N_2O decomposition 6

1.3.1 Ruthenium Catalysts 6

1.3.2 Cerium oxide based catalysts 7

1.4 Aim and motivation of the present work 7

2 The Interplay of Various Catalyst and Reaction Parameters in the Decomposition of N_2O over Supported Ru 18

2.1 Introduction 10

2.2 Ru catalysts supported on oxide, mixed oxide and spinel 11

2.2.1 Synthesis and characterization of oxide supported Ru catalysts 11

2.2.2 Catalytic activity of Ru supported on metal oxides 14

2.2.3 Impact of excess oxygen 18

2.3 AlF_3 based Ru catalysts 20

2.3.1 Synthesis and characterization of Ru/AlF_3 20

2.3.2 Catalytic activity of Ru/AlF_3 21

2.4 Influence of calcination temperature 22

2.4.1 Characterization of Ru catalysts calcined at different higher temperatures 23

2.4.2 Catalytic tests 24

2.5 Conclusion 27

3 Reactivity of N_2O with Transistion Metals Supported on Reducible Oxides 18

3.1 Introduction 30

3.2 Synthesis and characterization of the catalysts 31

3.3 Catalytic tests: transformation of N_2O at room temperature over Ru/CeO_2 .. 33

3.4 Influence of temperature and ruthenium on the amount of N_2O transformed 35

3.5 Temperature programmed reduction of CeO_2 and Ru/CeO_2 by hydrogen ... 37

3.6 Transformation of N_2O at room temperature over other transition metals supported on ceria 38

3.7 Temperature programmed reduction of ceria supported transition metals by hydrogen 40

3.8 Quantification of TPR profiles and N_2O conversion 42

3.9 Conclusion 44
4 Selective catalytic reduction of N_2O with H_2 18
4.1 Introduction 47
4.2 Selective catalytic reduction of N_2O with H_2 48
4.2.1 SCR of N_2O with H_2 at elevated temperature by Ru/CeO_2 48
4.2.2 SCR of N_2O with H_2 by supported Ru, Rh and Fe catalysts 49
4.3 Conclusion 53
5 Influence of Light on the Decomposition of Nitrous Oxide by Supported Metal Catalysts 55
5.1 Introduction 56
5.1.1 Heterogeneous Photocatalysis 56
5.1.2 Fermi Level and Schottky Barrier 60
5.1.3 Zeolites & Silica-Alumina 63
5.1.4 Fluidization 64
5.2 Motivation and Aim 66
5.3 Experimental Procedures 67
5.3.1 Experimental Setup 67
5.3.2 Design of the Photoreactor for the Decomposition of N_2O 68
5.3.3 Design of the Heating Furnace 68
5.3.4 Light Irradiation for Photocatalysis 69
5.3.5 Particle Size Range Determination for Fluidization 69
5.5 Influence of light on the decomposition of N_2O by supported ruthenium catalysts 71
5.5.1 De-N_2O Analysis of 1wt% Ru/Al_2O_3 71
5.5.2 De-N_2O Analysis of 1wt% Ru/TiO_2 76
5.5.3 De-N_2O Analysis of 1wt% $Ru/SiO_2 – Al_2O_3$ (1:3) 79
5.5.4 De-N_2O Analysis of 1wt% Ru/ZSM-5 81
5.5.5 Comparison between the supported Ru catalysts 85
5.6 Supported Silver Catalysts 86
5.7 Comparison of the influence of light between supported Ru & Ag catalysts 89
5.8 Conclusion 89
6 Summary 91
7 Experimental 95
7.1 Materials 96

7.1.1 Synthesis of SiO_2-Al_2O_3 mixed oxides 96
7.1.2 Synthesis of pure Al_2F_3 96
7.1.3 Catalyst preparation by incipient wetness impregnation 97
7.2 Analytical methods 98
7.2.1 N_2 physisorption 98
7.2.2 X-ray diffraction 98
7.2.3 H_2-chemisorption 99
7.2.4 Temperature programmed reactivity 99
7.3 Catalytic measurements 100
7.3.1 Instrumental setup for catalytic activity tests 100
7.3.2 Construction of an UV/vis irradiated tube furnace 100
7.3.3 General Test Procedures for the Decomposition Process 101
7.3.4 Photo-assisted N_2O decomposition measurements 102
7.3.5 Selective catalytic reduction 103
8 Appendix 104
9 References 106

Chapter 1

Introduction

1.1 Origins and effects of nitrous oxide

Nitrous oxide, dinitrogen monoxide (IUPAC) or laughing gas is a colorless gas with a sweetish scent with a boiling point of −88.48 °C and a melting point of -90.86 °C. The chemical formula of nitrous oxide is N_2O and the structural formula is depicted in Figure.1. The compound has a molar mass of 44.01 g/mol and possesses a dipole moment.[1]

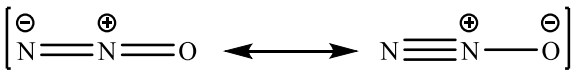

Figure 1.1: Structural formula of nitrous oxide.

Nitrous oxide is a greenhouse gas with a 310 times higher greenhouse warming potential than carbon dioxide.[2] Compared to preindustrial levels (year 1750) the nitrous oxide mole fraction rose by 22 % from 270 ppb to 329 ppb in 2016 (see Figure 1.2). Therefore, the understanding of its origin and control should notably contribute to the stabilization of Earth's climate.

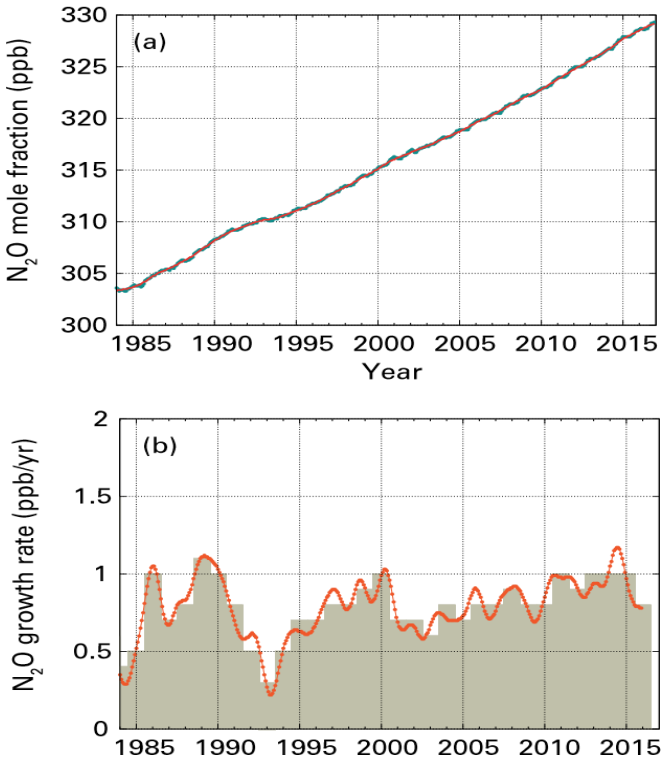

Figure 1.2. Globally averaged N_2O mole fraction (a) and its growth rate (b) from 1984 to 2016[3].

N_2O is emitted by both natural and anthropogenic sources. Natural emissions include terrestrial, marine, and atmospheric sources and are estimated at about 11 Mt

N_2O−N/yr (megatons of N_2O in equivalent nitrogen units per year), compared to about 6 Mt N_2O−N/yr of anthropogenic emissions.[4] Human activities that contribute to N_2O emissions include mainly the biological transformation of fertilizer's nitrogen into N_2O (agriculture), biomass burning, combustion of fossil fuels, industrial activities, wastewater treatment, aquaculture and the use of solvents.[5-7] N_2O emissions from the oceans due to anthropogenic N deposition should be also included.[8]

Agriculture is by far the largest source of N_2O emissions due to human activities, responsible for 4.1 Mt N_2O−N/yr, which is equivalent to 66% of total gross anthropogenic emissions. N_2O emissions from synthetic fertilizers, manure, and crop residues are mainly involved in agricultural N_2O emissions. N_2O emissions from biomass are mostly derived from forest fires, crop residue burning and biomass combustion for heating and cooking. Nowadays N_2O derived from biomass emissions are equivalent to 0.7 Mt N_2O−N/yr, corresponding to 11% of total gross anthropogenic emissions.[4, 9]

N_2O emissions from mobile sources are released primarily by three-way catalytic converters (TWCs), which are worldwide employed to simultaneously abate nitrogen oxides (NOx), carbon monoxide (CO), and hydrocarbons (HCs).[4] The amount of N_2O released by the transportation sector is mainly affected by the adopted control technology, the driving cycle, the TWC operating temperature as well as by the TWC composition and aging.[10, 11] N_2O is a byproduct of the reactions taking place in TWCs and its formation is notably favored during the "cold start" and "intermediate temperature" periods. Additionally, N_2O emissions are in general increased as a result of catalyst deactivation.[12-14]

1.2 N_2O Abatement Technologies

Nowadays, N_2O emissions are significantly increased as compared to the pre-industrial period. It is estimated that anthropogenic N_2O emissions in Europe must be reduced from the present value of 1200–1300 kt N_2O-N/ year to approximately 200–250 kt N_2O-N/ year, in order to limit further global warming to 0.1ºC/decade.[15, 16] Therefore, the control of N_2O emissions from combustion and chemical processes is of significant importance. Among the different remediation methods proposed so far, the end-of-pipe catalytic technologies represent the most promising alternatives, due

to their lower energy requirements and consequently lower cost. Among them, the catalytic decomposition and the selective catalytic reduction (SCR) of N_2O to N_2, represent the most promising approaches. Moreover, the employment of N_2O as a reactant could be an alternative route for N_2O abatement, in addition to the end-of-pipe catalytic technologies.[17-20] The integration of N_2O emission sources (e.g., adipic acid plants) with chemical processes utilizing N_2O as mild oxidizing agent (e.g., oxidative dehydrogenation) could be an interesting approach for N_2O emissions control.[21-24]

N_2O abatement technologies had been developed and applied into industrial applications to assist with the reduction of the high N_2O emissions.[25, 26] Despite the advancement in various abatement technologies, decomposition of N_2O into its elemental constituents remained one of the most suitable methods for N_2O reduction as harmless product gases are released into the atmosphere.[27, 28] The thermal decomposition of gaseous N_2O can only take place at temperatures above 600 °C:

$$2N_2O \rightarrow 2N_2 + O_2 \qquad \Delta H° \text{ (25 °C)} = -163 \text{ kJ mol}^{-1} \qquad (1.1)$$

The activation energy for thermal fission of the N–O bond is about 250–270 kJ mol^{-1}, and it releases enormous heat leading to a maximum adiabatic temperature as high as 1625°C.[29, 30] In the adipic acid industry, thermal destruction is an N_2O abatement process which utilised reducing flame boilers system to reduce the N_2O into its elemental forms, N_2 and O_2, upon release into the atmosphere[25, 27, 31]. The process is often operated at temperatures as high as 1500°C to decompose N_2O into its constituents fully. Reducing agents such as methane are also introduced to facilitate the reduction process better.[32] It was shown that the reducing flame burner system destroyed 98-99% of the N_2O emission. However, the high operating conditions of the flame burner system resulted in higher energy consumption.[33-35]

Catalytic decomposition process was introduced to counter the high energy-consuming process. The presence of a catalyst can lower the decomposition temperature and accelerate the reaction remarkably. Unlike the thermal process, the catalytic decomposition can be operated at lower temperatures. Results showed that the catalytic process conducted at 500°C with an off-gas stream consisting of 23% N_2O obtained a 99% N_2O decomposition rate. Works of literature also noted that supported ruthenium,[36-39] cobalt,[40-43] copper[44, 45] and rhodium[46-49] catalysts were active in the decomposition process. The catalytic activity of these catalysts can be

dependent on various factors. Development in catalysis studies also led to the discovery of potential commercial catalysts such as Pd/Al_2O_3. However, it was noted that factors such as the catalyst lifetime could eventually become a potential problem with the decomposition rate[32, 50].

Supported and unsupported metals, pure and mixed oxides, and zeolitic systems are known to be active in the catalytic decomposition of nitrous oxide[17, 26, 51]. The advantage of noble metal catalysts are high conversions at lower temperature but compared to noble metal free catalysts they are more prone to deactivation in the presence of components contained in flue gas.[52] Noble metal free catalysts are also less expensive. The catalytic activity in case of supported noble metal catalysts depends on the metal, precursor, metal loading, support, preparation method, additives, composition of the gas stream and the dispersion of the noble metal on the support. Different catalytic systems show a different dependence on these factors.[53-56]

Cobalt, copper, ruthenium, iridium and rhodium show high activity for nitrous oxide decomposition but also palladium, platinum, iron and nickel are noteworthy.[57-61] Rhodium catalysts are among the most active known systems, decomposing nitrous oxide completely in a range from 300°C to 400°C. Supports like alumina, ceria, titania, magnesia, zirconia and silica are commonly used, but also hydroxyapatite and carbon can be employed[62-67]. A major problem when using such a catalyst is deactivation due to gases that are usually present in exhaust fumes. Oxygen, water, nitric oxide, sulfur dioxide and carbon dioxide are known to both reversibly and irreversibly diminish catalytic activity[39, 49, 62].

The catalytic decomposition of nitrous oxide can be described by equations (1.2) to (1.5). The desorption of oxygen is assumed to be the rate limiting step[39, 62, 65]. The catalyst donates electron density to the antibonding orbital of nitrous oxide, therefore weakening the bonds of said compound. According to equation (1.4) two adsorbed oxygen atoms combine and leave the catalyst surface (*Langmuir-Hinshelwood* mechanism). Equation (1.5) proposes an *Eley-Rideal* mechanism. A nitrous oxide molecule from the gas phase interacts with an adsorbed oxygen and molecular nitrogen and oxygen desorb from the surface providing an empty catalytic site.

$$N_2O + * \rightarrow N_2O^* \quad (1.2)$$

$$N_2O^* \rightarrow N_2 + O^* \quad (1.3)$$

$$2\ O^* \rightleftarrows O_2 + 2 * \quad (1.4)$$

$$N_2O + O^* \rightleftarrows N_2 + O_2 + * \quad (1.5)$$

Despite ongoing research efforts, the role of support and some variables on catalytic reactivity in the N_2O decomposition has not been well established. Earlier reports have demonstrated an obvious influence of chosen support materials for rhodium as well as ruthenium on the catalytic activity (for rather similar metal dispersion).[63, 65] There is thus a need for further studies on the development of catalysts for N_2O decomposition, especially to select new classes of catalyst supports and to understand the key factors responsible for their activity.

1.3 Catalysts for N_2O decomposition

1.3.1 Ruthenium Catalysts

Ruthenium catalysts are commonly involved in the catalytic decomposition of N_2O. Several literatures had reported and discussed on its efficiency in the N_2O decomposition process. Zheng et al.[65] studied the influence of the catalyst support on the catalytic decomposition of N_2O using supported Ru catalysts. The variation in the catalytic activities of the different catalysts was due to the difference in the active site properties induced by the support material. He also noted the inhibitory effect on the catalytic activity induced by O_2 is dependent on the reducibility of the support material. Zeng et al.[31] reported on the decomposition of N_2O using Ru/Al_2O_3 and discovered that the N_2O conversion increases with the Ru loading at a given reaction temperature.

Chang et al.[68] studied the decomposition of N_2O using Ru loaded on zeolites. It is reported that the acidic Ru/HNaUSY has the highest catalytic activity and it can decompose N_2O at temperatures lower than 120°C. The high catalytic activity suggested that the interaction between the protons in the active sites and the Ru ions may have brought upon a higher conversion rate. The assumption was supported by the absence of N_2O conversion using the pure zeolite supports. Chang et.al[69] also studied the influence of the Ru loading on the zeolite-based catalyst (Ru/NaZSM-5)

and discovered that the catalytic activity decreases with the increasing Ru loading. The findings obtained from Chang et.al contradicts with the findings reported by Zeng et.al. The technique used for the introduction of the Ru ions and the contact between the Ru ions and the sodium (Na) ions in the support material was suggested to be the cause for the decline in catalytic activity.

1.3.2 Cerium oxide based catalysts

Transition metal oxides are of major importance in the field of heterogeneous catalysis, due to their peculiar chemisorptions properties, attributed to the presence of partially filled d-shells of metal ions.[70]

Over the last years, also lanthanides, in particular ceria-based oxides have received increasing attention in the field of heterogeneous catalysis, due to their exceptional physicochemical properties. The high oxygen storage−release capacity of ceria via Ce^{4+}/Ce^{3+} redox cycles is one of the special characteristics of CeO_2, which makes this material remarkably effective in several catalytic processes.[71-73]

Different groups found independently that the abatement of nitrous oxide is also possible at room temperature with supported ceria catalysts.[74, 75] Mainly, they use rhodium supported on ceria for the abatement of nitrous oxide. They found a full nitrous oxide conversion at room temperature, but the catalysts deactivate quite fast. A reductive pretreatment is necessary to obtain the reactivity. Imamura et al.[75] reported the activity of rhodium and rhodium / praseodymium supported on ceria during the nitrous oxide abatement. Approaches considering the quantification of hydrogen consumption and nitrous oxide conversion were done. Centi et al.[74] found that the decomposition activity depends on the free metallic surface area. Furthermore, they suggest that the reaction takes place on the metal-support interface.

1.4 Aim and motivation of the present work

Despite ongoing research efforts, the role of support and some variables on catalytic reactivity in the N_2O decomposition has not been really established. There is thus a need for further studies on the development of catalysts for N_2O decomposition,

especially to select new classes of catalyst supports and to understand the key factors responsible for their activity. One of objectives of the present study was to contribute to a better understanding of the above topics by addressing some of the variables in the support materials and catalytic tests, which influence the catalytic activities of chosen catalysts. Furthermore, the influential factors were suggested by combining various characterizations, including BET surface area, X-ray diffraction (XRD) and temperature-programmed reduction and desorption (TPR/TPD).

Supported Rh catalysts are among the most active systems for the N_2O abatement, but suffer from high price. In addition to Rh catalysts, the current work broadens the scope of catalysts to pre-reduced transition metals supported on CeO_2, including Ru/CeO_2, Rh/CeO_2, Pd/CeO_2, Ni/CeO_2, and Fe/CeO_2. Different transition metals between group 8 to 10 supported on cerium dioxide were tested at room temperature with N_2O after pre-reduction treatment. The noble metals Ru, Rh and Pd catalysts were chosen to catalyze the reaction with N_2O as classical hydrogen activation metals. The non-noble metals iron and nickel were chosen as cheaper alternatives. With the use of different metals supported on ceria, the interaction between metal and support can be investigated in detail. Furthermore, concepts like the Pilling-Bedworth ratio of the metals could be applied to clarify the different reactivity behavior of late transition metals supported on CeO_2.

Selective catalytic reduction (SCR) is the technique to reduce the amount of nitrous oxide mainly with ammonia as reducing agent. A new approach to use H_2 in SCR is presented. The objective is to evaluate the potential of the utilization of H_2 in the SCR of N_2O by supported Ru, Rh and Fe catalysts.

The present study also investigated the influence of light irradiation on the catalytic decomposition of N_2O using supported Ru and Ag catalysts. The experimental procedure and reaction parameters applied resemble the conventional approach for the (thermal catalytic) decomposition of N_2O. The experiments will be conducted under increased temperatures relative to the conventional photocatalytic processes, which are generally performed under ambient conditions.

Chapter 2

The Interplay of Various Catalyst and Reaction Parameters in the Decomposition of N_2O over Supported Ru

2.1 Introduction

Nitrous oxide (N_2O) is the third most significant anthropogenic greenhouse gas and the largest stratospheric-ozone-depleting substance.[76, 77] Without requiring reducing agents and forming only harmless products (N_2 and O_2), the direct catalytic decomposition of N_2O is the preferable method for its removal.[78-80] However, the interplay of various catalyst and reaction parameters and the reaction mechanism still stay unclear.

In recent years, supported ruthenium catalysts have shown efficient catalytic activity for N_2O decomposition.[65, 81] Metal oxides (Al_2O_3, SiO_2) as support have been extensively investigated due to the lower cost and thermal stability.[82-84] In general, silica–alumina mixed oxide is more acidic than alumina. It contains both strong Lewis and Brønsted acidic sites which play important roles in catalytic reaction. The catalytic activities in N_2O decomposition could be further improved by the use of SiO_2–Al_2O_3 mixed oxide supports.[85-88] In addition, aluminum fluoride is an interesting and promising material due to its high intrinsic Lewis acidity and the lack of oxygen in the lattice structure. The properties of AlF_3 are expected to be different from those of metal oxides. It opens the way to more specific applications such as a reference material to the oxygen-containing metal oxides of silica, alumina or spinels and to deeper understanding of the role of lattice oxygen.[89, 90]

Despite ongoing research efforts, the role of support and some variables on catalytic reactivity in the N_2O decomposition has not been really established. Earlier reports have demonstrated an obvious influence of chosen support materials for rhodium as well as ruthenium on the catalytic activity (for rather similar metal dispersion).[63, 65, 91] There is thus a need for further studies on the development of catalysts for N_2O decomposition, especially to select new classes of catalyst supports and to understand the key factors responsible for their activity. The objective of the present study was to contribute to a better understanding of the above topics by addressing some of the variables in the support materials and catalytic tests which influence the catalytic activities of chosen catalysts. Furthermore, the influential factors were suggested by combining various characterizations, including BET surface area, X-ray diffraction (XRD), temperature-programmed reduction and desorption (TPR/TPD) and in situ infrared spectroscopy (IR).

2.2 Ru catalysts supported on oxide, mixed oxide and spinel

2.2.1 Synthesis and characterization of oxide supported Ru catalysts

Oxide supported Ru catalysts were prepared by incipient wetness impregnation with the loading of 1%. The SiO_2-Al_2O_3 mix oxide supports containing 25, 50 and 75 wt% of alumina (named as SiAl25, SiAl50 and SiAl75) were prepared by a co-hydrolyzing method according to that of Leonard et al. (see experimental).[92, 93]

In order to obtain information on structure and oxidation states of the supported Ru species, the oxide-supported catalysts were studied by XRD (Figure 2.1). In addition, chosen data of supported Ru on spinel ($Ru/ZnAl_2O_4$ and $Ru/MgAl_2O_4$) was added for comparison (Figure 2.2). More details on spinels can be found in later subchapter 2.2 and 2.4. In XRD patterns, the weak reflections at 2θ = 28.1°, 35.1° and 54.4° are assigned to the (110), (101) and (211) planes of crystalline RuO_2. A broad peak around 20–30° represents a typical character of amorphous solid of SiO_2-Al_2O_3.[94] Since no peaks corresponding to metallic $Ru^{(0)}$ phases are present, it is concluded that the majority of the Ru species exists in form of RuO_2 particles on the oxide supports after calcination in air at 450°C for 6h. The average sizes of the crystallites are calculated from Scherrer formula. Ru supported on SiO_2-Al_2O_3 mixed oxides almost have the same particle size around 22 nm. For Ru/Al_2O_3 and $Ru/ZnAl_2O_4$, the particle sizes are clearly smaller at 5.3, 9.3nm.

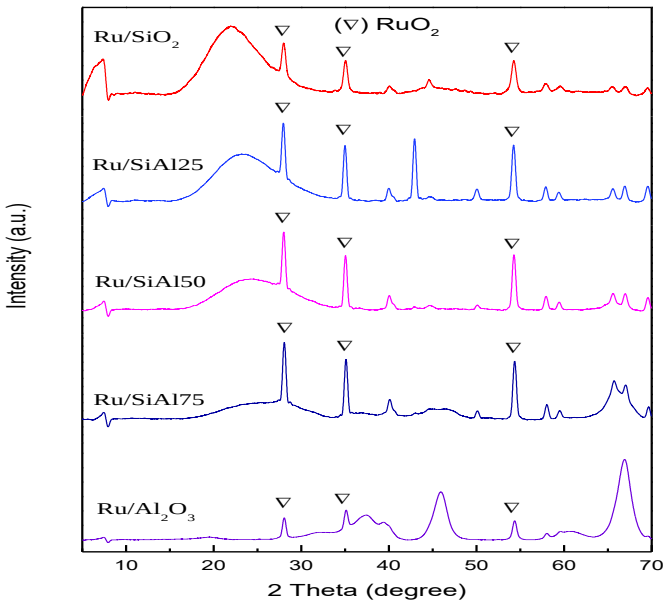

Figure 2.1: XRD patterns of Ru supported on Al_2O_3, SiAl75, SiAl50, SiAl25 and SiO_2

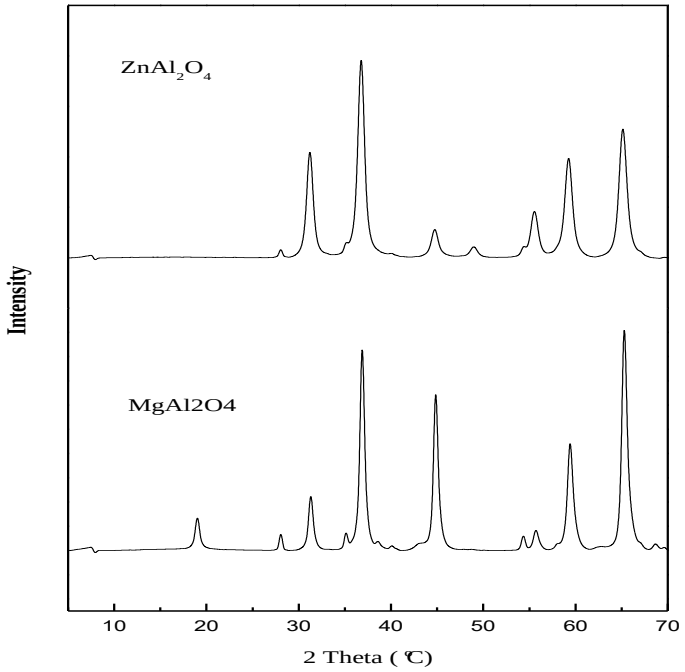

Figure 2.2: XRD patterns of Ru supported on $MgAl_2O_4$ and $ZnAl_2O_4$

The determination of the BET surface area of a catalyst particle is a crucial factor for N_2O decomposition catalytic activity. Different surface areas were obtained for the various catalysts despite having the same Ru loading. The different surface areas obtained could be due to the variations in the catalytic support structure. The support material SiO_2-Al_2O_3 mixed oxide has porous structure and results in a higher surface area. Ru/SiO_2-Al_2O_3 has the surface areas of 353, 376 and 385 m^2/g with the increasing 25, 50 and 75 wt% of alumina in supports. The 1wt% Ru/Al_2O_3 has a BET surface area of 245 m^2/g. The 1wt% Ru/SiO_2 has the smallest surface area among the supported Ru catalyst with the value of 203 m^2/g.

The H_2 chemisorption was used to analysis the dispersion of the metal (Ru) species which can affect the N_2O decomposition catalytic activity. The obtained chemisorption results showed that the 1wt% Ru/Al_2O_3 has the highest Ru dispersion around the catalyst surface with the value of 13.1%. The dispersion value obtained also corresponds to the particle size, whereby small metal particle size results in a higher dispersion. Ru/SiO_2 has the lowest Ru dispersion with the value of 3.2%. The Ru dispersion of Ru/SiO_2-Al_2O_3 catalysts is in the middle with the values from 8.2 to 10.6%.

Table 2.1: BET surface area and particle sizes of Ru catalysts

Sample	S_{BET} (m^2/g)	S_{Ru} (m^2/g)	D (%)	Particle size (nm)
Ru/SiO_2	203	11.8	3.2	21.0
Ru/SiAl25	353	29.8	8.2	22.2
Ru/SiAl50	376	38.4	10.6	22.7
Ru/SiAl75	385	32.8	9.0	22.7
Ru/Al_2O_3	245	47.7	13.1	5.3

The catalysts were investigated by temperature-programmed reduction with H_2 (H_2-TPR) to study the influence of the support material on the reducibility of RuO_x species. As shown in Figure 2.3, the TPR peaks appearing at temperatures between 150°C and 200°C correspond to the reduction of ruthenium oxide(s) to metallic ruthenium. The peak of Ru/Al_2O_3 appears at 182°C. By comparing the profiles of Ru/Al_2O_3 and supported Ru catalysts on different ratios of silica-alumina supports, it can be observed that the reduction temperature becomes slightly lower when the silica contents in the support material increases. However, the reduction temperature slightly increased again for Ru/SiO_2 at 173°C.

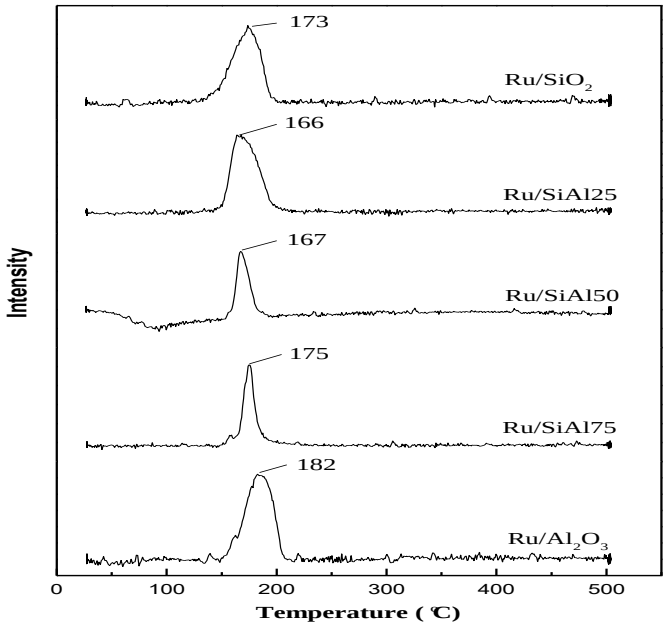

Figure 2.3: H_2-TPR profiles of Ru catalysts supported on Al_2O_3, SiAl75, SiAl50, SiAl25 and SiO_2

In order to get a better understanding of interaction between ruthenium and oxygen species, the O_2-TPD results presented here are extracted from the dissertation of former member Jian Zheng in the same group.[95] All results have been reproduced and extended in the present thesis. Figure 2.4 displays O_2-TPD spectra of the Ru/Al_2O_3 after pretreatment in oxygen at 500 °C for 30 minutes and followed by 1 h of O_2 adsorption at RT. Then the sample was heated in He to 800 °C applying a heating ramp of 5 K/min. Two peaks of oxygen evolution appeared in the TPD process: one weak at 430 °C and another intensive at about 600 °C. It demonstrates that there are two different types of oxygen species on the catalyst surface. Oxygen desorbed from oxidized Ru/Al_2O_3 corresponding to the dominant peak at around 600 °C is attributed to oxygen species of bulk RuO_2. The small peak observed at lower temperature is due to oxygen species interacting weaker with Ru.

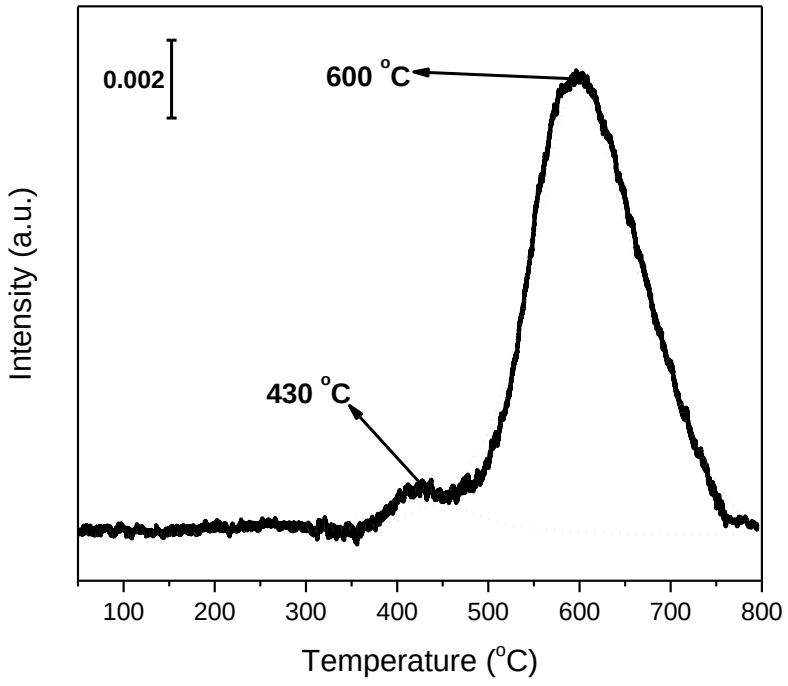

Figure 2.4: O_2-TPD profile of Ru/Al_2O_3. The catalyst was pretreated with O_2 at 500 °C for 30 minutes followed by cooling down to RT in the same atmosphere

2.2.2 Catalytic activity of Ru supported on metal oxides

The decomposition of N_2O over Ru supported on Al_2O_3, SiAl75, SiAl50, SiAl25, SiO_2 and $ZnAl_2O_4$, $MgAl_2O_4$ spinel is studied.

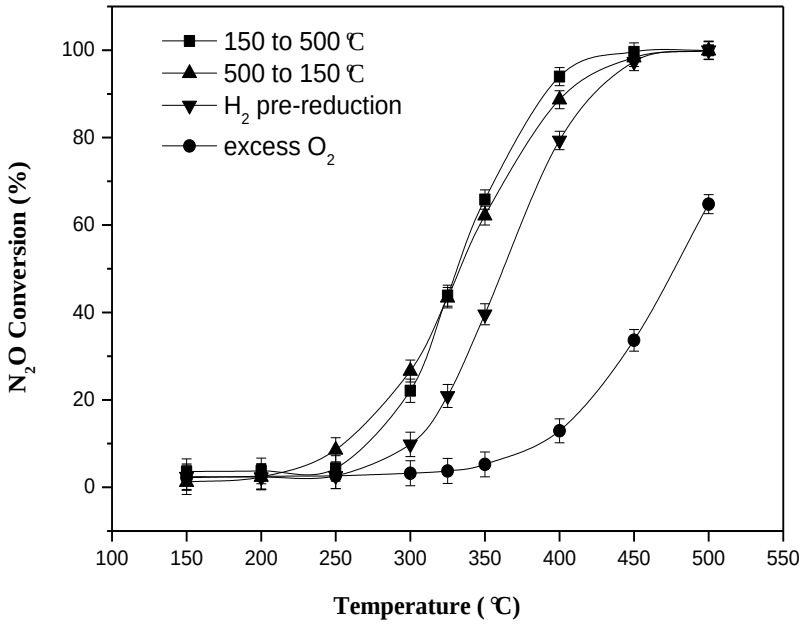

Figure 2.5: N_2O conversion with catalyst Ru/SiAl75 for measurements (■) from 150 to 500 °C (▲) from 500 to 150 °C (▼) after 5% H_2 pretreatment, and (●) in excess of 5% O_2 in the feed.

A typical experimental approach is shown in Figure 2.5 for the catalyst Ru/SiAl75, which includes measurements with temperature ramp up and down with pre-oxidized catalysts, with H_2-pre-reduced ones and measurements under 5% O_2 excess in the feed gas. All catalytic measurements were performed firstly starting from low(er) to higher temperature in 50 K steps, followed by measurements down to lower temperature. These experiments can give information on the stability of the catalysts under typical reaction conditions.

The conversion of “low to high” and “high to low” measurements are almost identical for nearly all supports studied (no “hysteresis”). This indicates that N_2O and temperatures of 500°C (maximum temperature applied) has no influence on the (short-term) stability of catalyst. Under identical conditions, the pre-oxidized catalysts are more active than the pre-reduced ones, again for the majority of the supports indicating that ruthenium oxide(s) rather than metallic ruthenium act as active species. As expected and known, introduction of O_2 has an inhibitory effect on the N_2O decomposition. This indicates that the active sites are poisoned by oxygen increasing the desorption temperature. Inhibitory effect of O_2 on the catalytic activities will be further discussed in the following part.

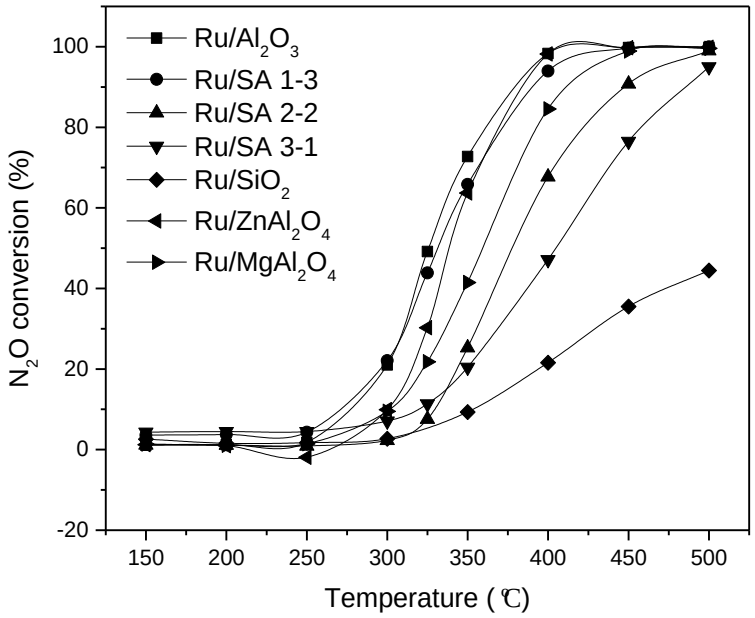

Figure 2.6: N_2O conversion with different catalysts under condition from 150 to 450°C after calcination at 450°C for 6h in air. For comparison, the results of $Ru/ZnAl_2O_4$ and $Ru/MgAl_2O_4$ were also added.

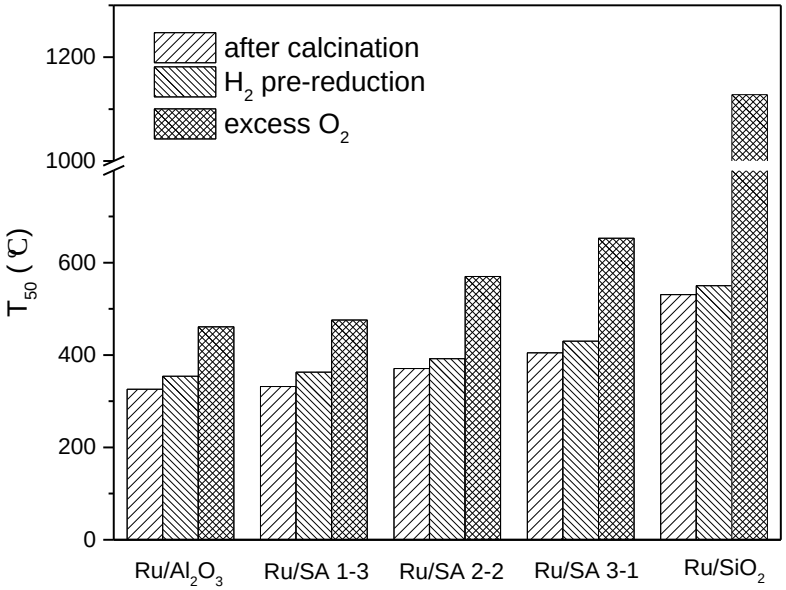

Figure 2.7: T_{50} of N_2O decomposition on Ru catalysts supported on different supports. All the catalysts were measured after calcination directly; with H_2 pre-reduction; with 5% O_2 excess in feed gas.

N_2O conversion with different catalysts under condition from 150 to 450°C after calcination is shown in Figure 2.6. For comparison, the results of $Ru/ZnAl_2O_4$ and

$Ru/MgAl_2O_4$ were also added. T_{50} of N_2O decomposition under different conditions were compared in Figure 2.7. T_{50} of N_2O decomposition increase with the increasing content of SiO_2 in Ru catalysts support. The same trend applies to conditions 5% H_2 pre-reduction of the catalysts at 300°C and 5% O_2 excess in feed gas. This corresponds with earlier research that have demonstrated an obvious influence of chosen support materials for rhodium as well as ruthenium on the catalytic activity (for rather comparable metal dispersion). Introduction of O_2 has an inhibitory effect on the N_2O decomposition, which increase the T_{50} drastically.

As all catalysts were subjected to the same preparation and calcination processes, the differences in catalytic activity must be due to either electronic or structural differences of the active metal centers induced by the respective support, or synergistic involvement of the support in the N_2O decomposition reaction. In our previous research, Ru/TiO_2 was found to show the best performance accompanied by easiest reducibility.[65] The general catalytic performance ranking of Ru catalysts correlates with different ratio of Al_2O_3 to SiO_2 and spinel species. However, it can't be simply explained by the TPR peak temperatures due to missing of systematic differences. The trend in the overall catalytic performance in the decomposition of N_2O seems to be governed by the alteration of the support material, not by the reducibility. This could be further supported by performances of catalysts without and with H_2 pre-reduction. The pre-oxidized catalysts are more active than the pre-reduced ones indicating that ruthenium oxide(s) rather than metallic ruthenium act as active species. Reducibility of silica-alumina composite has minor influence on the catalytic performance. The strong Lewis and Brønsted acidic sites in silica-alumina composition can not promote N_2O catalytic decomposition significantly. However, basic sites could be beneficial for N_2O decomposition as reported before.[47, 96, 97] Higher Ru dispersion was observed in the Al_2O_3 rich Ru/SiO_2-Al_2O_3 catalysts, corresponding to stronger metal-support interaction and higher catalytic activity. The high activity of Ru/Al_2O_3 compared to Ru/SiO_2-Al_2O_3 is possibly due to abundant basic sites and higher Ru dispersion (Table 2.1).

As shown in the catalytic testing section, N_2O was almost completely decomposed on Ru/Al_2O_3 above 350°C. At this temperature, desorption of O_2 by recombination of adsorbed oxygen atoms is not possible, because desorption of oxygen species from Ru starts only at 360°C and (local) maximum at 430°C. Thus, we assume that for

catalytic decomposition of N_2O on Ru/Al_2O_3, the adsorbed oxygen species possibly interact with N_2O molecules from the gaseous phase followed by desorption of N_2 and O_2 rather than by the recombination of co-adsorbed oxygen atoms. The reaction is likely to follow an Eley–Rideal mechanism.

2.2.3 Impact of excess oxygen

In order to study the sensitivity of oxide-based Ru catalysts to the presence of oxygen in the feed, 5% O_2 were added to the gas feed for the decomposition of N_2O.

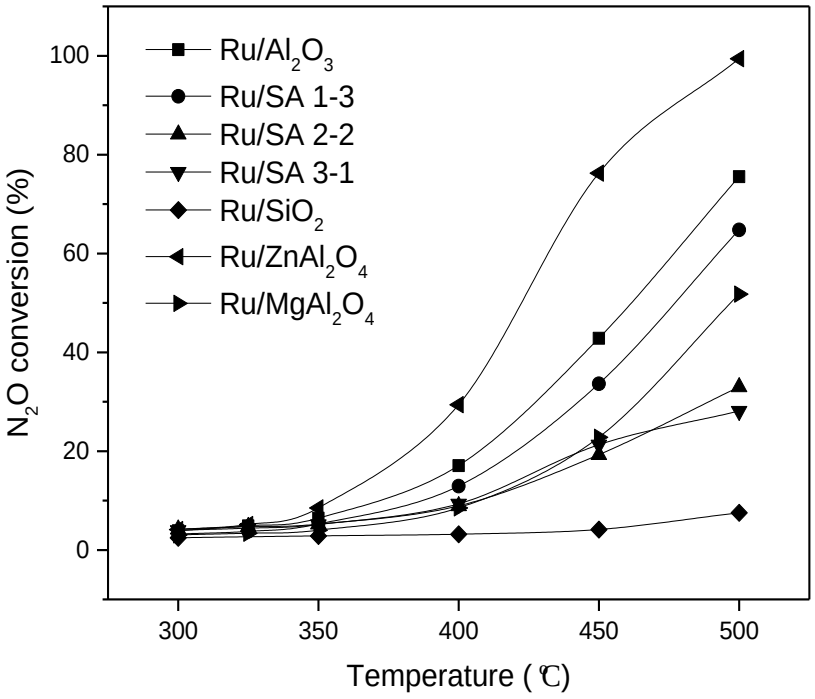

Figure 2.8: N_2O conversion over different catalysts with 5% O_2 in feed gas

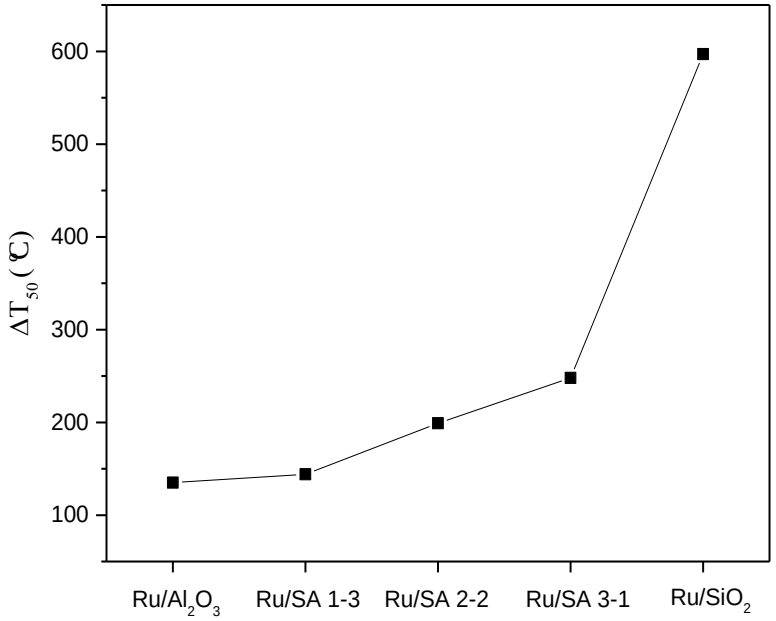

Figure 2.9: T_{50} increase (ΔT_{50}) observed in the presence of oxygen

Although the general order of catalytic activity does not change, a significant shift to higher temperatures is observed for all catalysts. The “relative” sensitivity of the catalysts to the presence of oxygen in the feed gas is found to be dependent on the support material. Based on the T_{50} increase (ΔT_{50}) observed in the presence of oxygen, i.e. the oxygen sensitivity of the catalysts rises in the order: Ru/Al_2O_3 (ΔT_{50} = 135K) < Ru/SA 1-3 (ΔT_{50} = 144K) < Ru/SA 2-2 (ΔT_{50} = 199K) < Ru/SA 3-1 (ΔT_{50} = 248K) < Ru/SiO_2 (ΔT_{50} = 497K). This order is related to the catalysts overall catalytic activity ranking (ΔT_{50}). The catalytic activities of Ru/SiO_2 and Ru/SA 3-1 drop significantly in the presence of oxygen. This effect is less pronounced for Ru/SA 2-2 and Ru/SA 1-3 and minimal for Ru/Al_2O_3. ΔT_{50} of N_2O decomposition increase with the increasing content of SiO_2 in Ru catalysts support, whereas Brønsted acidity seems to have minor influence on it.

$Ru/ZnAl_2O_4$ can achieve nearly 100% N_2O conversion at 500 °C with presence of excess of O_2. This could be due to the formation of a new phase and interaction between Ru and spinel structure. Increased Ru dispersion could also be responsible to the increased activity. From the point of view of molecular dispersion, Ru could possibly incorporated into spinel and form isolated Ru ions.

Introduction of O_2 has an inhibitory effect on the N_2O decomposition. This indicates that the active sites are poisoned by oxygen increasing the desorption temperature. It is clear that a stronger interaction between ruthenium and oxygen (indicated by higher H_2-TPR and O_2-TPD peak temperatures) leads to a reduced number of active sites available for N_2O decomposition. Results indicate that Ru/Al_2O_3 shows lower degree of inhibition by gaseous oxygen in the reaction due to stronger metal-support interaction. The effect of higher Ru dispersion is consistent with this hypothesis.

2.3 AlF_3 based Ru catalysts

Aluminum fluoride (AlF_3) is an interesting and promising material due to its high intrinsic Lewis acidity, and the lack of oxygen in the lattice structure. It opens the way to more specific applications such as a reference material to the oxygen-containing metal oxides of silica, alumina and to spinels. The properties of AlF_3 are expected to be different from those of metal oxides. In previous research, a useful method has been reported for the synthesis of amorphous AlF_3 materials with comparatively high specific surface area of approximately 60 m^2g^{-1}.[89]

2.3.1 Synthesis and characterization of Ru/AlF_3

AlF_3 has been prepared according to the previous reported method.[89] Immobilization of Ru on AlF_3 has been performed by incipient wetness impregnation (see experimental). The loading of Ru is 1%.

Table 2.2: BET surface area of 1% loading Ru/AlF_3

Sample	Surface area (m^2/g)
AlF_3	60
Ru/AlF_3	50.2

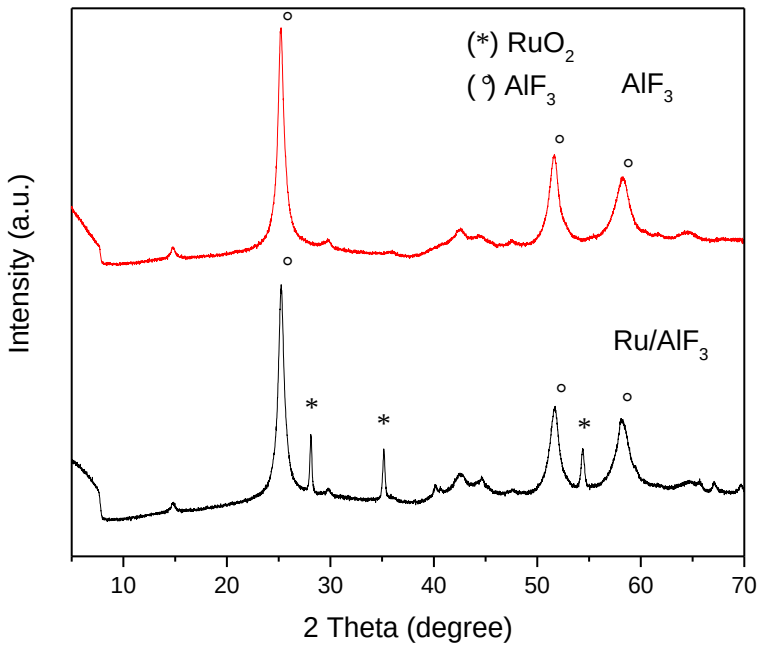

Figure 2.10: XRD pattern of AlF_3 and Ru/AlF_3

X-ray powder diffraction measurements were performed to investigate the bulk structure of the material. The X-ray diffraction measurements indicate that the bulk material consists of trigonal α-AlF_3. No crystalline oxide or hydroxide species were detected after calcination in air. The water of crystallization is removed by thermal treatment, resulting in an amorphous, water-free AlF_3 which starts to crystallize at higher temperatures (450°C). The reflections at 2θ = 28.1°, 35.1° and 54.4° are assigned to the (110), (101) and (211) planes of crystalline RuO_2. The BET surface area results are shown in Table 2.2. The BET surface area didn't change remarkably before and after ruthenium loading with about 60 m^2/g.

2.3.2 Catalytic activity of Ru/AlF_3

N_2O conversion with Ru/AlF_3 catalyst under different conditions are shown in Figure 2.11.

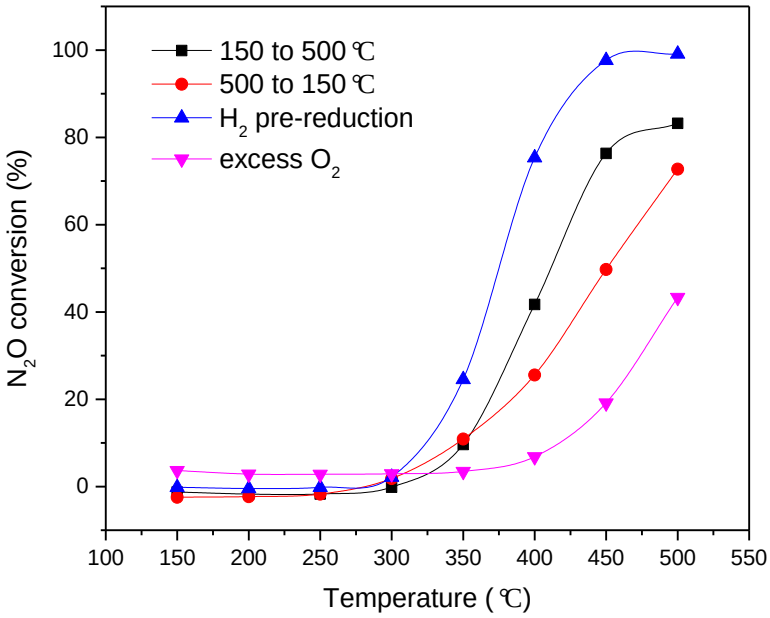

Figure 2.11: N_2O conversion with Ru/AlF_3 catalyst under condition (■) from 150 to 500 °C (●) from 500 to 150 °C (▲) 5% H_2 pre-reduction and (▼) 5% O_2 in feed gas

T_{50} of "low to high" process is 410°C. Slight changes of the catalytic activity of the catalysts were found between "low to high" and "high to low" procedures. The interesting point is that Ru/AlF_3 becomes more active after pre-reduction with decreasing T_{50} down to 375°C. This could be explained by the lack of oxygen in support lattice structure and missing involvement of oxygen from support material in the N_2O decomposition process. As well, introduction of O_2 has an inhibitory effect on the N_2O decomposition.

2.4 Influence of calcination temperature

Spinels are another group of support materials, which should be investigated for ruthenium catalysts. Two ways to these catalysts materials were done: (i) Ru is immobilized by incipient wetness on a $ZnAl_2O_4$ spinel and (ii) a spinel structure is hoped to be formed by high temperature treatment of Ru/Al_2O_3 catalysts described in the former subchapter. Ru/Al_2O_3 and $Ru/ZnAl_2O_4$ catalysts calcined at different higher temperatures were prepared with the loading of 1%.

2.4.1 Characterization of Ru catalysts calcined at different higher temperatures

The BET surface area of Ru/Al_2O_3 and $Ru/ZnAl_2O_4$ calcined at 500, 700, 900°C are shown in Table 2.3.

Table 2.3 BET surface area of Ru/Al_2O_3 and $Ru/ZnAl_2O_4$ calcined at 500, 700, 900°C

Sample	Surface area (m^2/g)	Sample	Surface area (m^2/g)
Ru/Al_2O_3 500°C	222	$Ru/ZnAl_2O_4$ 500°C	94
Ru/Al_2O_3 700°C	175	$Ru/ZnAl_2O_4$ 700°C	67
Ru/Al_2O_3 900°C	118	$Ru/ZnAl_2O_4$ 900°C	30

The surface area of Ru/Al_2O_3 catalyst decrease from 222 to 118 m^2/g when calcination temperature increase from 500 to 900°C. The surface area of $Ru/ZnAl_2O_4$ decrease from 94 to 30 m^2/g when the calcination temperatures increase from 500 to 900°C. The decrease in the BET surface area of the supported Ru catalysts with the increase in calcination temperature could be a result of destroyed pores structure of the support when exposed to a high temperature environment and of crystallization (sintering).

The XRD patterns of $Ru/ZnAl_2O_4$ and Ru/Al_2O_3 calcined at different higher temperatures (500, 700 and 900°C) are shown in Figure 2.12. The weak reflections at 2θ = 28.1°, 35.1° and 54.4° are assigned to the (110), (101) and (211) planes of crystalline RuO_2.

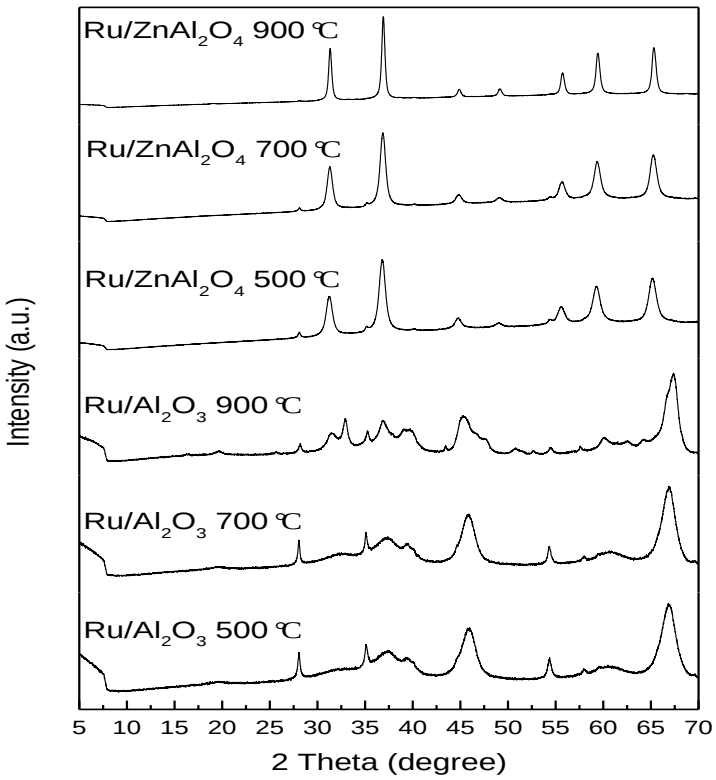

Figure 2.12: XRD patterns of Ru/Al_2O_3 and $Ru/ZnAl_2O_4$ with calcination temperature 500°C, 700°C and 900°C

2.4.2 Catalytic tests

Catalytic performance of $Ru/ZnAl_2O_4$ and Ru/Al_2O_3 calcined at different higher temperatures (500, 700 and 900°C) is shown in Figure 2.13. As can be seen from the Figure, the activity of Ru catalysts is strongly dependent on the calcination temperature. $Ru/ZnAl_2O_4$ (500°C) is the most active catalyst, which decomposes N_2O quantitatively at 450°C. The general order of catalytic activity, based on the temperature required for 50% conversion (T_{50}) is the following: $Ru/ZnAl_2O_4$ (500°C) > Ru/Al_2O_3 (500°C) > Ru/Al_2O_3 (700°C) > $Ru/ZnAl_2O_4$ (700°C) > Ru/Al_2O_3 (900°C) > $Ru/ZnAl_2O_4$ (900°C). The catalytic activity decreases with the increasing calcination temperature. This could be attributed to the decreasing surface area due to higher calcination temperature and Ru dispersion.

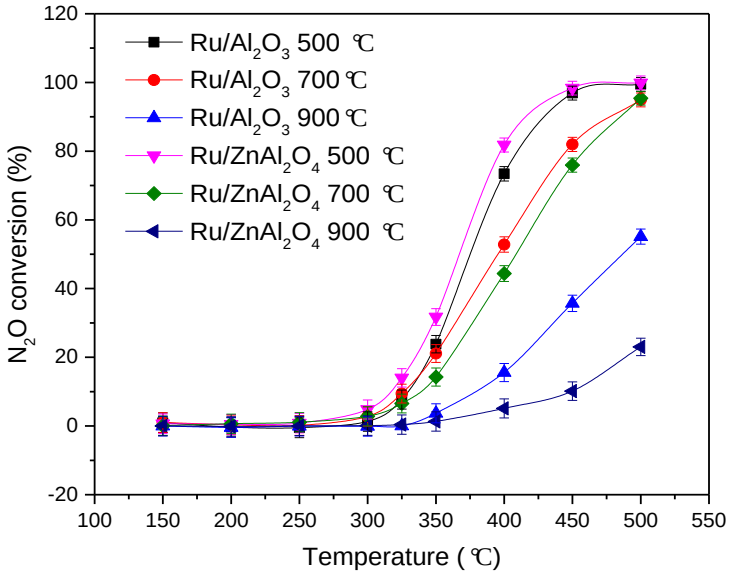

Figure 2.13: N_2O conversion with Ru/Al_2O_3 and $Ru/ZnAl_2O_3$ calcined at different higher temperatures

Catalytic performance of $Ru/ZnAl_2O_4$ and Ru/Al_2O_3 calcined at different higher temperatures (500, 700 and 900°C) with excess 5% O_2 in the feed gas is shown in Figure 2.14. As can be seen, Ru catalysts are less active with excess O_2 in the feed gas. Under the condition of excess O_2, the general order of catalytic activity, based on the temperature required for 50% conversion (T_{50}) is the following: $Ru/ZnAl_2O_4$ (500°C) > Ru/Al_2O_3 (500°C) > $Ru/ZnAl_2O_4$ (700°C) > Ru/Al_2O_3 (700°C) > Ru/Al_2O_3 (900°C) > $Ru/ZnAl_2O_4$ (900°C).

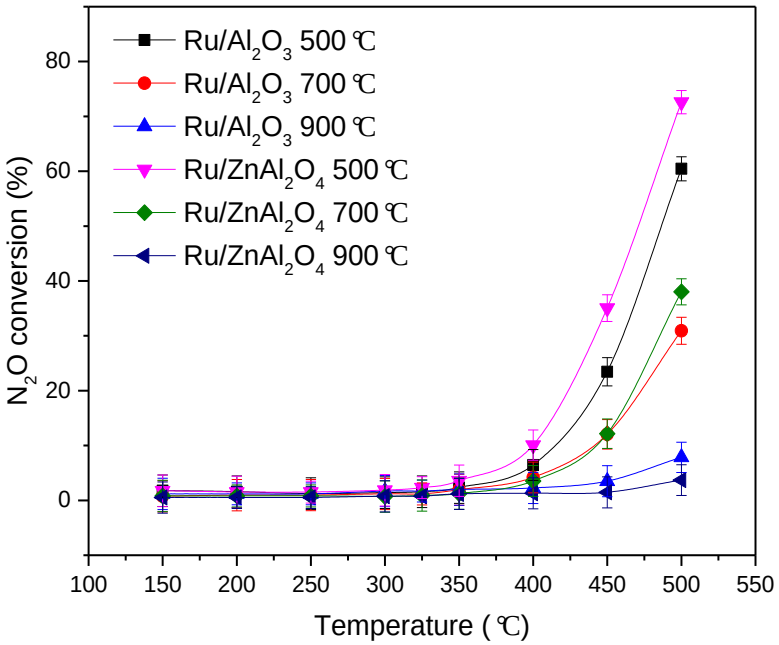

Figure 2.14: N_2O conversion over Ru/Al_2O_3 and $Ru/ZnAl_2O_3$ calcined at different higher temperatures with excess 5% O_2 in feed gas

T_{50} of N_2O decomposition on Ru/Al_2O_3 and $Ru/ZnAl_2O_4$ calcined at different higher temperatures without and with O_2 in the feed gas is shown in Figure 2.15. High calcination temperatures decrease the catalytic activities of Ru/Al_2O_3 and $Ru/ZnAl_2O_4$ with and without O_2 in the feed gas. This could be due to the agglomeration of particles and reduction of BET surface areas during high temperature calcination process.

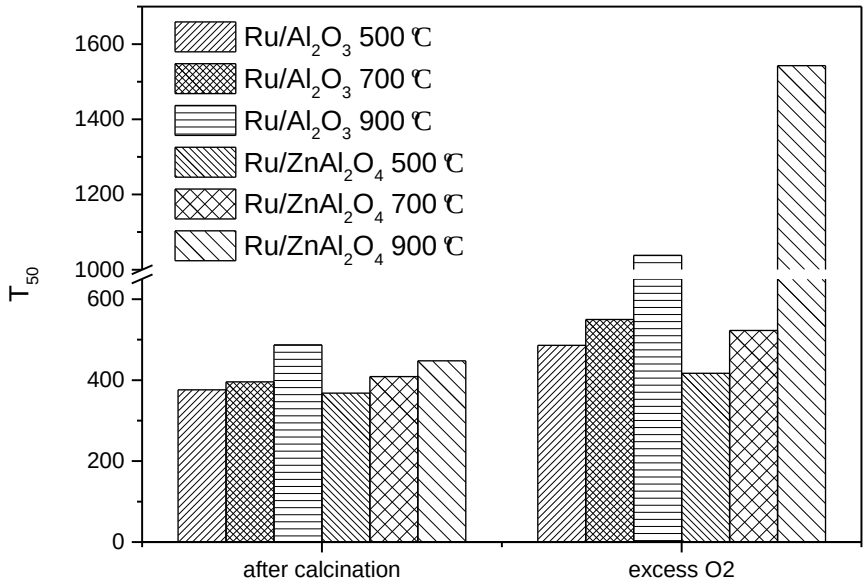

Figure 2.15: T_{50} of N_2O decomposition on Ru/Al_2O_3 and $Ru/ZnAl_2O_4$ with increasing calcination temperatures

2.5 Conclusion

Different chosen support materials for ruthenium catalysts demonstrated an obvious influence on the catalytic activity in N_2O decomposition. This could be explained by varying properties like the metal-support interaction, the dispersion of Ru species and structure and modification of the support. The strong Lewis and Brønsted acidic sites in silica-alumina composition do not influence the catalytic performance significantly. On the other hand, basic sites could be beneficial for N_2O decomposition. Higher Ru dispersion was observed in the Al_2O_3 rich Ru/SiO_2-Al_2O_3 catalysts. This may be due to the stronger metal-support interaction, and leads to higher catalytic activity and lower degree of inhibition by gaseous oxygen in the reaction.

The conversations of “low to high” and “high to low” measurements are almost identical for nearly all supports studied. This indicates that N_2O and temperatures of 500°C (maximum temperature applied) has no influence on the (short-term) stability of the catalysts. Under identical conditions, the pre-oxidized catalysts are more active than the pre-reduced ones, again for the majority of the supports indicating that ruthenium oxide(s) rather than metallic ruthenium act as active species. However,

Ru/AlF_3 becomes more active after pre-reduction with decreasing T_{50} at 375°C. This could be explained by the lack of oxygen in support lattice structure and missing involvement of oxygen from support material in the N_2O decomposition process.

Introduction of O_2 has an inhibitory effect on the N_2O decomposition. This indicates that the active sites are poisoned by oxygen increasing the desorption temperature. $Ru/ZnAl_2O_4$ is found to be the most highly active catalyst for the decomposition of N_2O. It can achieve nearly 100% N_2O conversion at 500 °C even with presence of excess of O_2. This could be due to the formation of new phase and interaction between Ru and spinel structure.

Chapter 3

Reactivity of N_2O with Transition Metals Supported on Reducible Oxides

3.1 Introduction

Nitrous oxide, N_2O, is one of the most harmful greenhouse gases and an important source of stratospheric nitrogen oxides destroying the ozone layer. The emissions from industry, like in the production of nitric acid or adipic acid, are considerable. It is also formed as by-product during the selective catalytic reduction (SCR) of NO_x.[26, 98] The atmospheric concentration of N_2O is increasing by an annual growth rate of 0.5-1.0 ppbv at present.[18] Several catalysts are found to be effective in the decomposition of N_2O at elevated temperatures.[63, 99-101] Of particular interest are catalysts that allow the abatement of N_2O under mild conditions, because in several cases N_2O emissions occur near to room temperature (RT). In addition, N_2O decomposition is of course more attractive than reduction by a then necessary reducing agent.

Such highly interesting catalysts that decompose N_2O at RT have been reported in the literature. Centi et al. investigated the decomposition of N_2O at RT over Rh catalysts supported on several oxides (CeO_2, ZrO_2 and titania-alumina).[74] Imamura et al. reported high activity of pre-reduced supported Rh/Ce and Rh/Pr/Ce catalysts in the decomposition of N_2O at ambient conditions.[75] Supported Rh catalysts are among the most active systems for the N_2O abatement, but suffer from rapid deactivation due to the saturation of the active metal centers by adsorbed oxygen.[102, 103] Other researchers have also investigated mechanistic aspects of N_2O decomposition over carbon films and carbon nanotube supported catalysts. It was experimentally confirmed that carbon materials act not only as supports but also reducing agents to achieve the conversion of NO_x. The formation and desorption of CO_x play a significant role due to the formation of new active centers.[91, 104]

N_2O is a powerful oxidizing agent delivering atomic oxygen in a highly exothermic reaction. N_2O decomposition is comprised of fast oxygen uptake and formation of an oxide layer followed by thickening of the oxide layer due to subsurface and bulk oxidation. The adsorptive decomposition of N_2O as a probe molecule could be employed to determine the specific metal surface area of Cu catalysts, Ni powder, $NiAlO_x$ and Ni/γ-Al_2O_3. Subsurface and bulk oxidation can be sufficiently suppressed at a certain reaction temperature region. In this specific temperature range, the ratio of adsorbed oxygen atoms to the Cu, Ni surface atoms (O/Cu_s and O/Ni_s) remains somewhat constant due to the formation of an oxygen monolayer. It could be applied for specific Cu and Ni surface area determination.[105, 106]

In addition to Rh catalysts, the current chapter broadens the scope of catalysts to pre-reduced late transition metals supported on CeO_2, including Ru/CeO_2, Rh/CeO_2, Pd/CeO_2, Ni/CeO_2, and Fe/CeO_2. Different late transition metals between group 8 to 10 supported on cerium dioxide were reacted at room temperature with N_2O after pre-reduction treatment. The noble metals Ru, Rh and Pd as classic hydrogen activation catalysts were chosen to catalyze the reaction with N_2O. The non-noble metals iron and nickel were chosen as cheaper alternatives. With the use of different metals supported on ceria the interaction between metal and support can be investigated in detail. Furthermore, concepts like the Pilling-Bedworth ratio of the metals could be applied to clarify the different behavior of late transition metals supported on CeO_2.

The interesting catalytic results, N_2O abatement at RT could have been reproduced over all of them very well. The results demonstrate further that the reduction of N_2O over the pre-reduced Ru/CeO_2 happened at room temperature. Detailed mechanistic understanding on the decomposition of N_2O over these catalysts at RT are still missing. Centi et al. suggested that the active sites for the decomposition of N_2O at room temperature are located at the metal–support interface.[74] Also for the noble metal supported on CeO_2, the reduced sites of CeO_2 have been considered to be very important.[75] Other even fundamental questions are open too. Is the transformation of N_2O to N_2 at room temperature in fact a decomposition or a stoichiometric reduction? In all mentioned reports, the catalysts deactivated after certain time. Pre-reduction of the catalyst (noble metal and/or transition metal oxide) by H_2 at elevated temperature prior to the catalytic test was found to be a prerequisite for reactivity at room temperature. The subject of the present investigations was to regard these questions carefully and to get a more detailed picture on the reaction, the active species and the mechanism of this very interesting reaction on these CeO_2-based catalysts at room temperature.

3.2 Synthesis and characterization of the catalysts

In order to investigate room temperature transformation of N_2O, various CeO_2 based catalysts (Ru/CeO_2, Rh/CeO_2, Pd/CeO_2, Ni/CeO_2, and Fe/CeO_2) were prepared with different loading(0.2, 1.0 and 5.0 wt-%) and characterized by XRD, BET, H_2-TPR and *in situ* IR. Synthesis of supported catalysts were via incipient wetness impregnation methods (see experimental).

Powder X-ray diffraction pattern were taken of all samples after calcination (fresh), after TPR (reduced) and after reaction with N_2O (spent). Especially the lower loaded noble metal samples, but also 1.0 wt-% rhodium and palladium supported on cerium oxide show only reflexes of the support, indicating that the active metal is finely dispersed and the loading is very low.

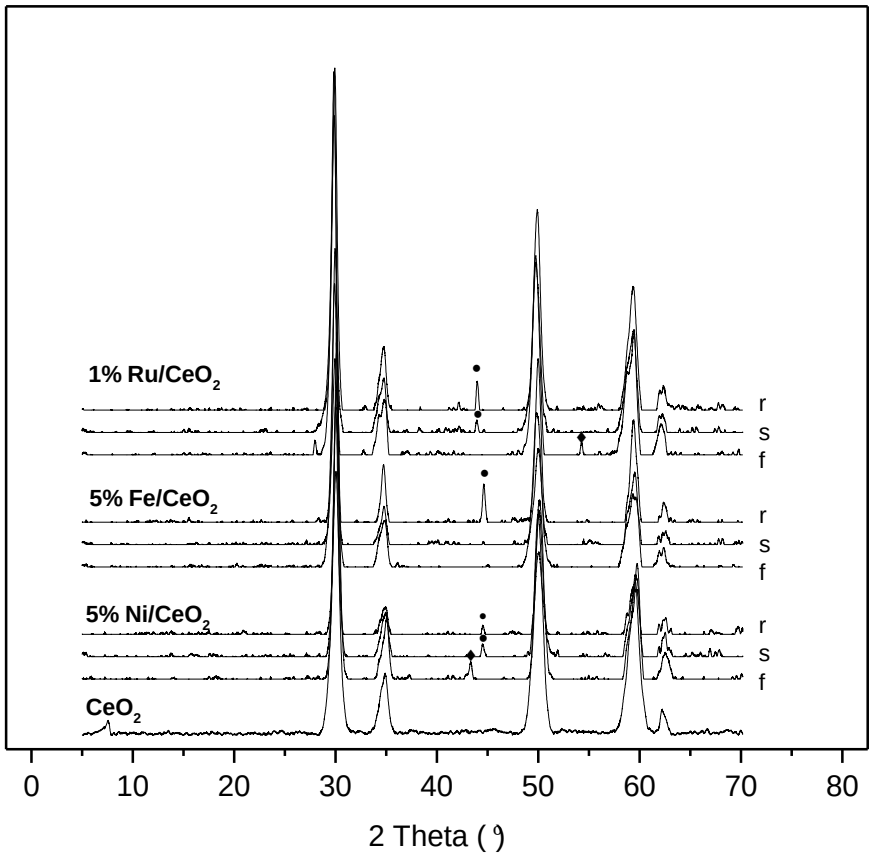

Figure 3.1**:** XRD patterns of fresh (bottom), spent (middle) and reduced (top) nickel, iron and ruthenium supported on ceria. Reflexes belonging to the metal oxide are marked by a diamond (♦), metals by a dot (•)

Reflexes of supported metal or metal oxide can be found in the higher loaded nickel, iron and 1.0 wt-% ruthenium sample (Figure 3.1). The nickel sample after calcination shows a reflex of nickel(II)-oxide. This reflex cannot be found anymore after reduction and after reaction with N_2O. However, a reflex indicating metallic nickel can be found after reduction and reaction. This indicates that nickel(II)-oxide gets reduced during TPR to metallic nickel and stays partially in metallic form on the support after reaction. In contrast, from iron samples reflexes, metallic iron was only identified in the reduced species, but iron was oxidized through to iron oxide after reaction with N_2O. The difference of oxygen coverage will be discussed in the following part via Pilling–

Bedworth ratio. For the ruthenium sample the fresh species show a reflex indicating ruthenium(IV)-oxide. Both spent and reduced catalysts show a reflex indicating metallic ruthenium. The peak indicating metallic ruthenium in reduced species is much larger compared to that of the spent catalyst. This indicates that the ruthenium sample gets at least partially back oxidized during the N_2O reaction and mixed ruthenium oxides remain on the surface. This is in accordance with the quantification results of consumed hydrogen during TPR and converted N_2O in the room temperature reaction.

The BET surface area of the CeO_2 support and supported nickel, iron and ruthenium catalysts are shown in Table 3.1. The supported samples were measured as fresh and spent species. The fresh nickel sample shows a similar BET surface area to the unsupported ceria. The iron and the ruthenium samples have a slightly higher surface area than ceria. The ruthenium and nickel samples show a higher surface area after reaction with N_2O, probably due to the formation of mixed oxide phases on the surface. Only the iron sample shows a reduced surface area after reaction, possibly due to some sintering processes at higher temperatures during the reduction. These results are in accordance to the XRD results.

Table 3.1**:** BET surface of iron, nickel and ruthenium supported on ceria. Measurements after calcination (f, fresh) and reaction with N_2O (s, spent).

Sample	**Surface area (f) (m^2/g)**	**Surface area (s) (m^2/g)**
CeO_2	55.3	**-**
5.0% Ni/CeO_2	52.6	55.2
5.0% Fe/CeO_2	60.3	54.6
1.0% Ru/CeO_2	60.4	73.1

3.3 Catalytic tests: transformation of N_2O at room temperature over Ru/CeO_2

In order to get a better understanding of reactivity of N_2O with CeO_2-based catalysts, some results presented in 3.3, 3.4, 3.5 are extracted from the dissertation of former member Jian Zheng in the same group.[95] All results have been reproduced and extended in the present thesis.

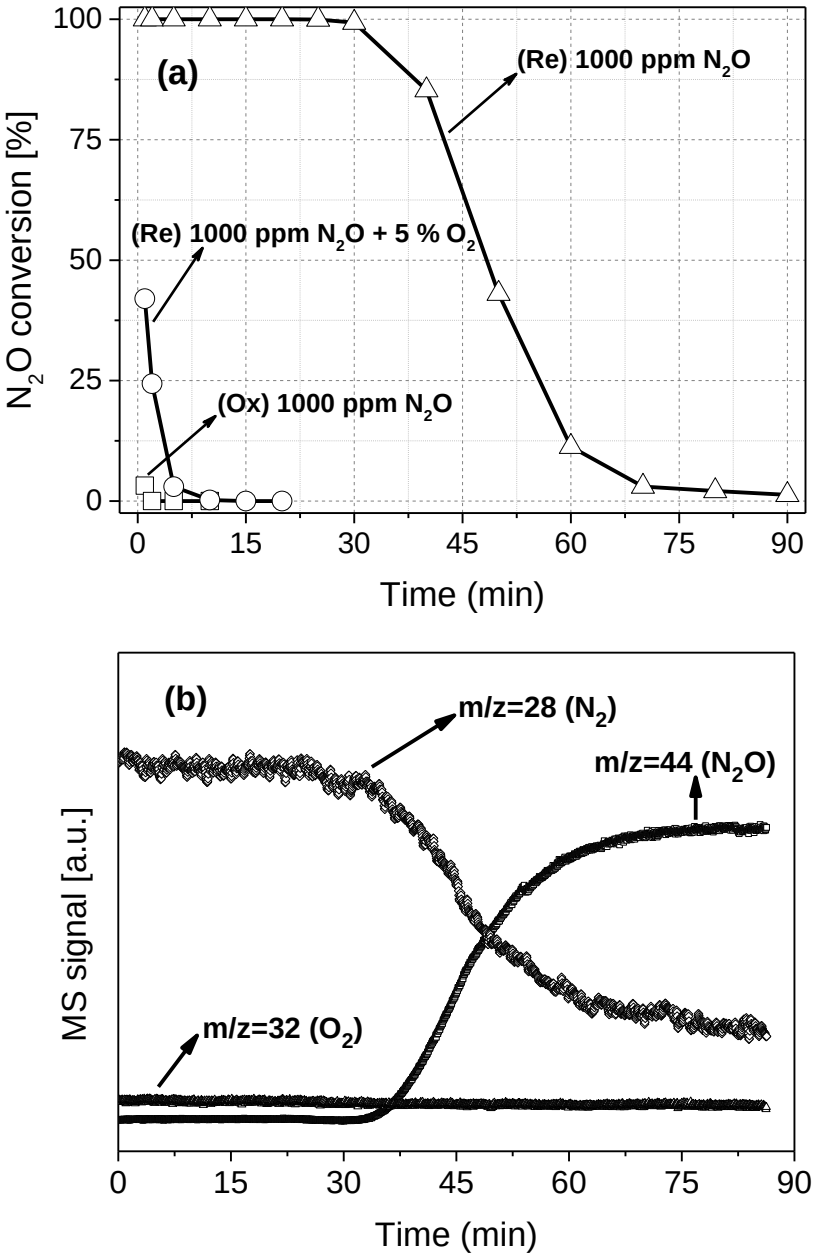

Figure 3.2: (a) N_2O conversion at room temperature (298 K): 1000 ppm N_2O over pre-reduced Ru/CeO_2 (triangle), 1000 ppm N_2O + 5% O_2 over the pre-reduced sample (circles) and 1000 ppm N_2O on pre-oxidized Ru/CeO_2 (squares); (b) Products evolved as determined by mass spectrometry during N_2O conversion; total flow rate = 100 ml/min, GHSV = 24000 h^{-1}.

It was reported that N_2O decomposition at room temperature could be achieved over supported Rh catalysts.[74, 75] In this study, ruthenium instead of rhodium was chosen since it works also quite well as hydrogen activation catalyst. Furthermore, supported ruthenium catalysts showed high catalytic activity in N_2O decomposition.[65] Firstly, N_2O conversion over Ru/CeO_2 has been investigated at room temperature (Figure 3.2a). The conversion as a function of time is strongly dependent on the pretreatment of the catalyst and the presence or absence of oxygen in the feed. N_2O could be

detected in the exhaust gas only after 40 minutes with the pre-reduced catalyst (triangles) indicating 100 % conversion during this time. Both initial conversion and duration of N_2O transformation decreased significantly when 5% O_2 were added to the gas mixture (circles). The catalyst pre-oxidized by O_2 lead to complete deactivation and no N_2O conversion could be observed (squares). Figure 3.2b shows the mass spectroscopic analysis of the product gas mixture as a function of time for the reaction of N_2O (1000 ppm in He) over the pre-reduced Ru/CeO_2 catalyst. In agreement with Figure 3.2a (triangles), the signal of N_2O (m/z = 44) is very weak at the beginning (complete conversion) and starts to increase at 35 minutes. The signal of N_2 (m/z = 28) is formed as the only gaseous product drops at the same time. No oxygen (m/z = 32) could be detected in the product gas mixture during the whole reaction time.

For interpretation, the following (stoichiometric) reactions can be regarded:

$$2\ N_2O \rightarrow O_2 + 2\ N_2 \qquad (3.1)$$

$$2\ N_2O + Ru \rightarrow RuO_2 + 2\ N_2 \qquad (3.2)$$

$$N_2O + Ce_2O_3 \rightarrow 2\ CeO_2 + N_2 \qquad (3.3)$$

Based on the experimental results, however, it is assumed that N_2O was reduced by metallic Ru and/or Cerium(III) oxide species (Equations 3.2 and 3.3) rather than catalytically decomposed (Equation 3.1). N_2O acted as stoichiometric oxidizing agent. The amount of N_2O transformed and the duration of the reaction are in accordance with the reports of Centi et al.[74] and Imamura et al.[75] The total amount of N_2O consumed on 500 mg pre-reduced Ru/CeO_2 was about 320 µmol, what is more than 40 times of the reduction equivalent of the Ru species (Ru(0) $\rightarrow$ Ru(IV)) according to equation 2. Thus, it must be concluded that reduced sites of CeO_2, i.e. cerium(III) oxide species represent the reducing agent for N_2O at room temperature (equation 3.3).

3.4 Influence of temperature and ruthenium on the amount of N_2O transformed

In order to understand the role of Ru and cerium oxides in the transformation of N_2O to N_2 in more detail, the influence of the temperature and of the presence and absence of ruthenium on the amount of N_2O transformed have been studied. The conversions of Ru/CeO_2 and of the Ru-free CeO_2 support at room temperature and 150 °C are presented in Figure 3.3. Both materials show 100% initial conversion at

both temperatures. This confirms the assumption that pre-reduced pure CeO_2 transforms N_2O to N_2 as a highly active accessible reducing site. N_2O conversion as function of reaction time ("deactivation") depends on the reaction temperature. The molar amounts of N_2O converted relative to the molar amount of cerium (and ruthenium) are summarized in Table 3.2. N_2O consumed over pure CeO_2 at room temperature and 150 °C are 60 µmol and 150 µmol, respectively. These amounts remarkably increased to 320 µmol and 480 µmol, when Ru was present. The low amounts of N_2O consumed compared to the total amount of CeO_2 used (around 2900 µmol) might be due to only partial reduction of CeO_2 at the low temperature of the pretreatment procedure (<<600 °C).[107] Obviously, the reducibility of CeO_2 significantly increased by the presence of (metallic) Ru. The more reactive cerium oxide in reduced form was formed by pre-reduction the higher is the total amount of N_2O converted. Improved reducibility of oxide supports by the presence of noble metal particles is well known in heterogeneous catalysis and has also been proposed for the present catalysts by Centi et al. who proposed that the reaction takes place at the Ru-Ce particle-support interfaces the number of which would increase with noble metal loading.[74]

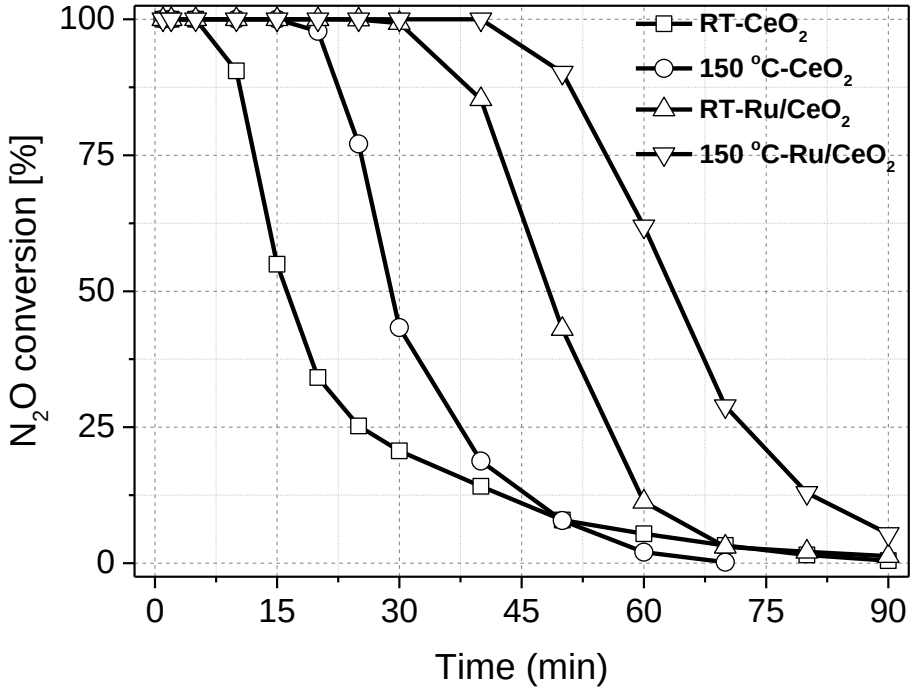

Figure 3.3: Conversion of N_2O over Ru/CeO_2 and over Ru-free CeO_2 at room temperature and at 150 °C. All the samples were reduced with 20% H_2/He at 500 °C for 30 minutes. Total flow rate = 100 mL/min; 1000 ppm N_2O in He; GHSV=24000 h^{-1}.

Table 3.2: The influence of the temperature and of the presence and absence of ruthenium on the amount of N_2O reduced by cerium oxide

Sample	Temperature (◦C)	Amount of Ce (µmol)	Amount of Ru (µmol)	N_2O Reduced (µmol)
Ru/CeO_2	150	2900	7.5	480
Ru/CeO_2	ambient	2900	7.5	320
CeO_2	150	2900	0	150
CeO_2	ambient	2900	0	60

3.5 Temperature programmed reduction of CeO_2 and Ru/CeO_2 by hydrogen

Temperature programmed reduction experiments (H_2-TPR) have been performed to study the reducibility of the Ru/CeO_2 catalyst compared to the pure Ru-free CeO_2 support (Figure 3.4).

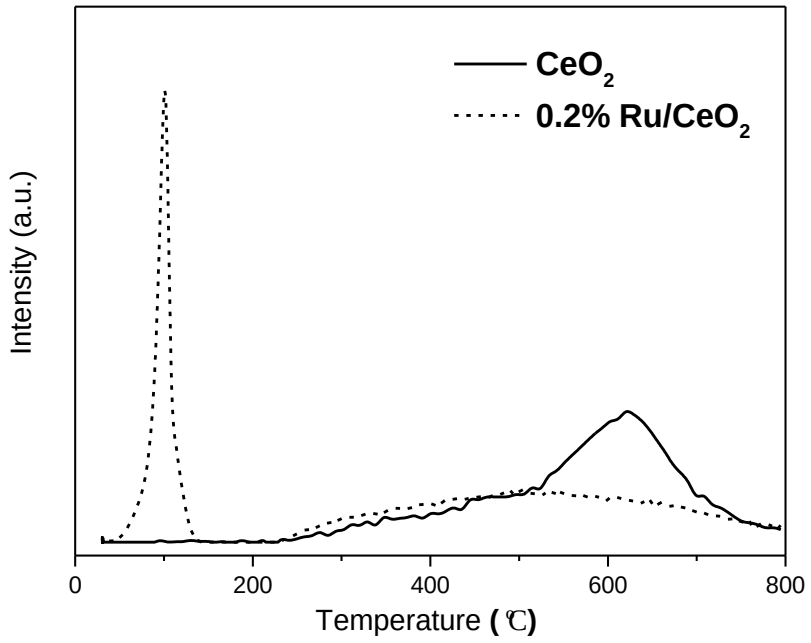

Figure 3.4: H_2-TPR profile of Ru/CeO_2 and CeO_2

The broad reduction bands of the pure support between 300 °C and 700 °C are attributed to the reduction of surface layers of CeO_2. The reduction of bulk CeO_2 will

occur at temperatures above 800 °C only.[108] For the Ru/CeO_2 catalyst, the peak between 50 and 150 °C correspond to the reduction of Ru^{4+} (equation 3.4).[109] The amount of hydrogen consumed is much higher than calculated for the total amount of ruthenium(IV) oxide present (equation 3.4) indicating that reduction of the outermost layer of CeO_2 starts already at this temperature, i.e. immediately when metallic ruthenium is present. The intense peak can be partially assigned to the reduction of surface layers of the CeO_2 support (equation 3.5).[110] The deeper reduction of cerium(IV) oxide in the presence of Ru agrees very well with the reactivity experiments in previous section. Ru plays an important role in hydrogen activation. The enhancement of CeO_2 reducibility by the noble metal is interpreted as spillover of hydrogen from Ru to CeO_2.[111]

$$2\ H_2 + RuO_2 \rightarrow Ru + 2\ H_2O \qquad (3.4)$$

$$H_2 + 2\ CeO_2 \rightarrow Ce_2O_3 + H_2O \qquad (3.5)$$

3.6 Transformation of N_2O at room temperature over other transition metals supported on ceria

Different late transition metals supported on ceria were synthesized by classic incipient wetness impregnation. Noble metals on ceria (ruthenium, rhodium, paladium) were synthesized with 0.2 and 1.0 wt-% loading, respectively, and iron and nickel with 5 wt-% loading. N_2O conversion at room temperature over these samples is shown in Figure 3.5.

Lower loaded (0.2 wt-%) noble metals supported on ceria show only a very short full N_2O conversion between 5 and 15 minutes. Also higher loaded (1.0 wt-%) palladium shows only a very short N_2O conversion of 15 minutes. Higher loaded (1.0 wt-%) ruthenium and rhodium have a much longer N_2O conversion (50 and 75 minutes, respectively). Nickel on ceria shows around 15-20 minutes full conversion, iron over 2 hours.

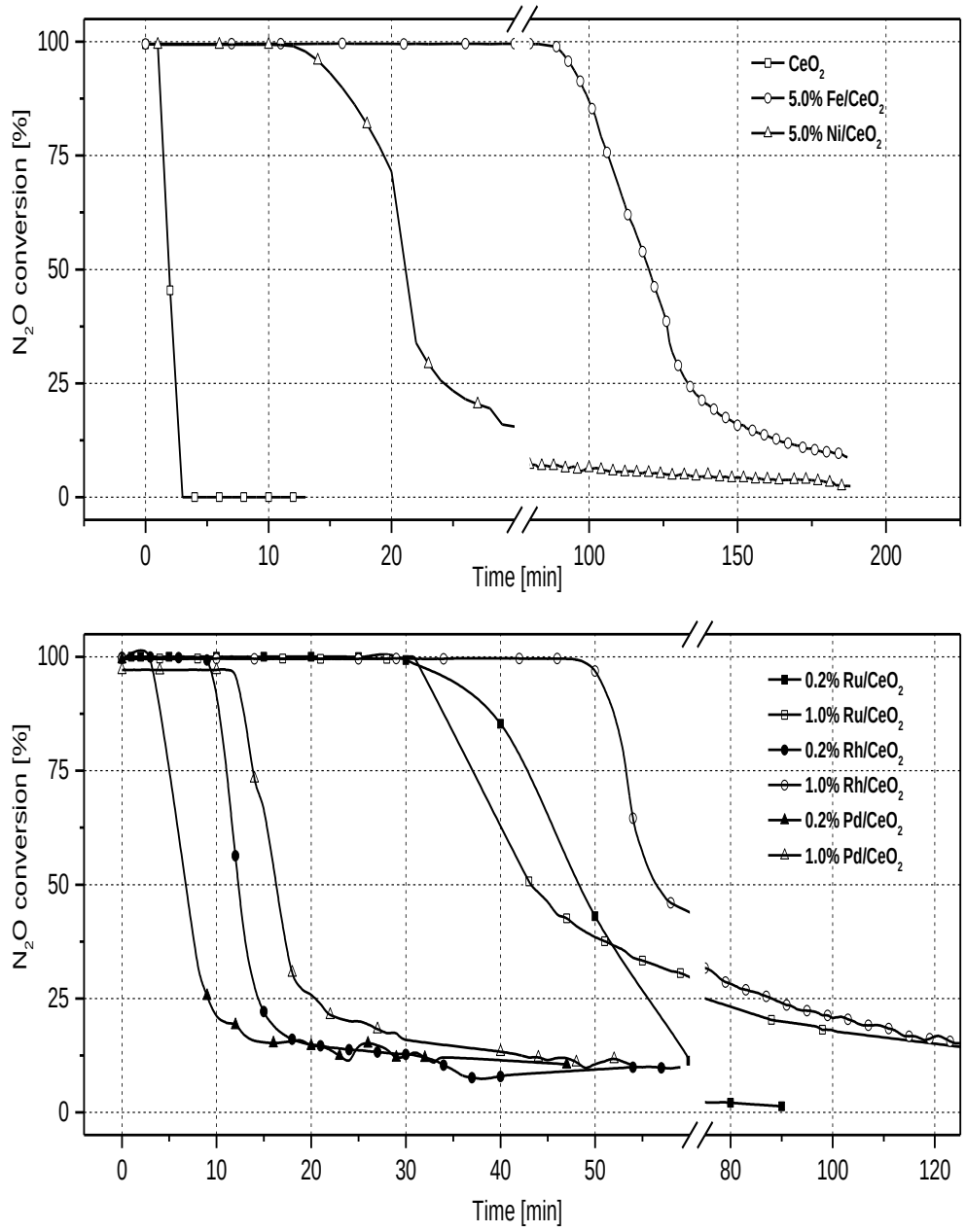

Figure 3.5: Room temperature reaction of N_2O with different transition metals supported on ceria. The samples were prereduced before measurement.

It can be seen that the full N_2O conversion depends both on the active metal species and the loading of the active metal. In general, higher loaded samples show a longer

N_2O conversion. Furthermore, group 10 metals show much shorter conversion compared to group 8 and 9 metals. This trend could be clarified with Pilling-Bedworth ratio. The Pilling-Bedworth ratio was used to determine if the different metals supported on cerium dioxide passivate.[112] A Pilling-Bedworth ratio between 1-2 indicates a passivation on the surface and it provides a protecting effect against further surface oxidation. No protective effect is provided and full oxidation can be reached when the ratio is above 2. The Pilling-Bedworth ratios of Fe, Ru and Rh are 2.15, 2.33 and 2.25, respectively. The Pilling-Bedworth ratios of Ni and Pd are 1.69 and 1.66.[113] It indicates that passivation doesn't happen on the surface of group 8 metals (iron, ruthenium) and the group 9 metal Rh. The whole metals can get fully oxidized during the reaction with N_2O. Group 10 metals Ni and Pd passivate. Only a monolayer of these two metals is expected to be oxidized. This fits quite well to the full nitrous oxide conversion in Figure 3.5. Due to the completed metal oxidation, group 8 and 9 metals achieve much longer conversion time compared to group 10 metals.

3.7 Temperature programmed reduction of ceria supported transition metals by hydrogen

Noble metals supported on ceria show a different profile than nickel or iron supported on ceria (Figure 3.6 and 3.7). For the noble metals one sharp peak in the temperature region 50-200 °C can be found. This sharp peak indicates the complete reduction of the metal oxide (due to calcination after the incipient wetness impregnation) to the metallic active species. The "reducibility" is shift to lower reduction temperature by increased loading of Rh and Pd from 0.2 to 1.0 wt-%. A second, very broad shoulder can be found in the temperature region from 200-800 °C. This peak is assigned to the reduction of surface-capping oxygen of ceria.[110] The stoichiometric reduction of subsurface and bulk ceria to Ce_2O_3 needs much higher temperatures.[108]

As expected, for the nickel and iron samples harsher conditions to reduce the metal oxide are necessary. These samples show only one main peak in the temperature region 300-600 °C. The nickel sample shows two smaller shoulders between 100 and 350 °C due to the reduction of outmost layer nickel oxide.[109]

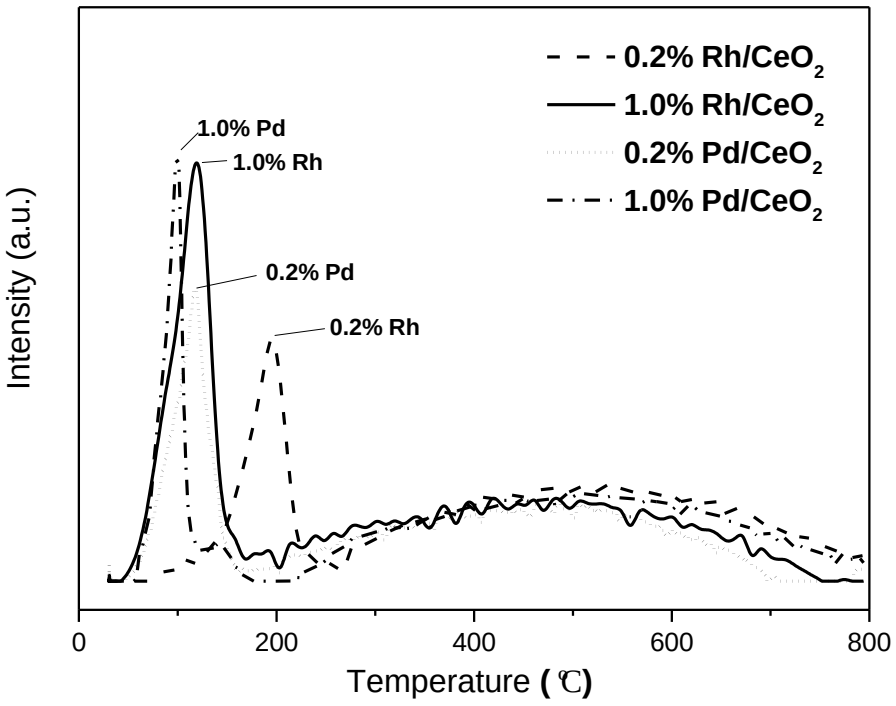

Figure 3.6: H_2-TPR profiles of the fresh noble metal oxides supported on CeO_2

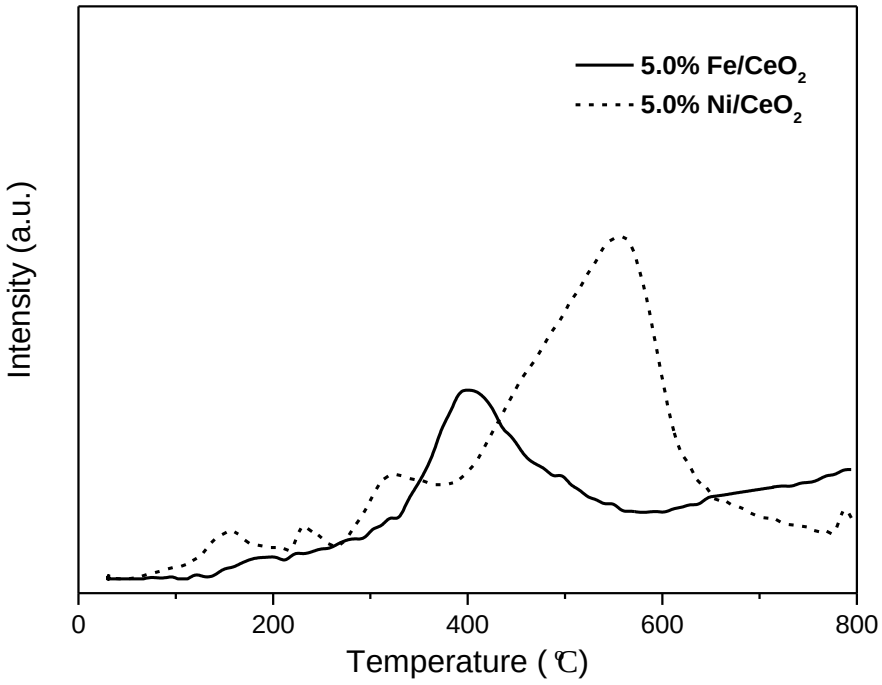

Figure 3.7: H_2-TPR profiles of the fresh non-noble metal oxides supported on CeO_2

3.8 Quantification of TPR profiles and N_2O conversion

The amount of hydrogen consumed during the TPR was quantified. For the noble metals, the two peaks (RT-220 °C and 220-800 °C) were also integrated separately to differentiate the amount of consumed hydrogen by the active metal and the support. The theoretical value for the total reduction of the metal oxide was also calculated by the loading of the active metal and the assumed oxidation state after calcination (Table 3.3).

The total hydrogen uptake of the noble metals supported on ceria decreases with decreasing oxidation state of the metal. A lower oxidation state of the active metal needs consequently less hydrogen to get fully reduced to the metallic species. The hydrogen uptake of the support (220-800 °C) is around 0.2 mmol in all noble metal samples. This means that around 15 % of the CeO_2 are reduced to Ce_2O_3. According to the BET surface area of unsupported cerium dioxide (55 $m^2 \bullet g^{-1}$), a particle size of around 15 nm can be calculated. Assuming spherical particles, the ratio of surface to bulk could be around 0.15.[114] TPR results have shown that around 15 % of cerium dioxide are reduced. It indicates that around one monolayer of cerium dioxide is reduced.

Comparison between the calculated value for the hydrogen uptake of the supported metal and the measured one (RT-220 °C) shows a strong mismatch. Especially for the lower loaded samples (0.2 wt-%) the measured hydrogen consumption is much higher than the calculated values. For the higher loaded samples (1.0 wt-%) the measured values fit better to the calculated one, although the calculated values are at least a little bit smaller than calculated. This indicates, that especially for lower loaded samples in the temperature region between room temperature and 220 °C not only active metal but also support is already reduced. Also it has to be taken into account that the theoretical value was calculated by an estimated oxidation state. Possibly, the oxidation state is higher than the assumed value. A higher oxidation state would increase the amount of consumed hydrogen of a full reduction.

In contrast to the supported noble metals, the amount of consumed hydrogen increases with decreasing oxidation state for iron and nickel samples. For the iron sample it has to be mentioned that the measured total amount of hydrogen consumption is smaller than the calculated amount to reduce the metal oxide

stoichiometrically. Also here, the oxidation state after calcination, and with this the calculated hydrogen uptake, was assumed. An mixed iron(II)- iron(III)-oxide would fit to the calculated value to reduce iron stoichiometrically. For the nickel sample the hydrogen uptake is larger than the calculated value, indicating similar to the noble metal samples a partial reduction of the support. Nickel is well known as classic hydrogenation catalyst indicating a quite good performance in hydrogen activation, at least better than iron.

Table 3.3: H_2-TPR quantification. For the noble metals hydrogen consumption is given separate for the metal and the support. The hydrogen consumption for the metal was also given as theoretical value calculated with the loading and the presumed oxidation state of the metal after calcination.

Sample	assumed oxidation state	n(H_2) total measured (mmol)	n(H_2) metal measured (mmol)	n (H_2) ceria measured (mmol)	n (H_2) metal calculated (mmol)
0.2% Ru/CeO_2	4	0.322	0.107	0.215	0.020
1.0% Ru/CeO_2	4	0.324	0.108	0.216	0.099
0.2% Rh/CeO_2	3	0.271	0.067	0.204	0.013
1.0% Rh/CeO_2	3	0.283	0.120	0.163	0.069
0.2% Pd/CeO_2	2	0.229	0.080	0.149	0.009
1.0% Pd/CeO_2	2	0.255	0.065	0.190	0.047
5.0% Fe/CeO_2	3	0.512	-	-	0.672
5.0% Ni/CeO_2	2	0.744	-	-	0.428

The amount of converted N_2O was calculated by integration of the conversion plot assuming a constant N_2O gas flow into the reactor. These results were compared with the TPR results. Assuming a stoichiometric, not catalytic reaction, the amount of converted N_2O can't be larger than the amount of hydrogen consumed during TPR.

It can be seen that in general the amount of converted N_2O is smaller than consumed hydrogen during the TPR. This is a further indication that the room temperature reaction is a real stoichiometric reaction and no catalytic decomposition. Only the 1.0% ruthenium sample converts slightly more N_2O than the reduction equivalent measured before. Probably, the oxidation state of ruthenium is slightly higher after the calcination. It can be further seen that the amount of converted N_2O of the lower

loaded noble metal samples is roughly the amount of consumed hydrogen during TPR in the temperature region between room temperature and 220 °C. For these samples, N_2O oxidizes not only the supported metals back to metal oxides but also ceria, mainly surface layers Ce_2O_3. For the higher loaded group 8 and 9 samples (Fe, Ru, Rh) a nearly complete back oxidation can be seen. Both group 10 samples (Ni, Pd) show only partial back oxidation. This is in accordance to the Pilling–Bedworth ratios of different metals and also to the XRD results. It supports the idea that the metal plays a role as catalyst not only for the pre-reduction of CeO_2, but also for the re-oxidation of Ce_2O_3.

Table 3.4: Comparison quantitative amount of hydrogen consumed during TPR and converted N_2O.

Sample	**n(H_2) (mmol)**	**n(N_2O) (mmol)**
0.2% Ru/CeO_2	0.322	0.108
1.0% Ru/CeO_2	0.324	0.262
0.2% Rh/CeO_2	0.271	0.079
1.0% Rh/CeO_2	0.283	0.307
0.2% Pd/CeO_2	0.229	0.086
1.0% Pd/CeO_2	0.255	0.108
5.0% Fe/CeO_2	0.512	0.511
5.0% Ni/CeO_2	0.744	0.128

3.9 Conclusion

The outstanding activity of transition metals supported on CeO_2 catalysts in the abatement N_2O has been successfully achieved. The catalysts pre-reduced in hydrogen at 500 °C exhibit high steady-state activities already at room temperature with N_2O for a limited time. The reaction of N_2O over the pre-reduced Ru/CeO_2 can happen at room temperature. Pre-reduced cerium oxide as well as supported transition metal nano-particles react efficiently stoichiometrically with N_2O. It was experimentally verified that the highly interesting transformation of N_2O to N_2 at room temperature over pre-reduced CeO_2-based catalysts does not represent a catalytic decomposition of N_2O, but a stoichiometric reduction of N_2O by Ce_2O_3 and transition metals. Transition metal oxides and surface layers of CeO_2 are reduced by H_2

pre-reduction. The reduced sites of CeO_2, i.e. cerium(III) oxide species represent the highly active accessible reducing sites for N_2O at room temperature. The transition metals act as catalysts for the stoichiometric reduction of N_2O by Ce_2O_3 and provide additional reactive sites for N_2O reduction. Metallic transition metals supported on CeO_2 can be partially oxidized by N_2O at room temperature too. The lifetime of the catalysts is determined by the stoichiometric consumption of the supported metals and the Ce_2O_3 support.

Chapter 4

Selective catalytic reduction of N_2O with H_2

4.1 Introduction

Selective catalytic reduction (SCR) is the technique to reduce the amount of nitrogen oxide gases, mainly nitrogen monoxide and nitrogen dioxide in the exhaust of vehicles and industrial plants, in particular power stations. Ammonia is preferably used as reducing agent. Nitrogen oxides are reduced selectively to nitrogen and water vapor, side reactions like oxidation of sulfur dioxide are suppressed. Thereby, the reaction is a comproportionation of nitrogen oxide gases and ammonia to nitrogen. Two types of catalysts are used mainly. A zeolite based system and a mixed oxide containing titanium dioxide, vanadium pentoxide and tungsten oxide are used as SCR catalyst.[115, 116]

Since around 20 years ago, SCR catalysts were used for diesel engines of cars and trucks. Urea is used as reducing agent. At elevated temperatures urea reacts to carbon dioxide and ammonia (over isocyanic acid) (Reaction scheme 4.1-2). At standard conditions (above 250 °C) ammonia reacts with nitrogen oxide to water and nitrogen (Reaction scheme 4.3). Detailed mechanistic studies were done by Nan-Yu Topsøe and Jacob and Grunwaldt et al.[117, 118]

The dosage of urea is quite difficult due to the fact that it has to be set quite exactly. Nitrogen oxide is not reduced completely in case of too low amount of urea. In the other hand, ammonia is not completely converted and so exposed to the environment in case of an overdose.[119]

$$(NH_2)_2CO \longrightarrow NH_3 + HNCO$$

$$HNCO + H_2O \longrightarrow CO_2 + NH_3$$

$$4\,NO + 4NH_3 + O_2 \longrightarrow 4\,N_2 + 6\,H_2O$$

Reaction scheme 4.1: Mechanism of selective catalytic reduction of nitrogen oxide with urea. 1.: Reaction of urea to ammonia and isocyaic acid. 2.: Reaction of isocyaic acid and water to carbon dioxide and ammonia. 3.: Comproportionation of ammonia and nitrogen oxide to nitrogen.

Currently, SCR of NOx by ammonia (NH_3-SCR) has been widely adopted for the control of NOx. However, NH_3 slip and vanadia emissions associated with the NH_3-SCR process have restricted its application.[120-122] The SCR of NOx by hydrocarbons (HC-SCR) also has some disadvantages such as poor activity at low temperatures.[122, 123] As an alternative technology, selective catalytic reduction of NOx by H_2 (H_2-SCR) has recently attracted increasing attention. When H_2 is used as

the reducing agent, the product is H_2O, which is environmentally friendly.[124, 125] Moreover, CeO_2-based catalysts were found to be activated (reduced) by H_2 at high temperature in Chapter 3. It is interesting to investigate the activation by H_2 simultaneously at mild temperature. However, little research has been reported on this topic. In this study, selective catalytic reduction of N_2O were performed with H_2 as reducing agent. Supported Ru, Rh and Fe catalysts were tested between room temperature and 250 °C.

4.2 Selective catalytic reduction of N_2O with H_2

4.2.1 SCR of N_2O with H_2 at elevated temperature by Ru/CeO_2

Hydrogen was introduced during the nitrous oxide reaction at slightly elevated temperatures (75-200 °C). In the first experiment, an excess of hydrogen (20:1) was introduced. Ruthenium on ceria was chosen as catalyst, the sample was pre-reduced under conditions previously described. Full nitrous oxide conversion was found between 75 and 200 °C (Figure 4.1). The sample was exposed to nitrous oxide at least for two hours at each temperature (without hydrogen as reducing agent a full nitrous oxide conversion is reached for only around one hour, Figure 3.5).

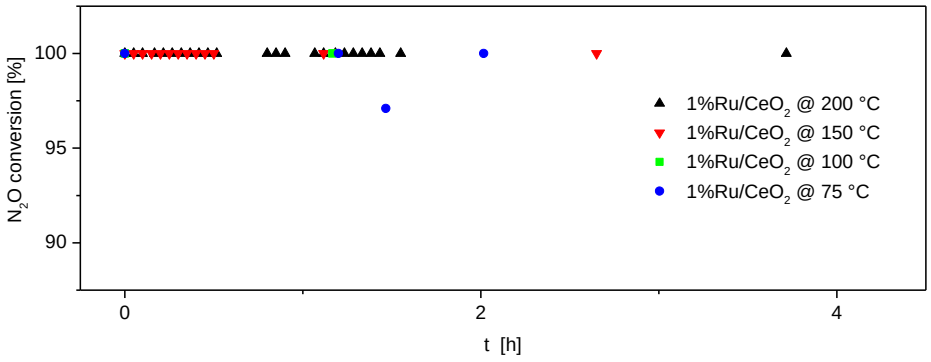

Figure 4.1: Nitrous oxide reaction on Ru/CeO_2 with an excess of hydrogen. Reduction: 10K/ min, 500°C, 1h, 20% H_2 (100 ml/min total flow, He as balance gas). Reaction: RT, 1000 ppm N_2O, 2 % H_2 (100 ml/min total flow, He as balance gas). WHSV = 12000 $mLg^{-1}h^{-1}$. N_2O conversion monitored via FT-IR.

This indicates that the reduction and the oxidation can occur simultaneously. Only 75 °C are needed for a continuous full nitrous oxide conversion (Equation 4.1). This sample shows hydrogen uptake at above 70 °C in the TPR-profile. Nevertheless, it has to be taken into account that this experiment was done with an excess of hydrogen.

$$MO_x/CeO_2 \xrightarrow[500\ °C]{H_2} M/CeO_{2-y} \xrightarrow[25\ °C]{\text{1000 ppm } N_2O,\ \text{excess } H_2} MO_{x'}/CeO_{2-y'} + N_2$$

Equation 4.1: Continous nitrous oxide conversion with hydrogen as reducing agent.

The simultaneous reduction and oxidation can also be written as catalytic reaction of nitrous oxide with hydrogen to form water and nitrogen (Equation).

$$N_2O + \text{excess } H_2 \xrightarrow[75\ °C]{[1\%Ru/CeO_{2-y}]} N_2 + H_2O$$

Equation 4.2: Catalytic reduction of nitrous oxide over ruthenium supported on ceria.

4.2.2 SCR of N_2O with H_2 by supported Ru, Rh and Fe catalysts

For further investigations of the continuous conversion with hydrogen as reducing agent, the experiment was done with nearly stoichiometric reduction equivalents of hydrogen (1.5:1). Different samples were tested between room temperature and 250 °C. These samples were exposed to the reaction mixture for at least 2 hours (
The iron sample does not show full nitrous oxide conversion below 250 °C. This is in accordance to TPR results, which show the main hydrogen uptake only above 300 °C. Both noble metals show full nitrous oxide conversion at above 150 °C. Decreasing temperature to 100 or 125 °C leads to decrease in nitrous oxide conversion for the ruthenium sample. This is in accordance to the TPR results. The main hydrogen uptake for the ruthenium sample is at around 150 °C (Figure 3.4). Without excess of hydrogen a full nitrous oxide conversion cannot be reached below 150 °C.

Table 1.1).
The conversion was monitored over the whole time. Due to the fact that the conversion did not change significantly during this period, the average value was chosen as conversion.
Without introducing hydrogen as reducing agent, all tested samples show a significant decrease during this time and finally a deactivation as presented in previous part. The investigated samples (1 wt.-% ruthenium, 1 wt.-% rhodium, 5 wt.-% iron on ceria) were pre-reduced before measurement and cooled down in pure helium gas flow to the set temperature and exposed to the reaction mixture. After each scan, the sample

was cooled down further. During the whole measurement the catalysts were continuously exposed to the reaction mixture.

The iron sample does not show full nitrous oxide conversion below 250 °C. This is in accordance to TPR results, which show the main hydrogen uptake only above 300 °C. Both noble metals show full nitrous oxide conversion at above 150 °C. Decreasing temperature to 100 or 125 °C leads to decrease in nitrous oxide conversion for the ruthenium sample. This is in accordance to the TPR results. The main hydrogen uptake for the ruthenium sample is at around 150 °C (Figure 3.4). Without excess of hydrogen a full nitrous oxide conversion cannot be reached below 150 °C.

Table 1.1: Nitrous oxide conversion after exposing to reaction mixture of 1000 ppm H_2 and 1500 ppm N_2O for two hours at different temperatures. Data given in percentage. WHSV = 12000 $mLg^{-1}h^{-1}$.

temperature [°C]	1% Ru/CeO_2	1% Rh/CeO_2	5% Fe/CeO_2
250	-	-	70
200	100	100	25
150	100	100	-
125	60	100	-
100	24	100	-
75	-	100	-
50	-	100	-
25	-	100	-

Interestingly, the rhodium sample still shows full nitrous oxide conversion at room temperature. This indicates that the rate of reduction of metal and/ or support on the surface is still fast enough to show full nitrous oxide conversion also at room temperature.

Switching off hydrogen leads to oxidation of the sample. A complete oxidation (and so no more nitrous oxide conversion) is observed after 30 minutes. Interestingly, switching on hydrogen at room temperature leads to full nitrous oxide conversion for the rhodium sample after a short induction period (< 5 minutes) and so no more nitrous oxide can be found in the exhaust. This indicates the very good performance of rhodium as hydrogen activation catalyst and especially as SCR catalyst for the reduction of nitrous oxide with hydrogen. Furthermore, this indicates that the reductive pretreatment is not necessary for this catalytic reduction.

To verify the assumption that the reductive pretreatment is not necessary, the rhodium catalyst was also tested as fresh, calcined species. Also, rhodium supported on alumina was tested to check if a reducible support is necessary for this reaction.

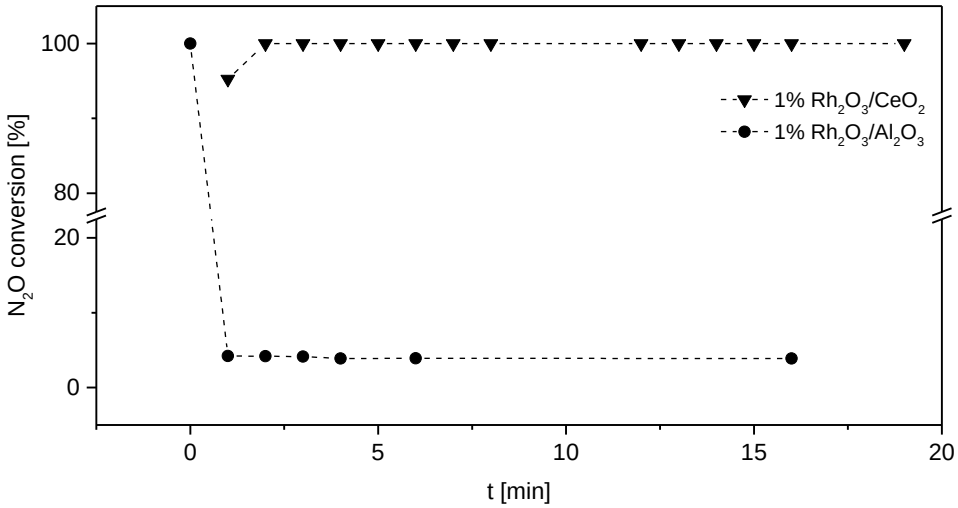

Figure 4.2: Catalytic reduction of nitrous oxide with rhodium supported samples. No pretreatment, samples used directyl after calcination. Reaction: RT, 1000 ppm N_2O, 1500 ppm H_2 (100 ml/min total flow, He as balance gas). WHSV = 12000 $mLg^{-1}h^{-1}$. N_2O conversion monitored via FT-IT.

The ceria supported rhodium shows full nitrous oxide conversion at room temperature after a short induction period, while the alumina supported sample deactivates immediately (Figure 4.2). This validates the finding of the previous experiment that the reductive pretreatment is not necessary. A second finding is the fact that the reducibility of the support is necessary for the SCR of nitrous oxide at room temperature. It looks like the metal oxide stays during the reaction as oxide and catalyzes the reduction of nitrous oxide. Nevertheless, a partial reduction of smaller particles is also possible. To prove this, powder XRD patterns were taken of the rhodium supported on alumina and ceria catalysts (Figure 4.3). The patterns were taken after the reaction with nitrous oxide and hydrogen (transferred under atmospheric conditions). For the ceria supported sample, the activated (pre-reduced) and the non-activated (calcined) samples were measured (both after nitrous oxide reaction). Both ceria supported samples show reflexes according to rhodium(III)-oxide (34.5, 48.9 °). Interestingly, the alumina supported sample shows reflexes according to rhodium(IV)-oxide (28.1, 55.8 °). This indicates at least a partial oxidation of the supported metal. This fits to the finding of a short initial nitrous oxide conversion before deactivation (Figure 4.2).

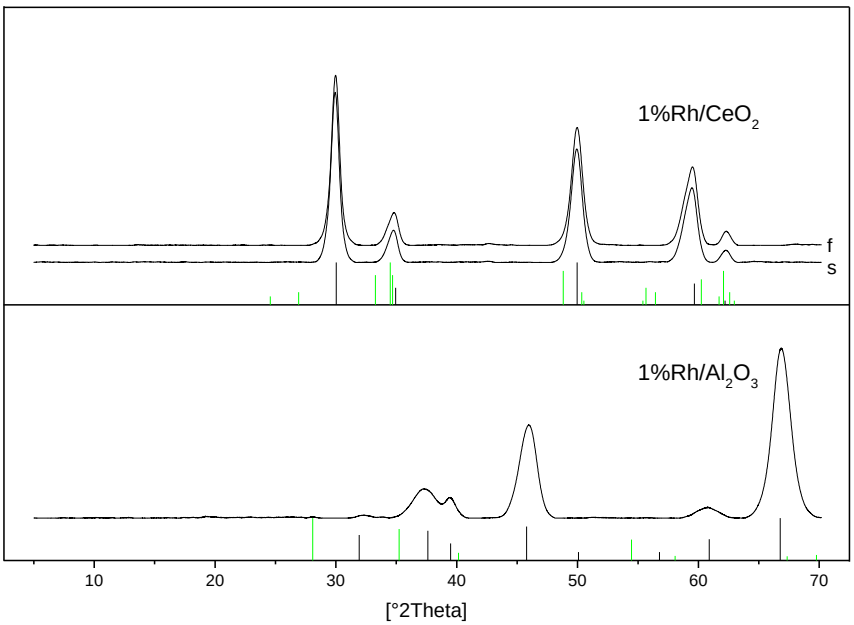

Figure 4.3: Powder-XRD pattern of rhodium supported on ceria and alumina. 20 min, 5-70 °2 Theta. Reference pattern: Black: support; green: Rh_2O_3 (CeO_2), RhO_2 (Al_2O_3).

Due to the fact that there is at least for the ceria sample no change in the supported metal, the reducibility of the support is necessary for this reaction. Nevertheless, it has to be mentioned that the sample was transferred under atmospheric conditions. An oxidation during the transferring is also possible. A reduction of smaller rhodium particles which cannot be seen in the XRD is possible, too. Therefore, the active species rhodium oxide formulated in the following reaction scheme can also be regarded as metallic rhodium particles. More detailed studies will be necessary for a clear distinction of both. A partial reduction of the support during the induction period forms probably the active species (Reaction scheme 4.2.1). Afterwards, nitrous oxide is reduced with hydrogen to nitrogen. (Reaction scheme 4.2.2)

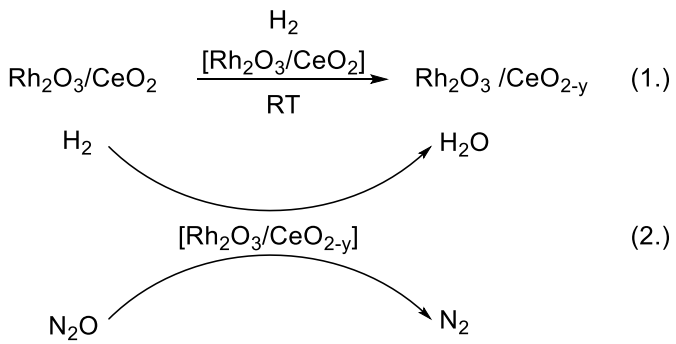

Reaction scheme 4.2: Assumed reaction pathway of the catalytic nitrous oxide reduction over rhodium supported ceria at room temperature. (1) Activation of the catalyst. (2) Reaction of nitrous oxide and hydrogen over the activated catalyst to nitrogen and water.

In addition to the XRD pattern, the BET surface area of the ceria supported SCR samples was also measured (Table 4.2). Both samples were measured after the SCR reaction. For the spent catalyst a reductive pretreatment was done before the SCR reaction, for the calcined catalyst no reductive pretreatment was chosen.

After the stoichiometric reaction, the spent sample shows the smallest surface area (55 m^2/g). It can be assumed that the spent sample shows a full back oxidation of the support. The SCR sample without reductive pretreatment shows a slightly increased surface area (64 m^2/g). For this sample a slightly reduced support can be assumed. The SCR sample with reductive pretreatment before the SCR reaction shows the largest surface area (88 m^2/g). This sample probably shows also the highest reduction degree of the support.

Table 4.2: Comparison of the BET surface area of the samples after stoichiometric reactions (calcined, reduced and spent), and the SCR samples (f: without reductive pretretment, s: with reductive pretreatment.). Values given in m^2/g.

1% Rh/CeO_2	**calcined**	**reduced**	**spent**
stoichiometric reaction	75.7	71.8	55.0
SCR	64.4		88.2

In the SCR reaction, the ceria supported rhodium would act as catalyst for the partial reduction of the support and also in the activation of the nitrous oxide. Probably, both abilities are quite important for this reaction. As seen in the TPR section (Table 3.3), rhodium shows very good abilities as hydrogen activation catalyst. As a full nitrous oxide conversion is still reached at room temperature with stoichiometric amount of hydrogen, the performance of this catalyst in nitrous oxide activation is also quite high.

4.3 Conclusion

Experiments according to the selective catalytic reduction of nitrous oxide were performed. These experiments were done with noble metals (ruthenium and rhodium) supported on ceria and alumina. Hydrogen was used as reducing agent. It was found that the ceria supported samples show very good properties in the selective catalytic reduction. A reductive pretreatment is not necessary. The rhodium sample shows full nitrous oxide conversion at room temperature with a (nearly) stoichiometric amount

(of reduction equivalents) of hydrogen. For alumina supported catalysts, no nitrous oxide conversion is obtained at this temperature. This indicates that the reaction takes place at the interface of the support and the metal. Rh-CeO_2 acts in this case as catalyst for the simultaneous reduction and oxidation of the support. XRD pattern indicated that the state of the metal does not change during the selective catalytic reduction.

Chapter 5

Influence of Light on the Decomposition of Nitrous Oxide by Supported Metal Catalysts

5.1 Introduction

5.1.1 Heterogeneous Photocatalysis

The concept of heterogeneous photocatalysis was introduced by Fujishima and Honda in 1972 during their experiment on the separation of water molecules using TiO_2 as the photocatalyst.[126] Since then, TiO_2 became a common material used in heterogeneous photocatalysis studies due to its capability to perform redox reactions on its surface[127]. Photocatalysts such as transition metal oxides or semiconductors in general contain a void region also known as a band gap. Photoexcitation by light irradiation lifts electrons from the valence band up into the conduction band and forms an active site for the photocatalytic processes[128].

Beyer[128] noted that the utilisation of wide bandgap photocatalysts requires UV irradiation for the photoactivation. However, the UV irradiation restricts the amount of light used for photoexcitation and may not be adequate for the photochemical reaction. Fortunately, this weakness can be compensated with the introduction of transition metals onto the support materials. He mentioned that physical ion implantation techniques are required to obtain an effective transition metal-doped photocatalyst. The technique alters and enhances the photocatalytic properties of the original catalyst with the addition of reaction sites, which promote more redox reactions to occur. However, the insertion of transition metals onto the support material by impregnation technique might not be practical due to the formation of an "impurity energy level". The presence of the "impurity energy level" could become a potential recombination site for the electron-hole pair and lowers the photocatalytic capability of the catalyst. Despite the disadvantage, the impregnation technique remained popular due to its simplicity. Figure 5.1 is extracted from the study performed by Beyer.[128]

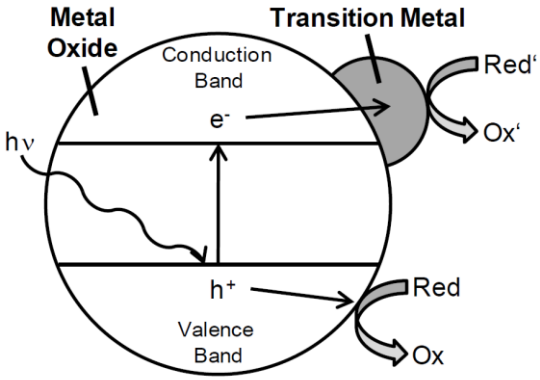

Figure 5.1: Schematic diagram of a photocatalyst doped with a transition metal[128].

Beyer also reported on two reactor concepts published by Lim et al[129], which can meet the difficult demands of the purification processes on industrial exhaust gases. The two reactors were designed specifically for the photocatalytic decomposition of NO by TiO_2. Figure 5.2 is extracted from the study performed by Beyer.[128]

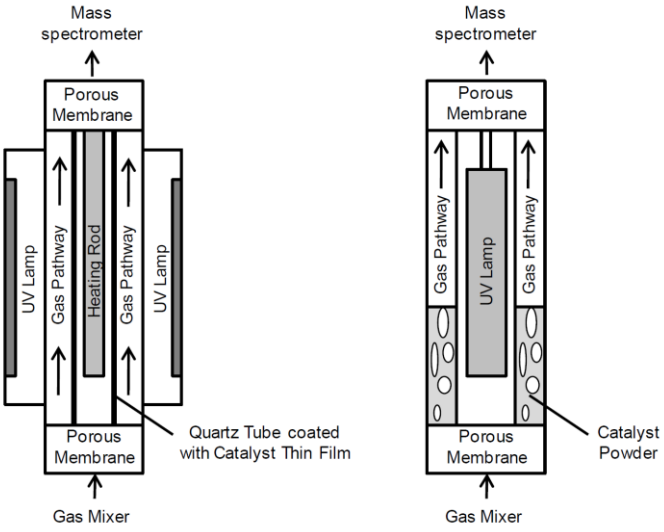

Figure 5.2: Schematic diagrams of the two reactor concepts for the photocatalytic decomposition of NO proposed by Lim et al.

The general mechanism for the photocatalytic decomposition of N_2O had been suggested and mentioned by Kočí et al.[130]. The mechanism was discussed with Ag/TiO_2 as the photocatalyst for the decomposition process.

Photons generated from the light irradiation initiates the formation of the negatively-charged electrons (e^-) into the conduction band and the positively-charged holes (h^+) into the valence band. In general, the charged electron-hole pair recombines and degenerates as heat energy. However, the phenomenon can be inhibited with the presence of the transition metals being adsorbed onto the catalyst surface. The decomposition process then proceeds with the reaction between the generated electrons and the N_2O molecules being adsorbed onto the catalyst surface, forming N_2 gas and oxygen radicals ($^{\bullet}O^-$). Kočí et al. noted that the utilisation of UV light allows the rate-limiting desorption of the oxygen species to proceed under ambient conditions. In particular, there are two reaction routes for the desorbed oxygen species to proceed to the decomposition of the N_2O molecules: (i) reaction with the positively-charged holes to form O_2 gas or (ii) reaction with a new N_2O molecule to form N_2 and O_2. The reaction selectivity varies under different reaction conditions and catalysts used.

Additionally, Cunningham et al.[131] stated that the intermediate products generated from light irradiation might also increase the N_2O decomposition rate by decomposing more N_2O molecules via various reaction routes with photoexcited electrons and holes.

Photocatalytic studies on supported Ag catalysts have always been a subject of interest due to the potential photocatalytic capabilities of the light sensitive Ag (compounds). Obalova et al.[132] conducted the decomposition of N_2O using $Ag\text{-}TiO_2$ thin films and discovered that Ag loading has a positive influence on the decomposition process. The amount of Ag loading is also found to be a potential factor affecting the decomposition process. Kočí et al.[130] studied the photocatalytic decomposition of N_2O using the Ag/TiO_2 of various Ag loadings (0.7%, 2.4%, 3.4%, 5.2% Ag) and found that the photocatalytic activity increases with the Ag loading. However, the photocatalytic activity decreases upon reaching a threshold with Ag loading higher than 3.4%. The increase in

the photocatalytic activity could be explained with the better charge separation efficiency between the holes and electrons generated from the light irradiation by the Ag nanoparticles and clusters. It is also noted that the presence of water vapour (H_2O) and oxygen (O_2) act as an inhibitory agent in the decomposition process as well.

Sano et al.[133] reported that the synthesis method of supported Ag catalysts synthesized by various techniques can also be a deciding factor in their photocatalytic activity. The catalytic activity of the catalyst synthesized via photo-deposition reduced more rapidly as compared to the catalysts prepared from the impregnation method and deposition-precipitation. The decomposition of N_2O was conducted along with the presence of methanol and water vapour. Sano et al. noted that the decomposition rate could also be influenced by the Ag species doped onto the catalysts. Matsuoka et al.[134] also studied the decomposition of N_2O using Ag/ZSM-5.

Reducing agents were also added into the photocatalytic studies on the decomposition (reduction) of N_2O. Kudo et al.[135] studied the decomposition / reduction of N_2O using metal-supported TiO_2 with the introduction of water vapour (H_2O) and methanol (CH_3OH) vapour. The relationship between the N_2O reduction process and the water reduction potential was established due to the formation of H_2 from the photoreduction process of the water vapour and resulted in an enhancement of the photocatalytic activity. Ag-, Cu- and Pt-TiO_2 was known for their photocatalytic capability. However, the latter was found to be inactive in the experiment due to the reaction selectivity towards the H_2 reduction process. Ag/TiO_2 was found to be the most active in the decomposition process with methanol vapour.

Additionally, supported Ru catalysts also can function as a potential photocatalyst in various applications. Ouyang[136] reported on the enhanced photocatalytic properties of TiO_2 with the introduction of Ru components and showed that the improved photocatalytic capability is similar to that of a better photocatalyst as supported Pt photocatalyst. Supported Ru catalysts were also involved in other photoinduced reactions such as the photocatalytic oxidation of organic compounds with ruthenium(II)-pyridylamine complexes[137].

5.1.2 Fermi Level and Schottky Barrier

Fermi Level

The concept of Fermi level is commonly applied in electrochemistry and photochemistry. The Fermi level of a semiconductor can be determined by using the following equation below. The equation is extracted from the study performed by Subramanian et al.[138]:

$$\mathrm{E_F} = \mathrm{E_{CB}} + \mathrm{KT}\, ln \frac{\mathrm{n_c}}{\mathrm{N_c}} \qquad (5.1)$$

E_F: $Fermi\ Level$

E_{CB}: $Conduction\ Band\ Energy\ Level$

K: $Boltzmann\ Constant$

T: $Absolute\ Temperature$

n_c: $Density\ of\ accumulated\ electrons$

N_C: $Charge\ carrier\ density\ of\ the\ semiconductor$

Subramanian et al. noted that the shift in Fermi level towards negative potentials could enhance the efficiency of the charge separation for better photocatalytic activity. He also pointed out that the negative shift in the Fermi level is due to the accumulation of photoelectrons in doped semiconductors after photoexcitation. Jakob et al.[139] studied the change in Fermi level using TiO_2 doped with Au (gold) nanoparticles. He mentioned that the doping of the metals into the semiconductors results into the Fermi level equilibrium and the equilibrated Fermi level of the two materials will be shifted closer to

the conduction band of the semiconductor. The phenomenon is caused by charge distribution between the metal and semiconductor due to the Fermi level equilibrium, which increases the capacitance of the Helmholtz layer and the diffuse double layer. The larger Helmholtz capacitance of the metal attracts electrons from the semiconductor and results in a shift of the Fermi level closer to the conduction band of the semiconductor. Obalova et al.[132] also mentioned that such a phenomenon could be observed because of the higher Fermi level of semiconductors relative to the metals.

Schottky Barrier

Figure 5.3 is extracted from the study performed by Khan et al.[140] and shows the formation of the Schottky barrier between the metal and the semiconductor.

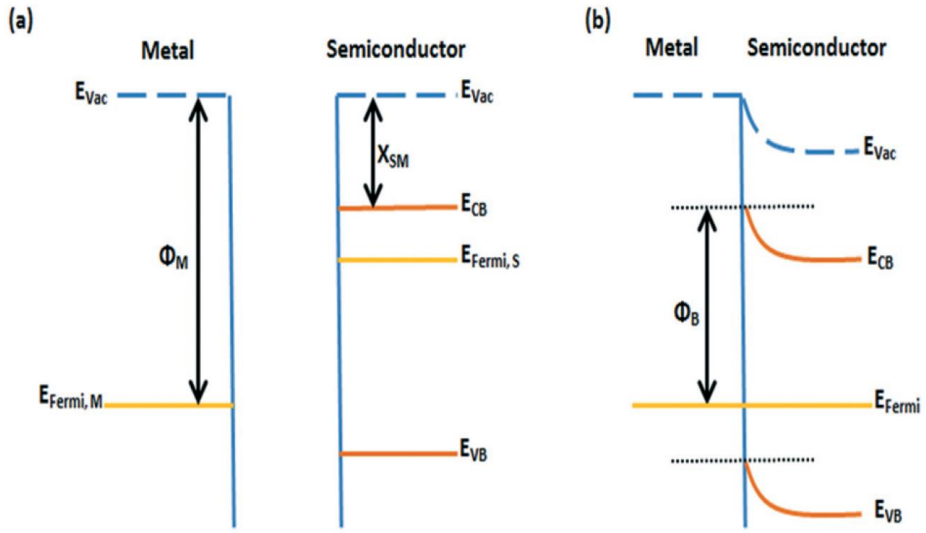

Figure 5.3: Diagram on the formation of a Schottky barrier (a) before interaction between the two materials and (b) after interaction between the two materials.

Φ_M: $Working\ function\ of\ the\ metal$

Φ_B: $Schottky\ Barrier$

X_{SM}: $Electron\ Affinity$

E_{CB}: $Conduction\ Band\ Energy\ Level$

E_{VB}: $Valence\ Band\ Energy\ Level$

$E_{Fermi,M}$: $Energy\ Corresponding\ to\ the\ Fermi\ Level\ of\ the\ Metal$

$E_{Fermi,S}$: $Energy\ Corresponding\ to\ the\ Fermi\ Level\ of\ the\ Semiconductor$

E_{Vac}: $Vacuum\ Energy$

Working function (Φ_M) of the metal is the energy needed for the transfer of an electron from the Fermi energy to vacuum energy; the corresponding energy required for the transfer of an electron away from the metal. Schottky barrier is the potential energy barrier formed in the metal-semiconductor junction. Wang et al.[141] mentioned that the metal-semiconductor junction is a space-charge separation region which involves the contact between a metal and a semiconductor material. In general, the Fermi level of the metals is lower than that of the semiconductors. To achieve stability in the metal-semiconductor junction, the electrons from the semiconductor are transferred into the metal, resulting the Fermi energy of the metal to be increased until both the Fermi energies of the semiconductor and the metal are identical. However, the stability in the metal-semiconductor junction is obtained at the expense of the availability of the electrons in the semiconductors as more electrons are needed to be transferred into the metal due to the presence of the Schottky barrier. The loss of electrons from the semiconductor into the metal cause the formation of a depletion layer in the semiconductor and results in a bent band structure in the semiconductor. The Schottky barrier (Φ_B) can be calculated using Equation 5.2 extracted from the study performed by Khan et al.[140]:

$$\Phi_{\mathrm{B}} = \Phi_{\mathrm{M}} - \mathrm{X}_{\mathrm{SM}} \qquad (5.2)$$

Khan et al. mentioned that the Schottky barrier could be used as an approach to enhance the charge separation between the photo-electrons and photo-holes as the photo-electrons are not able to be shifted back into the semiconductor. The enhancement in the charge separation of the electron-hole pair eventually results in a better photocatalytic activity. The concept of Schottky barrier can also be explained using the work function between the metals and semiconductors. Chiarello et al.[142] studied the production of hydrogen in a photocatalytic process using Pt/TiO_2 and Ag/TiO_2. Chiarello et al. found out that the difference in photocatalytic activities between the two catalysts can be caused by the difference in the work function between the metal and TiO_2. It was mentioned that the larger positive difference in the work function between metal and the semiconductor causes higher charge separation efficiency with the formation of a larger Schottky barrier. It was noted that the work function of Ag has a value of 4.74 eV.

5.1.3 Zeolites & Silica-Alumina

Zeolite is a common material used in various catalytic applications in industry. The unique structural network of zeolites allows them to possess unique physical and chemical characteristics, which enhances the catalytic activities in the various applications. The use of zeolites for industrial applications have expanded rapidly over the years as various efforts and several studies have been conducted to understand and modify them for further potential industrial applications. The amorphous silica-alumina (ASA) has the same chemical composition as zeolites. It is also commonly used for catalytic applications in chemical industry, especially in the petrochemical industry. Unlike the uniform zeolite, ASA contains different types of active sites originating from both the silica and alumina components. Such characteristics cause the ASA to be widely utilised for various Brønsted acid catalysed reactions such as hexane cracking, ethanol dehydration, etc.[143-146]

It is also noted that ASA plays a significant role in photoinduced reactions as well. Yoshida et al.[143] reported on the photoinduced non-oxidative methane coupling using silica-alumina as photocatalyst. Sastre et al. reported on the photocatalytic reduction of CO_2 to methane using a Ni/SiO_2-Al_2O_3 catalyst with a high conversion value of 90% under visible light irradiation.

5.1.4 Fluidization

Fluidization is a process, which involves the contact between a flowing fluid and solid particles. The flowing fluid causes a behavioural change to the solid particles such as the particles act in a fluid-like motion. The process is commonly applied in industries due to advantages such as the rapid mixing of particles and their liquid-like behaviour during the reactor. The rapid mixing process allows uniform particle mixing and removes any minor temperature difference occurring in the reactor. The liquid-like behaviour of the particles allows continuous operation without needing to stop the reaction.[147]

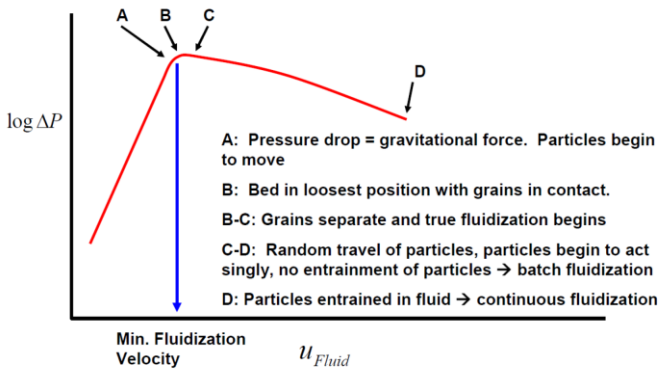

Figure 5.4: Pressure drop diagram with increasing fluid velocity.[148]

To obtain fluidization, a minimum fluidization velocity (U_{mf}) had to be determined first. Figure 5.4 depicts the transition from a fixed bed to a fluidised bed. The catalyst bed experiences a pressure drop across the catalyst bed upon the introduction of a flowing fluid across the fixed bed. At low fluid velocities, the catalyst bed underwent no behavioural change and remained in a fixed bed position. The overall pressure drop

across the catalyst bed increases with the fluid velocity. The minimum fluidization velocity is eventually obtained when the overall pressure drop across the catalyst bed is equal to the overall weight of the catalyst bed. Subsequently, different fluidization stages are obtained as the fluid velocity increased further, as seen in Figure 5.5.

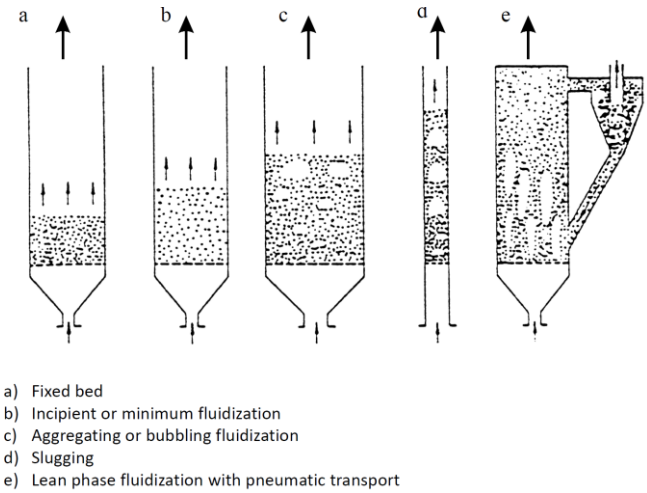

Figure 5.5: Different stages of fluidization.[148]

It was noted that not all particles do possess the same fluidization behaviour upon contact with a flowing fluid. In 1973, Geldart suggested the categorisation of the particles into four different groups of powders. These groups of powders were separated by their particle sizes and the density difference between the particles and the flowing fluid (Figure 5.6).

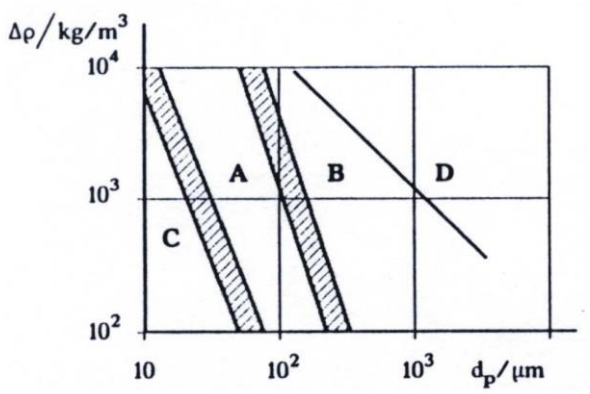

Figure 5.6: Four particle groups proposed by Geldart (1973)[149]

The description of the fluidization behaviour of each particle group can be found below:

Table 5.1: Geldart Particle Categorization and the respective fluidized behaviour description[150].

Particle Group Type	Description
Group A	Fluidization occurs along with the uniform expansion of the catalyst bed as the fluid velocity increases. Cohesive forces between each particle results in the absence of phase separation of the catalyst bed
Group B	Formation of bubbles upon fluidization. Insignificant adhesive forces between the particles and the flowing fluid.
Group C	Low possibility for the observation of fluidized behaviour in the particles due to strong cohesive forces between the particles. Catalyst bed may break into multiple segments with increasing fluid velocity.
Group D	Presence of spouting behaviour from the catalyst bed due to large particle size. Large fluid velocity is often required for fluidization.

5.2 Motivation and Aim

Heterogeneous photocatalysis has always been a subject of interest ever since its discovery. Various efforts in the photocatalytic field have been applied and developed rapidly over the years, resulting in the potential expansion into industrial scale. However, the majority of the photocatalytic studies only deal at ambient conditions. Hence, photocatalytic technologies are not commonly applied in industry as the process may not be able to meet the industrial demands.

The primary objective of the present study is to investigate the influence of light irradiation on the catalytic decomposition of N_2O using supported Ru and Ag catalysts. The experimental procedure and reaction parameters applied resemble the conventional approach for the (thermal catalytic) decomposition of N_2O. The experiments will be conducted under increased temperatures relative to the conventional photocatalytic process, which are generally performed under ambient conditions.

The objective of this investigation is to evaluate if light irradiation can principally promote the catalytic decomposition reaction of nitrous oxide. Hence, the reaction conditions conducted in this study will be similar to those of a typical decomposition reaction, i.e. high reactant concentrations, the rather short contact times between the reactant and the catalyst, and increased reaction temperatures.

5.3 Experimental Procedures

5.3.1 Experimental Setup

The experimental set-up used in the present study follows closely to the experimental design and procedures stated from Beyer[128] to form the foundation of the present study. Experimental modifications were carried out accordingly due to different measurement criteria.

5.3.2 Design of the Photoreactor for the Decomposition of N_2O

The photoreactor used in the present study was constructed using a standard U-shaped quartz tube (4mm inner diameter) reactor with the addition of an elliptical quartz tube (inner dimensions 4x12mm) (Figure 5.7, extracted from the thesis of Beyer[128]) to obtain a fluidized bed for better light irradiation efficiency onto the particle bed. The thermocouple was placed next to the elliptical tube for temperature measurements in the experimental set-up used in the present study to avoid sample output caused by the fluidized particles.

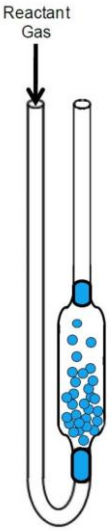

Figure 5.7: Design of the photoreactor.

5.3.3 Design of the Heating Furnace

The heating furnace used in the present study was constructed with a quartz tube from QSIL AG (length = 50cm, inner diameter = 30mm) with the addition of a K-type thermocouple (HTM Reetz GmbH) and heating cord for temperature measurements. Heat insulation was obtained via the installation of insulating ceramic fibre mats (Rath GmbH) before covering it with a stainless-steel jacket. A 4 x 1.5 cm rectangular window

was exposed out from the heating furnace to allow light penetration for the photoinduced reaction.

5.3.4 Light Irradiation for Photocatalysis

Light irradiation was carried out using a commercial 100 W Hg lamp and controlled via a universal arc lamp power supply (L.O.T Oriel GmbH & Co. KG, 50 -100W Universal Arc Lamp Power Supply LSN150). The light beam was concentrated at the rectangular window of the heating furnace for better light irradiation efficiency onto the catalyst. The Hg lamp was placed at a specific distance away from the heating furnace to ensure the heat influence from the light source is negligible. Furthermore, a water filter was placed between the light source and the heating furnace to countermeasure any potential heat influence generated from the light source. The experimental setup was conducted in an enclosed space as a safety measure against the UV light irradiation.

5.3.5 Particle Size Range Determination for Fluidization

In the present experiment, the concept of fluidization is applied to the experimental set-up to allow ample light irradiation onto each catalyst particle. A suitable particle size range had to be determined to obtain proper fluidized behaviour during the experiment.

Pure supports (i.e. H-ZSM-5, P25 TiO_2, SiO_2 – Al_2O_3 (1:3) and γ-Al_2O_3) were sieved into two different particle (grain) size ranges of 100-300 µm and 300-500 µm respectively using a sieving machine. The determination of the particles size range was conducted utilising the photoreactor. The reactor was loaded with a sample mass of 500 mg to observe for the fluidization behaviour. A low gas velocity was initially introduced to observe for sudden behavioural changes to the particles. The gas velocity was increased slowly to a final gas velocity of 100 ml/min to observe for the final behavioural changes of the particles. The particle size range was determined upon reaching the suitable fluidized behaviour for the support material.

5.4 Particle Size Range Determination for Fluidization

The application of the bubbling fluidization in the present study is essential to achieve sufficient light irradiation for each catalyst particle. Literature stated that all particles behave differently upon the contact with a flowing fluid due to the differences in their properties based on the particle sizes and density difference between the particles and the flowing fluid as proposed by Geldart. It has also suggested that the Group B powders had to be obtained to allow the generation of fluidization bubbles and the adhesive forces between each particle can be neglected as well.

Table 5.2: Particle size determination of the various supports for fluidization.

Type of support	Particle Size Range [µm]	
	100-300	300-500
P25 TiO_2	✗[b]	✓[a]
$SiO_2 – Al_2O_3$ (1:3)	✓	✓
H-ZSM5	✗	✓
γ-Al_2O_3	✓	✓

[a] Presence of Bubbling Fluidization.

[b] Absence of Bubbling Fluidization.

The pure supports were subjected to a final flow velocity of 100 ml/min. Results obtained showed that only $SiO_2 – Al_2O_3$ (1:3) and γ-Al_2O_3 could be fluidized for the particle size range of 100-300 µm whereas TiO_2 and H-ZSM5 are unable to obtain a proper fluidized behaviour for that particular particle size range. Cracks were formed in the catalyst bed during the test on a 100-300 µm range of the other two supports. The catalyst bed was broken into multiple parts upon the contact with the flowing fluid. The broken catalyst

bed was lifted as the fluid velocity increased. The phenomenon corresponds to the characteristics of the Group C particles as stated in Section 5.1.4.

In the analysis of the 300-500 μm supports, all four supports were able to obtain the bubbling fluidization as shown in Figure 5.5. The phenomenon also corresponds to the characteristics of a Group B particle.

It is suggested that 300-500 μm particle size range will be utilized for P25 TiO_2 and H-ZSM5 while 100-300μm will be used with γ-Al_2O_3 and SiO_2 – Al_2O_3 (1:3) for the fluidized bed during the decomposition process. It was known that P25 TiO_2 has a specific surface area of 49 m^2/g, while γ-Al_2O_3 has a specific surface area of 129 m^2/g[151]. However, P25 TiO_2 required a larger particle size range for fluidized behaviour and a smaller particles size range for the alumina sample, which contradicts with the fact that the large particle has a smaller surface area. It is suggested that the phenomenon could be caused by stronger adhesive forces of P25 TiO_2 particles as compared to γ-Al_2O_3.

5.5 Influence of light on the decomposition of N_2O by supported ruthenium catalysts

5.5.1 De-N_2O Analysis of 1wt% Ru/Al_2O_3

(a) Influence of Light on the De-N_2O Process under Elevated Reaction Temperatures

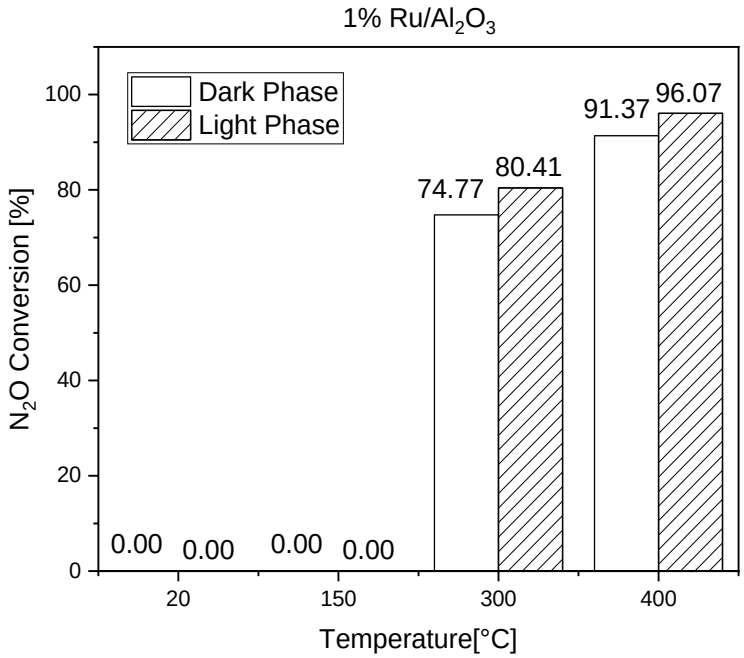

Figure 5.8: Decomposition of N_2O by 1wt% Ru/Al_2O_3 under different reaction temperatures.

The decomposition of N_2O using 1 wt% Ru/Al_2O_3 was conducted at different reaction temperatures. The absence of N_2O conversion is detected for the decomposition process performed at low temperatures (20°C, 150°C). In contrast, the decomposition process conducted at higher reaction temperatures (300°C, 400°C) demonstrates N_2O conversion throughout the entire experiment. It was suggested that the activation of the catalytic decomposition process was only initiated at a reaction temperatures higher than 300°C.

The irradiation phase for the two high reaction temperatures exhibits a higher N_2O conversion as compared to their respective dark stages. The phenomenon corresponds precisely to the observation described by reports in the literature, whereby the photoexcitation from light irradiation will initiate more N_2O molecules to be decomposed and enhances the N_2O conversion with time.

The light phase for the decomposition process at 300°C has a 6% increase in its N_2O conversion while the light phase for the decomposition process at 400°C has a 4.8% increase in its N_2O conversion. The increase in the N_2O conversion upon photoactivation

is a result of the introduction of the transition metal. The insertion of the transition metal enhances the photocatalytic activity by modifying the light absorption characteristics[152]. Kočí et al.[130] mentioned that light irradiation enhances the slow desorption rate of the oxygen species. With a higher desorption rate of the oxygen species, the decomposition of N_2O can be improved and results in a higher N_2O conversion during the irradiation phase as shown in Figure 5.8.

(b) Influence of Light on the De-N_2O Process at a Specific Reaction Temperature

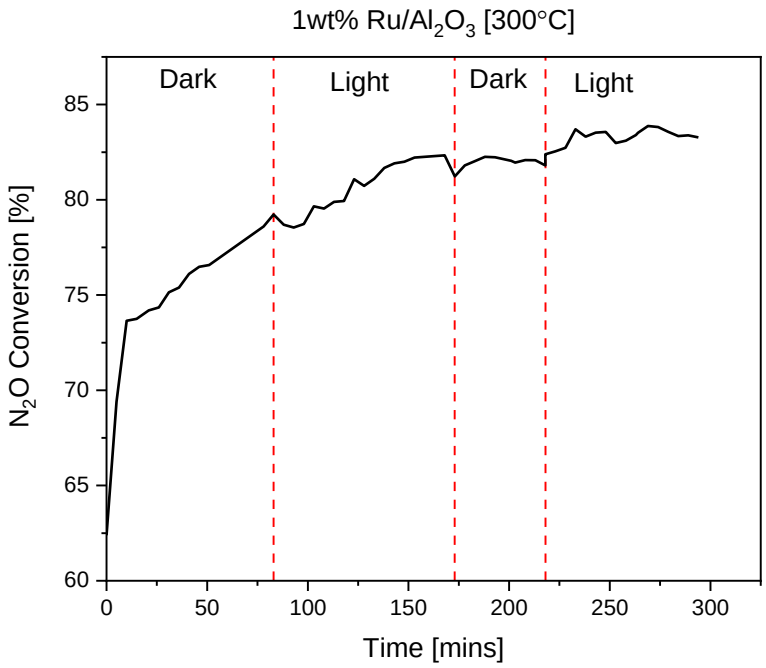

Figure 5.9: Decomposition of N_2O using 1wt% Ru/Al_2O_3 at 300°C.

The influence of light on the de-N_2O process by 1 wt% Ru/Al_2O_3 is further analysed by observing the changes in the N_2O conversion at a specific reaction temperature. The supported Ru catalyst in Figure 5.9 is subjected to a reaction temperature of 300°C with two cycles of light irradiation to ensure the credibility of the results.

The two rounds of light phase for the 1 wt% Ru/Al_2O_3 exhibit a similar N_2O conversion trend, whereby the N_2O conversion increases with irradiation time. The phenomenon supports the assumption that light irradiation enhances the catalytic activity.

A different N_2O conversion trend was observed for the dark phase. The N_2O conversion remained constant upon the termination of light irradiation. A similar pattern was also noted for the N_2O conversion during the second dark phase.

(c) Influence of Light on the Catalytic Activity of Ru/Al_2O_3 with Different Metal Loadings

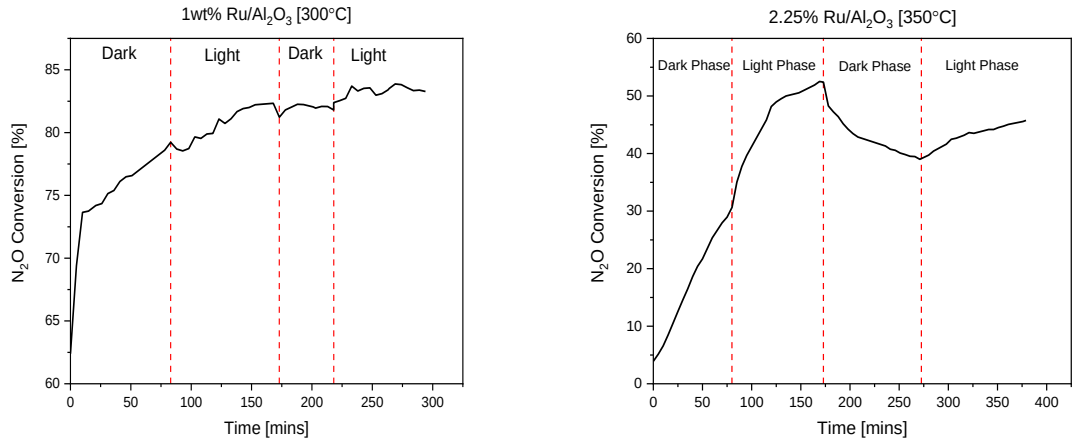

Figure 5.10: De-N_2O process using (a) 1% Ru/Al_2O_3 at 300°C (left) and (b) 2.25% Ru/Al_2O_3 at 350°C (right).

2.25 wt% Ru/Al_2O_3 was synthesised to evaluate and compare with 1 wt% Ru/Al_2O_3. Figure 5.10 shows the N_2O conversion against time for the de-N_2O process using 1 wt% Ru/Al_2O_3 (left) and 2.25 wt% Ru/Al_2O_3 (right). The reaction temperature for the decomposition process varies because a specific N_2O conversion had to be obtained initially to observe the changes brought by the supported Ru catalysts upon light irradiation.

The light phases for both Ru catalysts exhibit a similar trend, whereby the N_2O conversion increases with irradiation time. The phenomenon supports that the light irradiation does impose a positive influence on the catalytic activity.

It is suggested earlier that the catalytic decomposition can be initiated at reaction temperatures higher than 150°C. Since the decomposition process in this segment is subjected to 300°C and 350°C, the catalytic decomposition process should be deactivated upon the termination of light irradiation and the N_2O conversion should

decrease. In contrast, the N_2O conversion trend during the dark phases for the two catalysts behave differently. In Figure 5.10(b), the N_2O conversion for 2.25 wt% Ru/Al_2O_3 decreases with time after light irradiation, which corresponds to the earlier findings. However, the N_2O trend for the 1 wt% Ru/Al_2O_3 remained constant despite the termination of the light irradiation.

The phenomenon of the difference between the Ru catalysts can be explained by two reasons:

Firstly, the constant N_2O conversion trend can be substantiated with the presence of adsorbed oxygen species. Literature stated that the N_2O molecules degenerate as N_2 and oxygen species. As the oxygen species desorbed slower than the N_2 gas, the oxygen species concentration remaining on the active sites increases with time. The high oxygen species concentration subsequently causes an inhibitory effect and terminates the decomposition process. Therefore, the constant N_2O conversion throughout the dark phase for the 1 wt% Ru/Al_2O_3 is caused by the absence of Ru active sites available for the decomposition process due to the domination of the rate-limiting desorption of the oxygen species.

The difference in the Ru loading also causes the difference in the N_2O conversion trend between the two Ru catalysts. As the amount of metal loadings correlates to the amount of Ru active sites inserted onto the support material, the amount of the Ru content for the 2.25 %wt Ru/Al_2O_3 is higher than the 1 %wt Ru/Al_2O_3, forming more Ru active sites present on the catalyst support. Therefore, the slow desorption of the oxygen species imposes a smaller inhibition effect, and the decomposition process was able to proceed further but at a lower efficiency. However, the intensity of the inhibition effect eventually increases as the oxygen species concentration increases with time and corresponds to the decreasing N_2O conversion trend in Figure 5.10(b). The low Ru content in the 1 %wt Ru/Al_2O_3 could not initiate any decomposition of N_2O molecules and results in a stable N_2O conversion throughout the experiment duration. The stable N_2O conversion is due to the available active sites on the support being occupied with oxygen species.

5.5.2 De-N_2O Analysis of 1wt% Ru/TiO_2

(a) Influence of Light on the De-N_2O Process under Elevated Reaction Temperatures

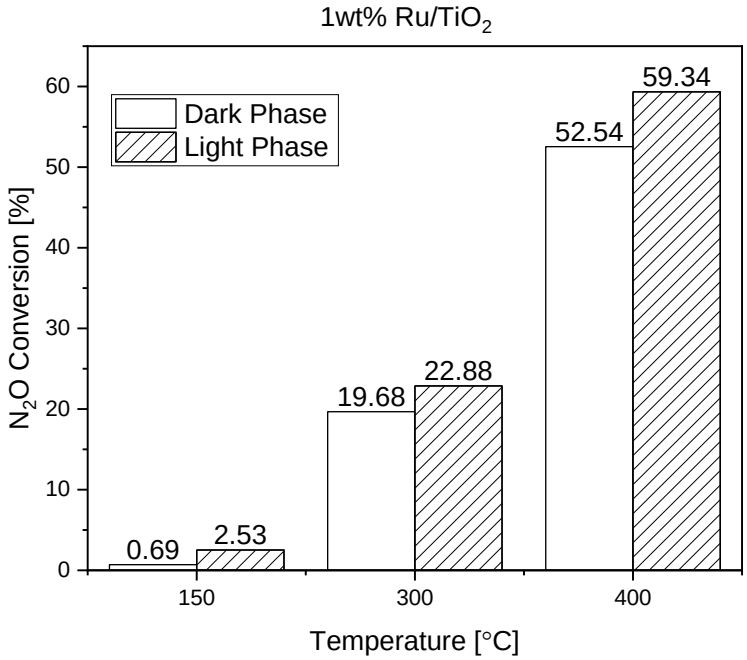

Figure 5.11: Decomposition of N_2O by 1% Ru/TiO_2 at different reaction temperatures.

N_2O conversion is obtained for all reaction temperatures during the decomposition by 1 wt% Ru/TiO_2. It was suggested that the catalytic decomposition via the 1 wt% Ru/TiO_2 could be activated at a temperature higher than 150°C. The irradiation phase for the respective reaction temperature also exhibits an increase in the N_2O conversion. The difference in the N_2O conversion between the light and dark stages increases with temperature as an increase of 1.83 % and 3.2 % in the N_2O conversion was obtained upon light irradiation at 150°C and 300°C respectively.

The presence of N_2O conversion during the dark phase at 150°C suggested the ability of the 1 wt% Ru/TiO_2 to serve as a potential photocatalyst for applications at ambient conditions.

However, the observation of a 0.6% increase on the N_2O conversion during the light phase at 400°C does not support the positive influence of the light irradiation. Photo-deactivation processes may dominate at such high temperatures. The analysis of the N_2O conversion induced by light irradiation at 400°C will be further evaluated for a better insight on the influence of light irradiation on the catalytic decomposition by the TiO_2-based catalysts conducted at higher reaction temperatures, which will be explained later.

(b) Influence of Light on the De-N_2O Process at a Specific Reaction Temperature

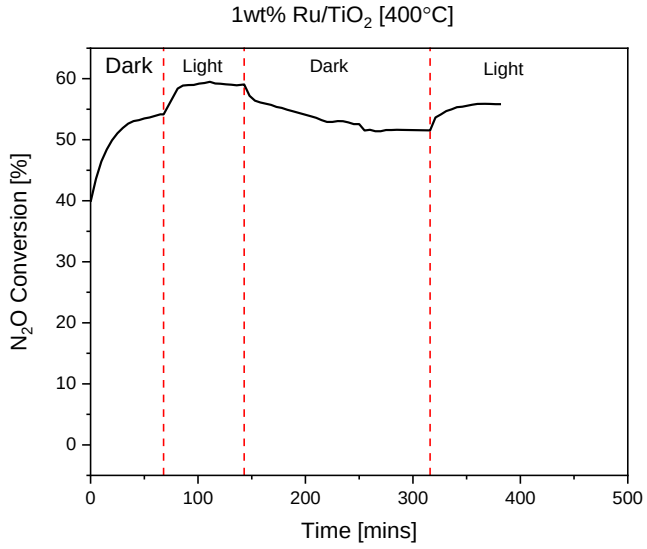

Figure 5.12: De-N_2O process using 1wt% Ru/TiO_2 at 400°C.

It was previously mentioned that the small increase in the N_2O conversion during the light phase in the decomposition reaction at 400°C is not significant to conclude that light irradiation does impose a positive impact on the catalytic activity. The phenomenon can be further evaluated using Figure 5.13. The graph demonstrates two cycles of light irradiation on the same catalyst to ensure the accuracy of the results obtained.

The first light phase demonstrates a noticeable growth in the N_2O conversion, suggesting that the light irradiation at 400°C does induce a positive influence on the catalytic activity. A similar trend is also observed in the second light phase as well. As such, the two similar N_2O conversion growth obtained during the light stages can support

that light irradiation does cause a positive influence on the decomposition of N_2O even at higher temperatures for 1 wt% Ru/TiO_2.

The small growth in the N_2O conversion during the light phase at the reaction temperature of 400°C could be caused by the presence of rutile phase in the TiO_2 sample. Rutile was known for its poorer photocatalytic capabilities compared to the anatase phase. Works of literature noted that TiO_2 exists in three polymorphic forms with the anatase and rutile more commonly used.[153, 154] P25 TiO_2 was used as a support material for the catalyst preparation and its composition consists of 80 % anatase phase and 20% rutile phase. As the original composition of the P25 TiO_2 contains more anatase, the photocatalytic activity should increase. However, the phenomenon was not observed as a phase transition from the anatase phase to the rutile phase could have occurred during the reaction. Additionally, the Ru/TiO_2 was initially calcined at 450°C, and the irreversible phase transition of the anatase phase into the rutile phase could have been triggered as well. Prolonged exposure to the high reaction temperatures during the decomposition process could have also accelerated the phase transition into the rutile phase. Although the common phase transition temperature was known to be at 600°C, there was no distinct temperature for phase transformation to occur. The factors mentioned above could have also resulted in the activation of the phase transition as phase transition at 400°C has also been mentioned in the works of literature as well. Kim et al.[155] reported that the formation of RuO_2 favours more on the rutile phase in a mixture of the anatase and rutile phase.

Another possible reason for the small increase in the N_2O conversion during the light phase is the agglomeration of the TiO_2 particles at high temperatures. Before the decomposition process, the 1 wt% Ru/TiO_2 was sieved to the particle size range of 300-500µm. However, the catalyst was found to be agglomerated after the decomposition process and could explain the small difference in N_2O conversion between the light and dark phase. It is known that a large particle (grain) size can result in a lower photocatalytic activity due to a smaller surface area for light absorption.

5.5.3 De-N_2O Analysis of 1wt% $Ru/SiO_2 – Al_2O_3$ (1:3)

(a) Influence of Light on the De-N_2O Process under Elevated Reaction Temperatures

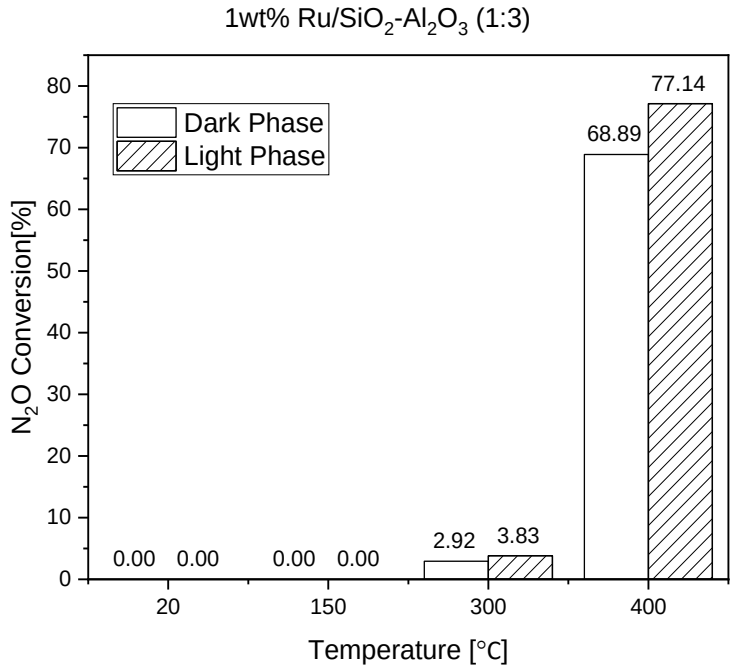

Figure 5.13: Decomposition of N_2O by 1wt% $Ru/SiO_2 – Al_2O_3$ (1:3) under different reaction temperatures.

The activation of the catalytic decomposition of N_2O using the 1 wt% $Ru/SiO_2 – Al_2O_3$ (1:3) is initiated at the temperature of 300°C. However, the efficiency of the catalyst at 300°C was not as high as compared to the other two Ru catalysts reported earlier. However, the catalytic activity at 400°C increased tremendously with an N_2O conversion of 69%. Amorphous SiO_2-Al_2O_3 (ASA) is commonly known for their involvement in the petrochemical industries, which deal with high temperatures, suggesting that the activation of the catalytic activity using the ASA material works only at high temperatures.

It is noted that the difference in the N_2O conversion between the light and dark phase under low reaction temperatures does not imply that the light irradiation imposes a significant influence on the conversion rate. Although the reaction at 300°C shows an increase in N_2O conversion upon light irradiation, such phenomenon can be considered

negligible due to the small N_2O conversion. The influence of light irradiation can only be observed for the reaction at 400°C. The N_2O conversion has an increase of 9% upon light irradiation. As it was previously mentioned that significant result is only observed at high reaction temperatures, it could be suggested that an increase of the number of the active sites is also initiated as well. ASA is known as a Brønsted acid catalyst and the active sites on the catalyst surface act as a proton donor during the catalytic reaction. Therefore, the excess positively-charged particles can enhance the decomposition of N_2O molecules by accelerating the oxidation of the oxygen species and demonstrate an increase in N_2O conversion during the light phase.

(b) Influence of Light on the De-N_2O Process at a Specific Reaction Temperature

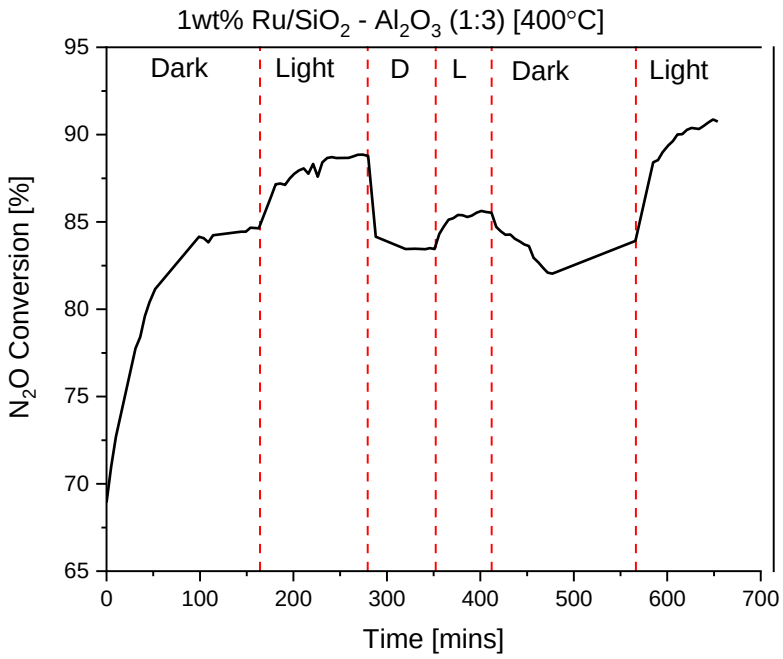

Figure 5.14: De-N_2O process using 1wt% Ru/SiO_2 – Al_2O_3 (1:3) at 400°C.

The decomposition process under 400°C underwent three cycles of light irradiation due to its high conversion rate during light phases to determine the influence of light under high reaction temperature. Similar trend is observed and can be explained with the same explanations as mentioned for the other supported Ru catalysts. However, the difference

between the $Ru/SiO_2 – Al_2O_3$ (1:3) and the other supported Ru catalysts is the increase in the N_2O conversion with the reaction duration. It is observed that the increase in N_2O conversion during the second light phase is lower than in the first light phase, suggesting that the N_2O conversion is decreased due to factors such as agglomeration of the catalyst particles resulting in a smaller surface area and hence lowers the N_2O conversion. However, such a phenomenon is not observed for the $Ru/SiO_2 – Al_2O_3$ (1:3). Since the $Ru/SiO_2 – Al_2O_3$ (1:3) underwent three cycles of light irradiation, it should be assumed that the N_2O conversion should decrease with the number of light cycles. The N_2O conversion was observed to have the highest N_2O conversion growth at the end of the third cycle. The phenomenon seen can be explained with the coupled effect from the activation of the Brønsted acid sites at high temperatures and the increase in the N_2O conversion due to acceleration in the oxidation of the oxygen species upon light irradiation. The ASA is known for its high reactivity at high temperatures, suggesting that the active sites in ASA are activated at higher temperatures. The excess positively-charged particles from the Brønsted acid sites increased the N_2O conversion further by oxidising more oxygen species which are desorbed easily under light irradiation. Therefore, the coupled effect from the two factors results in the high N_2O conversion.

5.5.4 De-N_2O Analysis of 1wt% Ru/ZSM-5

(a) Influence of Light on the De-N_2O Process under Elevated Reaction Temperatures

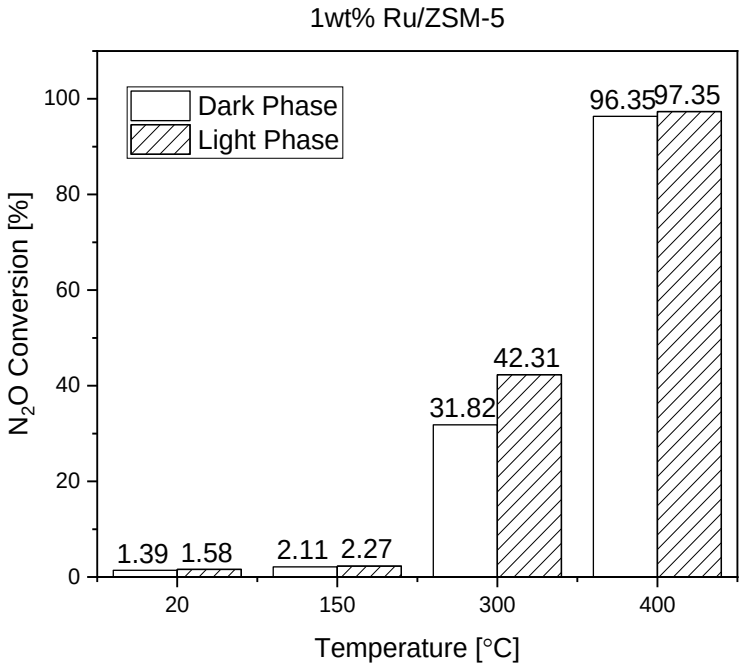

Figure 5.15: Decomposition of N_2O by 1wt% Ru/ZSM-5 under different reaction temperatures.

The potential catalytic decomposition of N_2O using the 1 wt% Ru/ZSM-5 is activated at temperatures higher than 20°C. Although N_2O conversion is also detected at 20°C, the N_2O conversion value can be negligible due to its small conversion value. N_2O conversion became significant upon reaching temperatures higher than 150°C. The dark phases at 300°C and 400°C has a high catalytic activity of 32% and 96%, suggesting that the 1 wt% Ru/ZSM-5 is the most effective catalyst for the catalytic decomposition of N_2O at high temperatures. Although the 1 wt% Ru/ZSM-5 and 1 wt% Ru/SiO_2 – Al_2O_3 (1:3) has the same chemical composition, a different phenomenon is observed within the two catalysts. The 1 wt% Ru/ZSM-5 has a difference of 27 % in the N_2O conversion at 400°C relative to the 1 wt% Ru/SiO_2 – Al_2O_3 (1:3). The results obtained supported that the 1 wt% Ru/ZSM-5 is better than the 1 wt% Ru/SiO_2 – Al_2O_3 (1:3) due to the large difference in the catalytic activity during the decomposition process at 400°C. The significant difference could be explained with their composition. H-ZSM5 was used for the synthesis of the 1 wt% Ru/ZSM-5. The ratio of SiO_2 to Al_2O_3 for H-ZSM5 has a value of 28:1 and the 1 wt% Ru/SiO_2-Al_2O_3 has a ratio of 1:3 for the SiO_2 to Al_2O_3. The significant difference in the ratio of SiO_2 to Al_2O_3 for the 1 wt% Ru/ZSM-5 results in a

more substantial amount of reactive sites available for the decomposition process. The proposed photocatalytic decomposition mechanism of N_2O via the 1 wt% Ru/ZSM5 is shown in Figure 5.17.

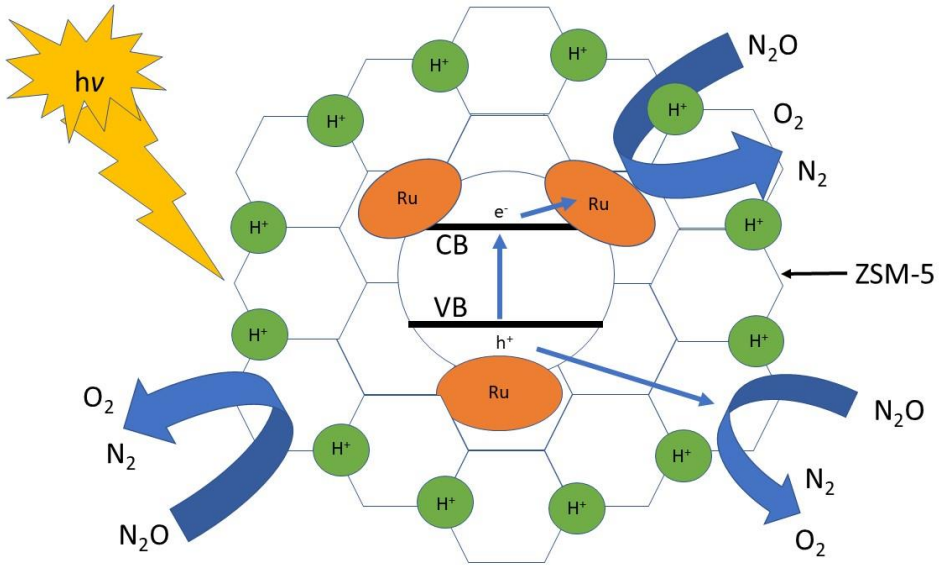

Figure 5.16: Proposed photocatalytic N_2O decomposition mechanism scheme by 1 wt% Ru/ZSM-5.

The light phases at both temperatures exhibited a different phenomenon relative to the dark periods. The reaction at 300°C and 400°C has an increase of 11% and 1% in their N_2O conversion upon light irradiation respectively.

It was mentioned previously that light irradiation at high temperature can result in a better photocatalytic activity for the 1 wt% $Ru/SiO_2 – Al_2O_3$ (1:3) and since it has a similar chemical composition as the 1 wt% Ru/ZSM-5, it is suggested that the 1 wt% Ru/ZSM-5 will exhibit a similar N_2O conversion trend. However, the results obtained for the reaction at 400°C during the light phase is not significant as N_2O conversion has reached its maximum. The reaction at 400°C has an N_2O conversion of 97%, which is also higher than 1 wt% Ru/Al_2O_3 which has a high N_2O conversion of 96% after light irradiation. The influence of light irradiation on the reaction conducted at 400°C will be discussed in the next part.

(b) Influence of Light on the De-N_2O Process at a Specific Reaction Temperature

It was previously mentioned that the low N_2O conversion growth obtained during light phase in the N_2O decomposition reaction conducted at 400°C is not significant enough to support that the zeolite catalysts can perform better at higher reaction temperatures. Figure 5.17 and 5.18 show the N_2O conversion trend at 300°C and 400°C respectively.

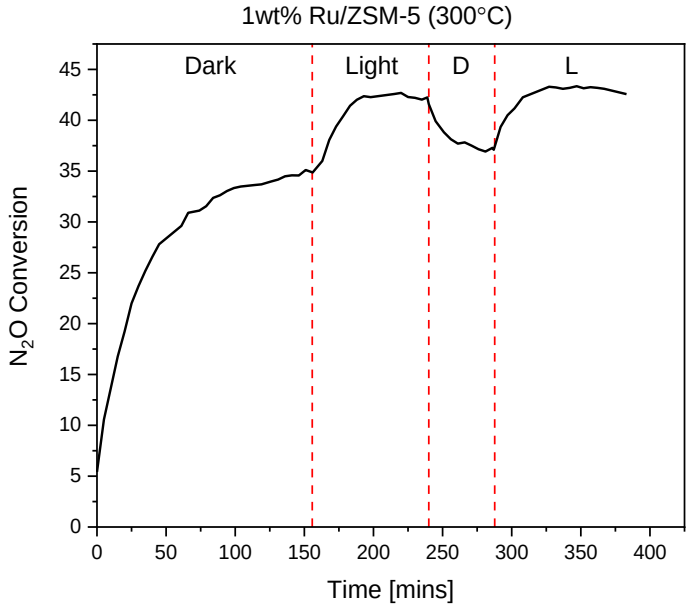

Figure 5.17: De-N_2O process using 1% Ru/ZSM-5 at 300°C without and with light.

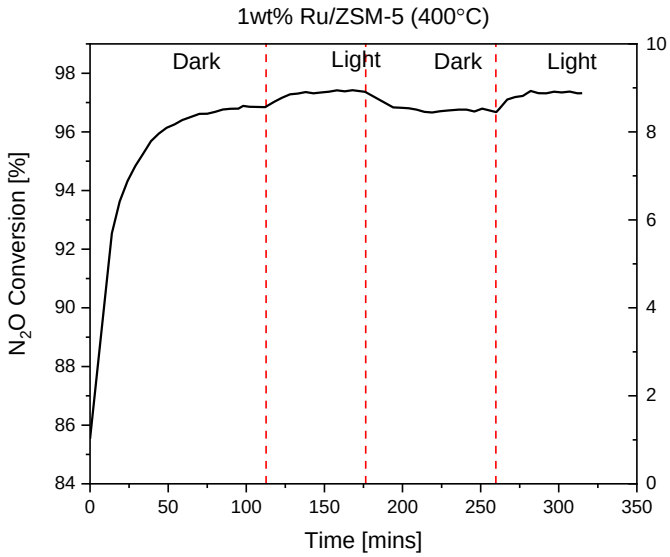

Figure 5.18: De-N_2O process using 1% Ru/ZSM-5 at 400°C without and with light.

The determination of the influence of light on the reaction at 400°C can be discussed with the figure above. Although the difference in the N_2O conversion between the light and dark phases is small, a noticeable growth can be observed in the N_2O conversion plot during the two cycles of light irradiation. Additionally, it could be suggested that maximum N_2O conversion could have been reached with a value of 97%. Therefore, the two factors mentioned above justifies that light irradiation still imposes a positive influence for the 1 wt% Ru/ZSM-5 even at higher reaction temperatures.

5.5.5 Comparison between the supported Ru catalysts

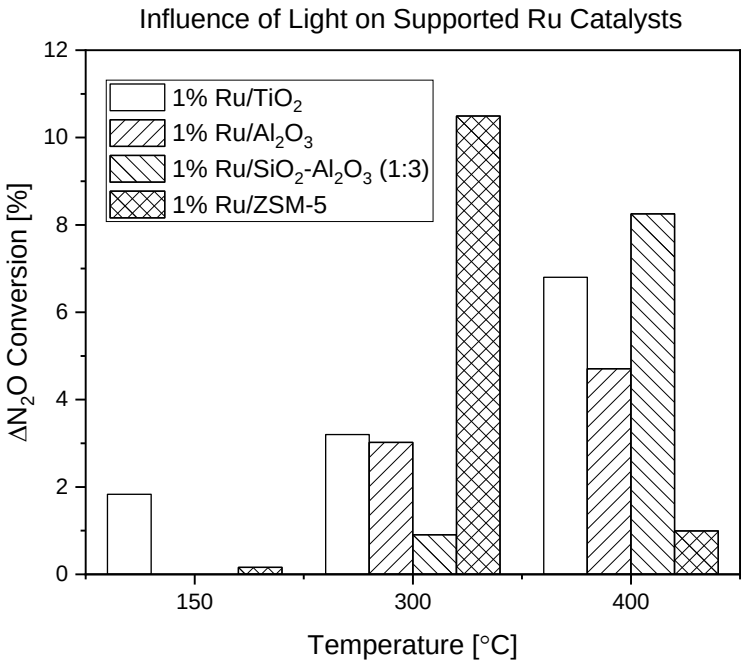

Figure 5.19: Influence of light on the catalytic activities by the Ru catalysts relative to the conversion in the dark (ΔN_2O conversion) at different temperatures.

The y-axis in Figure 5.19 denotes the difference in the N_2O conversion due to the influence of the light irradiation at their respective temperatures. From the temperature range of 150°C to 300°C, the N_2O conversion difference by the supported Ru catalysts increases with time except for the case of 1 wt% Ru/ZSM-5 and 1 wt% Ru/TiO_2 during the decomposition process conducted at 400°C. The different phenomenon exhibited by

the 1 wt% Ru/TiO_2 was explained by the occurrence of a phase transformation in the P25 TiO_2, whereas the 1 wt% Ru/ZSM-5 was due to maximum N_2O conversion being obtained during the reaction at 400°C, causing the N_2O conversion unable to increase further. In summary, it is suggested that the 1 wt% Ru/ZSM-5 is the most effective catalyst for the photocatalytic decomposition of N_2O with the highest N_2O conversion of 97% under light irradiation.

Literature has reported the potential inhibitory effect on the N_2O conversion induced by the presence of oxygen.[65] Although the experimental procedures in the present study did not include the introduction of oxygen gas into the feed gas mixture, the oxygen sensitivity of the supported Ru catalysts can still be studied due to the presence of the oxygen species produced from the decomposition of N_2O. The phenomenon can be explained using the decomposition process conducted at 300°C. Zheng et al.[65] mentioned that the properties of the support material influenced the oxygen sensitivity of the Ru-based catalysts. Ru loaded on supports that are sensitive to oxygen are unable to desorb the oxygen species as compared to those that can desorbed oxygen species easily. This behaviour results in a lower N_2O conversion upon light irradiation as it has been reported earlier on that light irradiation allows the oxygen species to be desorbed more easily and enhances the N_2O conversion further, yet, the phenomenon mentioned was not observed for some supported Ru catalysts. It was suggested that the oxygen sensitivity of the supported Ru catalysts in the presence of light irradiation decreases in the following order: 1 wt% Ru/SiO_2 – Al_2O_3 (1:3) > 1 wt% Ru/γ-Al_2O_3 > 1 wt% Ru/TiO_2 > 1 wt% Ru/ZSM-5.

The order on the oxygen sensitivity of the supported Ru catalysts is also supported by the findings obtained from Zheng et al.

5.6 Supported Silver Catalysts

Matsuoka et al.[134] had previously reported that the presence of Ag^+ ions is responsible for the photocatalytic decomposition of N_2O. 1% loading supported Ag catalysts were synthesized with Al_2O_3, TiO_2, SiO_2-Al_2O_3 mixed oxides and ZSM-5 as supports. The decomposition of N_2O using these catalysts was conducted under the same experiment conditions with supported ruthenium catalysts. However, there is no N_2O conversion detected for all supported Ag catalysts throughout the entire experiment. Additionally, the activation by light irradiation did not promote the decomposition of N_2O molecules further as well. The negative results obtained for the supported Ag catalysts can be explained by several potential causes: (i) reduction of Ag^+ to Ag^0, (ii) phase transition of the anatase phase to the rutile phase, (iii) type of technique used for the synthesis of the supported Ag catalyst, (iv) the influence of different Ag loading amount on the support and (v) the influence of Schottky barrier and Fermi level.

(1) Reduction of Ag^+ to Ag^0

Firstly, the thermal decomposition of the Ag^+ ions into metallic Ag^0 could have taken place during calcination. All the supported Ag catalysts were calcined at 450°C during catalyst synthesis to form Ag_2O from $AgNO_3$, which is impregnated onto the catalyst surface. However, Zhang et al.[156] mentioned that Ag_2O is not thermally stable at high temperatures as the decomposition of the silver compound back into its elemental form can occur at the temperature value of 450°C. Therefore, there is a possibility that the Ag^+ ions could have been reduced into metallic Ag^0 during the heat treatment and decreases the availability of the Ag^+ active sites. Reduction of the Ag^+ into the metallic Ag^0 could have also occurred during the light phase. As it is commonly known that all silver compounds are photosensitive because they decompose readily upon light irradiation, it is possible that the amount of the Ag^+ ions introduced onto the catalyst surface would have decreased tremendously upon light irradiation and contributed to the negative results obtained for the silver catalysts.

(2) Phase Transition of the Anatase Phase to the Rutile Phase,

It has been mentioned earlier in Section 5.5.2 that the transition of the anatase phase to the rutile phase in TiO_2 support will result in a lower photocatalytic activity as it was known that the anatase phase possesses better photocatalytic capability as compared to the rutile phase. Since the Ag/TiO_2 catalyst has been calcined and underwent decomposition process at high temperatures, the activation of the irreversible process would have been activated and contributed to the absence of N_2O conversion. Works of literature have also reported on the possibility of the Ag species to promote the phase transition into the rutile phase to occur[157].

(3) Type of Technique used for the Synthesis of the Supported Ag Catalyst

The introduction of metals onto the catalyst support can influence the charge transfer and separation process during photocatalysis[158]. The technique used in the preparation of the supported Ag catalysts could have caused the absence of N_2O conversion. Beyer[159] mentioned that the introduction of transition metals by impregnation might not be a suitable technique to obtain a better photocatalytic activity. The insertion of the transition metal using the impregnation technique could have promoted the recombination of the electron-hole pair by creating an “impurity energy level” within the original band gap of the support material. The presence of the “impurity energy level” accelerates the recombination of the electron-hole pair and decreases the efficiency of the charge separation and results in poor photocatalytic activity.

(4) The Influence of Different Ag Loading Amount on the Catalyst.

As the three factors mentioned above inhibit the decomposition of N_2O by decreasing the availability of the Ag^+ active sites, the 1 wt% loading may not be sufficient enough to produce a noticeable result. The issue is compensated with a higher Ag loading to determine the efficiency under light irradiation. The Ag catalyst is loaded with an amount of 3.5 wt% as Kočí et al. reported that the optimal loading for Ag/TiO_2 was at 3.4 %, with the conversion of 77 % after 24 hours (990 ppm N_2O/He mixture, volume 756 cm^3, pressure 110 kPa, 0.135 g Ag/TiO_2 powder). The calcination temperature for the synthesis of the 3.5 wt% Ag/TiO_2 is decreased to 200°C as it has been reported that the

stability of Ag_2O is found to be at a temperature value of 200°C. However, the 3.5 wt% Ag/TiO_2 used in the present study was unable to achieve similar conversion as no presence of N_2O conversion is obtained which contradicts with the findings reported by Kočí et al. It could be suggested that 3.5 % of Ag loading could have exceeded the threshold such that an adverse influence is imposed onto the catalyst during photoexcitation. Zhang et al.[160] reported that excessive Ag dopants could result in detrimental effects relative to the positive influence from the formation of the Schottky barrier between Ag and the catalyst support. Excess Ag content may result in an inhibitory effect on the photocatalytic activity as the availability of the active sites used for photocatalysis will be reduced tremendously. The reduction of the Ag^+ ions into metallic Ag^0 may also reduce the amount of light being absorbed by the catalyst and results in low photocatalytic activity.

5.7 Comparison of the influence of light between supported Ru & Ag catalysts

In general, the insertion of transition metals on / into photocatalysts enhance their photocatalytic properties through various modifications such as the reduction of the band gap energy needed for photoexcitation, increase in the charge separation efficiency and facilitating the charge transfer process for the redox reactions occurring at the catalyst surface. The phenomenon caused by the various mentioned factors was exhibited by the enhanced catalytic activity of the supported Ru catalysts upon light irradiation. However, similar behaviour was not demonstrated by the supported Ag catalysts.

5.8 Conclusion

Light irradiation imposed a positive influence on the decomposition of N_2O via the supported Ru catalysts. Additionally, the N_2O conversion during the light phase has demonstrated to be increasing with the irradiation time. The increase in N_2O conversion under light irradiation is a result of the enhanced photocatalytic properties of the catalyst

in the presence of transition metals. Light irradiation allows the rate-limiting oxygen species to be desorbed more easily. The 1 wt% Ru/ZSM-5 is found to be the most effective catalyst in the decomposition process with the highest catalytic activity of 96 % in the absence of light irradiation. A very similar maximum of N_2O conversion of 97 % is also obtained in the presence of light irradiation for the decomposition process using the 1 wt% Ru/ZSM-5. The high catalytic activity is possibly due to the presence of excess reactive sites, which improves the N_2O conversion by accelerating the oxidation of the oxygen species, which can be a rate-limiting factor during the decomposition process. The assumption is supported by the case of the 1 wt% Ru/SiO_2 – Al_2O_3 (1:3). The 1 wt% Ru/SiO_2 – Al_2O_3 (1:3) and 1 wt% Ru/ZSM-5 has a similar chemical composition and demonstrates a similar catalytic activity due to the presence of the reactive sites in both catalysts and both are commonly used in for catalytic activities under high reaction temperature, suggesting that the 1 wt% Ru/ZSM-5 is efficient under high reaction temperatures.

Although several works of literature have reported on the decomposition of N_2O via the supported silver catalysts, a similar phenomenon was not observed in the present study. The absence of N_2O conversion by the silver-based catalysts could be explained by various factors such as the influence of the active metal(0) species on the catalyst surface, the influence of the catalyst support, the reaction methods and conditions during the catalyst preparation.

Chapter 6

Summary

6 Summary

The present work provides new insights in structural parameters that determine the catalytic performance of supported noble metal catalysts in N_2O decomposition. The investigations focus on (1) the dependency of catalytic performance on support materials (**Chapter 2**); (2) reactivity of N_2O with transition metals (Fe, Ni, Ru, Rh, Pd) supported on CeO_2 (**Chapter 3**); (3) selective catalytic reduction of N_2O with H_2 (**Chapter 4**); (4) influence of light on the decomposition of nitrous oxide (**Chapter 5**).

Catalytic decomposition of N_2O is one of the most suitable methods to reduce the emission of N_2O. In **Chapter 2**, ruthenium on chosen supports (Al_2O_3, SiO_2, Al_2O_3-SiO_2 mixed oxides, $MgAl_2O_4$ spinel, $ZnAl_2O_4$ spinel and AlF_3) as catalysts were synthesized by incipient wetness impregnation with $Ru(NO)(NO_3)_3$ as precursor. The catalysts were characterized by BET surface area determination, X-ray diffraction, chemisorption, temperature-programmed reduction and desorption (TPR/TPD) and in situ infrared spectroscopy (IR) to establish structure–activity relationships. Different chosen support materials for ruthenium catalysts demonstrated an obvious influence on the catalytic activity in N_2O decomposition. This could be explained by varying properties like the metal-support interaction, the dispersion of Ru-active species and structure and modification of the support. The strong Lewis and Brønsted acidic sites in silica-alumina composition do not influence the catalytic performance significantly. On the other hand, basic sites are beneficial for N_2O decomposition. Higher Ru dispersion was observed in the Al_2O_3 rich Ru/SiO_2-Al_2O_3 catalysts. This promoted the stronger metal-support interaction, higher catalytic activity and lower degree of inhibition by gaseous oxygen in the reaction.

N_2O and temperatures of up to 500°C (maximum temperature applied) have no influence on the (short-term) stability of catalyst. Under identical conditions, the pre-oxidized catalysts are more active than the pre-reduced ones, again for the majority of the supports indicating that ruthenium oxide(s) rather than metallic ruthenium act as active species. However, Ru/AlF_3 becomes more active after pre-reduction with decreasing T_{50}

to 375°C. This can be explained by the lack of oxygen in support lattice structure and missing involvement of oxygen from support material in the N_2O decomposition process.

Introduction of O_2 has an inhibitory effect on the N_2O decomposition. This indicates that the active sites are poisoned by oxygen increasing the desorption temperature. $Ru/ZnAl_2O_4$ is found to be the catalyst of highest activity for the decomposition of N_2O. It can achieve nearly 100% N_2O conversion at 500 °C even with presence of excess of O_2 (GHSV = 24000 h^{-2}). This could be due to the formation of particular phase by interaction between Ru and spinel structure.

Supported Rh catalysts are among the most active systems for the N_2O abatement, but suffer from rapid deactivation. Pre-reduction of the catalyst (noble metal and/or transition metal oxide) by H_2 at elevated temperature prior to the catalytic test was found to be a prerequisite for reactivity at room temperature. In addition to Rh catalysts, the **Chapter 3** broadens the scope of catalysts to pre-reduced late transition metals supported on CeO_2, including Ru/CeO_2, Rh/CeO_2, Pd/CeO_2, Ni/CeO_2, and Fe/CeO_2. The outstanding activity of late transition metals supported on CeO_2 catalysts in the abatement N_2O has been successfully demonstrated. The catalysts pre-reduced in hydrogen at 500 °C exhibit high steady-state activities already at room temperature with N_2O for a limited time. Pre-reduced cerium(IV) oxide (surface layers of Ce_2O_3) as well as supported late transition metal nano-particles react efficiently stoichiometrically with N_2O. It was experimentally verified that the highly interesting transformation of N_2O to N_2 at room temperature over pre-reduced CeO_2-based catalysts does not represent a catalytic decomposition of N_2O, but a stoichiometric reduction of N_2O by Ce_2O_3 and transition metals. Transition metal oxides and surface layers of CeO_2 are reduced by H_2 pre-reduction. The reduced sites of CeO_2, i.e. cerium(III) oxide species represent the highly active accessible reducing sites for N_2O at room temperature. The transition metals act as catalysts for the stoichiometric reduction of N_2O by Ce_2O_3 and provide additional reactive sites for N_2O reduction. Metallic transition metals supported on CeO_2

can be oxidized by N_2O at room temperature. The lifetime of the catalysts is determined by the stoichiometric consumption of the supported metals and the Ce_2O_3 layer.

In **Chapter 4**, experiments according to the selective catalytic reduction of nitrous oxide were performed. These experiments were done with noble metals (ruthenium and rhodium) supported on ceria and alumina. Hydrogen was used as reducing agent. It was found that ceria-based catalysts show very good properties in the selective catalytic reduction. A reductive pretreatment is not necessary. The rhodium sample shows full nitrous oxide conversion at room temperature with a (nearly) stoichiometric amount of hydrogen. For alumina supported catalysts, no nitrous oxide conversion is obtained at this temperature. This indicates that the reaction takes place at the interface of the support and the metal. Rh/CeO_2 acts in this case as catalyst for the simultaneous reduction and oxidation of the support. XRD pattern confirmed that the state of the metal does not change during the selective catalytic reduction.

In **Chapter 5**, the influence of light on the catalytic decomposition of N_2O was investigated under different reaction temperatures using supported ruthenium and silver catalysts. Light irradiation imposed a positive influence on the decomposition of N_2O with the supported Ru catalysts. Additionally, the N_2O conversion during the light phase has demonstrated to be increasing with the irradiation time. The increase in N_2O conversion under light irradiation is interpreted as a result of the enhanced photocatalytic properties of the catalyst in the presence of transition metals. Although several works of literature have reported on the decomposition of N_2O via the supported silver catalysts, a similar phenomenon was not observed in the present study.

Chapter 7

Experimental

7.1 Materials

All supports and metal precursors were purchased by commercial suppliers (VWR, Sigma Aldrich, Alfa Aesar) and used without further purification. Gases from Westfalen AG (Germany) were used with a purity of > 99.5% for all gases.

7.1.1 Synthesis of SiO_2-Al_2O_3 mixed oxides

A series of SiO_2-Al_2O_3 mixed oxides containing various percentage of Al_2O_3 (25, 50 and 75 wt%) were prepared by co-hydrolyzing tetraethyl orthosilicate with a solution of desired amount of aluminium nitrate. The mixture of both aluminium and silicon salts, when slowly introduced into a 0.1 M acetic acid solution, gave a homogeneous mixed gel after heating for 15h at about 80°C with vigorous stirring. A second homogenization took place after adjusting and maintaining the pH at 7 by means of ammonia. After aging for 24 h at room temperature, the obtained gel was filtered, followed by washing severally with distilled water and three times with ethanol to remove most of the water. The product was dried sequentially at room temperature for 16 h, at 383 K for 5 h. Finally, the material was calcined in a flow of dry air by increasing the temperature linearly at a ramping rate of 2 K/min to 773 K, and maintaining this temperature for 4 h

7.1.2 Synthesis of pure Al_2F_3

AlF_3 was prepared according to a literature procedure from a former member in the group. In a flask made of perfluoroalkoxy polymer (PFA), 9.18 g of Al_2O_3 (90 mmol) is suspended in 150 mL of water. Twenty-four milliliters of hydrofluoric acid (40%; 540 mmol HF) is added dropwise under vigorous stirring at room temperature and subsequently the solid oxide is dissolved completely. The resulting clear solution is stirred for three days at room temperature. During this period, a white solid precipitates which is separated from the solvent by centrifugation (6000 rpm, 10 min). The resulting white aluminum fluoride is washed 3 times with 5-10 mL of water and dried at 70°C overnight. Subsequently, the material is treated in a muffle furnace for 4 h at the desired calcination temperature.

7.1.3 Catalyst preparation by incipient wetness impregnation

Determination of Water Uptake Volume of the Supports

Water uptake measurements were determined using the pure support material before the impregnation process. The pure supports were stored in a drying oven for two hours for moisture removal to ensure the accuracy of the water uptake measurements. The measurements were done based on 1g sample for each pure support. Water was initially injected in a series of 100µl solution into the support and was eventually added in by a series of 50µl of solution for a better judgement on the water uptake measurements. Measurements were recorded upon the observation of a layer of liquid forming in the support. From these data, the concentration of metal salt solutions for impregnation can be calculated so that catalysts containing the desired amount of metal per weight or bulk volume can be prepared.

Impregnation of the Supported Ruthenium Catalysts

Alumina (Aluminiumoxid C), silica (Aerosil 200) and titania (Aeroxide P25) were purchased from Degussa. Magnesia (MgO Nanopowder) was purchased from Aldrich. Ceria (SNAC-10000) was received from Priem. All metal oxides were agglomerated by suspending in destilled water and drying on a rotary evaporator. The agglomerated materials were sieved into a grain size of 100µm < dg < 300µm and dried at 200°C for 8h. Supported ruthenium catalysts were prepared by incipient wetness impregnation of the sieved and dried metal oxides with aqueous solutions of ruthenium nitrate ($Ru(NO_3)_3$). $Ru(NO)(NO_3)_3$ (c = 1.5wt%) was used as the precursor solution. Dilution was performed accordingly to obtain the required metal loading amount for the different catalysts. The samples were mixed homogeneously using a vortex mixer (Heidolph™ Reax Control Vortex Mixer) upon each addition of the precursor solution.

Impregnation of the Silver-Based Catalysts

Drying of the support materials is also repeated for the synthesis of the supported Ag catalysts. The precursor solution was made using the $AgNO_3$ (99%) solids, and dilution was performed to obtain the desired metal loading amounts for the different catalysts. The mixing of the samples was repeated using the vortex mixer (Heidolph™ Reax Control Vortex Mixer) upon each addition of the precursor solution.

Drying and Calcination of the Impregnated Samples

The impregnated samples were either dried at 120°C for two hours in a muffle furnace (Wisd Laboratory Instruments) with a ramp rate of 10K/min or overnight in a drying oven for the removal of excess water from the catalyst surfaces. Calcination was done in a muffle furnace (Wisd Laboratory Instruments) at 450°C and 200°C for the supported Ru catalysts and supported Ag catalysts respectively for four hours with a ramping rate of 5K/min before storing it for moisture removal.

7.2 Analytical methods

7.2.1 N_2 physisorption

Surface areas of solid materials were determined by single-point N_2 physisorption at a temperature of -196°C and atmospheric pressure on a Quantachrome NovaTouch. All samples were degassed at 300°C for 1h in flowing helium prior to N_2 physisorption. Specific surface areas were calculated from the amount of N_2 desorbed upon rapid sample heating from -196°C to room temperature.

7.2.2 X-ray diffraction

Powder X-ray diffraction (XRD) measurements were performed on a Philips X'Pert Pro diffractometer with a copper anode (K_α = 0.154056 nm). The recorded diffraction angle range was 10-70° on the 2θ scale for wide angle measurements. Reference

diffractograms were taken from the database of the International Center for Diffraction Data (ICDD).

7.2.3 H_2-chemisorption

Chemisorption analysis was carried out on Quantachrome AutosorbiQ. The process was conducted in a vacuum environment. An evacuation was performed for 120 minutes and heated at 300°C at 10K/min. Reduction with H_2 gas was performed for 120 minutes to obtain the active metal species before evacuating for another 120 minutes. The temperature was then decreased to 100°C at the rate of 10K/min before the chemisorption analysis. The measurements were repeated by evacuating for 60 minutes. The chemisorption result was obtained by taking the difference between the two isotherm measurements.

7.2.4 Temperature programmed reactivity

Hydrogen Temperature programmed reduction (H_2-TPR) and oxygen temperature programmed oxidation (O_2-TPO) are measured on a Quantachrome ChemStar TPx equipped with a thermal conductivity detector (TCD). Produced water was removed by a cooling trap filled with a mixture of liquid nitrogen and isopropanol. 500 mg sample were used in per measurement. The hydrogen consumption was calculated by copper(II) oxide calibration. Measurements were done in an U-tube quartz reactor with an inner diameter of 4 mm. All samples were heated in inert gas before TPR and TPR/ TPO measurement (10 K/min, 500 °C, 30 min; 50 mL/min He) to remove surface impurities. H_2-TPR experiments were conducted between room temperature and 800 °C, heating ramp of 10 K/min. The gas glow contains 5 % hydrogen, total gas flow was set to 100 mL/min, argon as balance gas. The WHSV was 12000 $mLg^{-1}h^{-1}$.

For TPR/ TPO experiments the samples were first reduced (10 K/min, 500 °C, 1 h) and subsequently oxidized in syntactic air (10 K/min, 800 °C). The reduction was done in 20 % hydrogen, total gas flow was set to 100 mL/min, argon as balance gas. The oxidation was done in 20 % syntactic air, total gas flow was set to 100 mL/min, helium as balance gas. The WHSV was 12000 $mLg^{-1}h^{-1}$.

7.3 Catalytic measurements

7.3.1 Instrumental setup for catalytic activity tests

A gas mixer allows to adjust the feed gas composition to the experiments specific requirements via four mass flow controllers (MFC). The following gases were usable within the given flow ranges of 0−100 ml/min: He, O_2, H_2 and a mixture of 0.5% N_2O in He.

The effluent gas stream from the reactor or bypass run through the gas flow cell of an FT−IR spectrometer for quantitative analysis.

7.3.2 Construction of an UV/vis irradiated tube furnace

A quartz tube (purchased from QSIL AG, length = 50 cm, inner ø = 30 mm, wall thickness = 1.5 mm) was lagged with a glass fiber isolated heating cord (purchased from Horst GmbH, ø = 3.5mm, heated length = 10m, max. power consumption = 1250W, max. working temperature = 450°C), leaving the central 50 mm and the marginal 50 mm of the tube length uncovered. A thin quartz tube (inner ø = 4 mm, wall thickness = 1mm) covering the full heated length is attached to the outside of the heating cord to provide a cavity for the insertion of a K type thermocouple (purchased from HTM Reetz GmbH). Insulating ceramic fiber mats (purchased from Rath GmbH) are then wrapped around the tube array and fixed with glass fiber strings. In the central area of the tube, a rectangular window (4 x 1.5cm) is cut out of the insulating material, thus exposing the inner quartz

tube. The construction is then covered with a stainless steel jacket, leaving the central window and both ends of the quartz tube uncovered. To avoid a stack-effect when heating the vertically arranged tube furnace, the lower end of the quartz tube is later sealed with a quartz wool plug.

All electrical connections to a temperature controller from HTM Reetz GmbH were installed by the central workshop for electronics at Technische Universität München.

7.3.3 General Test Procedures for the Decomposition Process

The catalytic measurement in the present study involves a series of steps: starting from (i) He pre-treatment, (ii) introduction of feed gas mixture via different mass flow controllers (MFCs), (iii) the decomposition of N_2O and ending with (iv) Fourier-Transform Infrared (FT-IR) analysis of the gases generated from the decomposition process.

Catalytic tests were performed in a fixed bed tube reactor with an inner diameter of 4 mm. The gas lines from the MFCs to the FT-IR spectrometer were pre-treated with helium at the flow rate of 100ml/min to remove potential impurities. The background signal for the FTIR spectrometer was also obtained after the pre-treatment step. The duration of the He pre-treatment varies with the amount of impurities present in the system as well as the gas lines. After the He pre-treatment step, the feed gas mixture at the flow rate of 100ml/min was introduced into the system to initiate the decomposition of N_2O. Feed gas mixtures contained 1000 ppm of N_2O, helium as a balance and optional 5 vol.% of O_2. The measurements were obtained based on the remaining N_2O concentration available in the system after the decomposition process.

Measurements were collected consecutively at the intervals of 5 minutes until steady state conditions were achieved using an FT-IR spectrometer (Agilent, Cary 660 FT-IR Spectrometer).

7.3.4 Photo-assisted N_2O decomposition measurements

500mg of the calcined sample was loaded into the photoreactor. Both ends of the elliptical part of the photoreactor were covered with quartz wool to avoid sample leakage. The He pre-treatment process was performed at room temperature to obtain the background signal for N_2O (approximately 1000ppm).

The decomposition process comprises both the conventional catalytic decomposition (dark phase) and the photocatalytic decomposition (light phase). The measurements were obtained based on the remaining N_2O concentration available in the system after the decomposition process. The activation and termination of the light irradiation were carried out upon reaching a steady state condition for the N_2O concentration in the system.

Upon the collections of the results, the N_2O concentration remaining in the system was being converted into conversion rate (%) and plotted against the experiment duration to observe the various changes in the decomposition of N_2O induced by the presence and absence of light.

The decomposition process was conducted at four different operating temperatures: 0°C, 150°C, 300°C, 400°C for the N_2O decomposition. The reaction temperature was increased to the designated temperature value after each measurement using the temperature-controlled oven (HTM Reetz GmbH) with a ramp rate of 10K/min.

The decomposition of N_2O is also conducted at a specific reaction temperature to observe the influence of light on the decomposition process in details. The operating temperature was maintained for several hours to ensure reproducible results. The operating temperature at which the decomposition process is conducted allows a distinct N_2O conversion rate. The analysis for the light and dark phases were carried out for two cycles to ensure the accuracy of the results obtained.

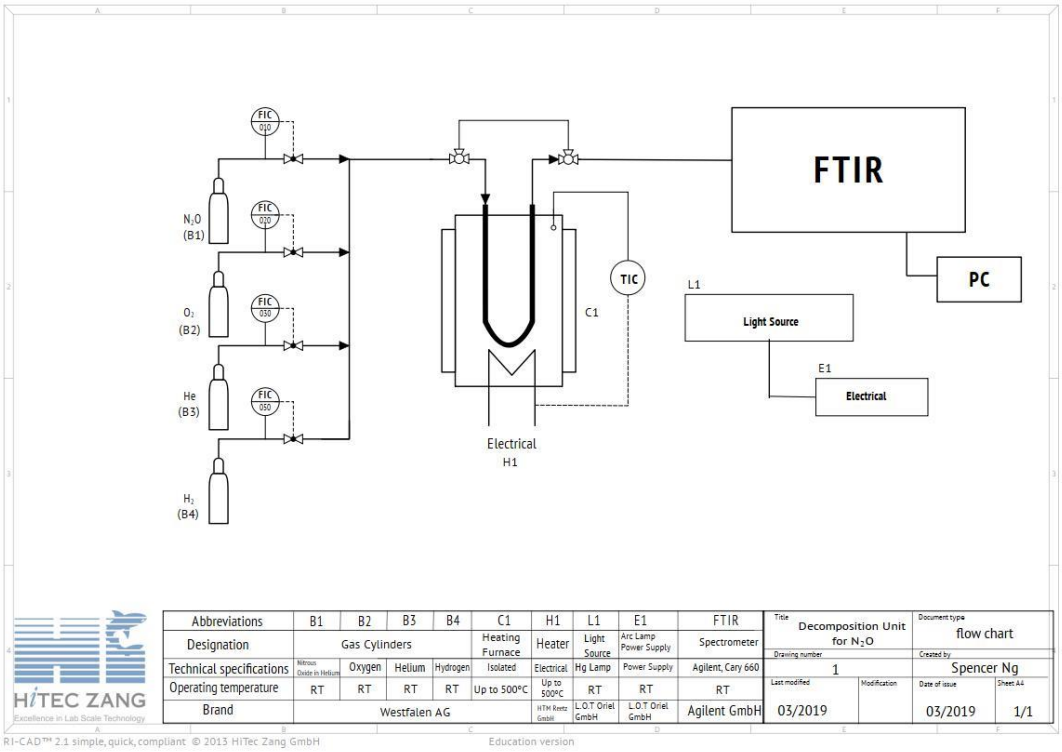

Figure 7.1: Schematic diagram of the N_2O decomposition process

7.3.5 Selective catalytic reduction

For the SCR experiments, hydrogen is introduced as reducing agent during the reaction with nitrous oxide. There are two sets of experiments. In the first one, excess of hydrogen is introduced (2 mL/min, H_2:N_2O = 20:1). In the second one hydrogen is introduced stoichiometric (1500 ppm H_2, H_2:N_2O = 1.5:1). The total flow is 100 mL/min, He as balance gas. Temperature was set between room temperature and 200 °C, 500 mg sample per measurement. The WHSV was 12000 $mLg^{-1}h^{-1}$.

Chapter 8

Appendix

8 Appendix

List of publications

Xiaoqiao Zhang, Jian Zheng, Max Johannes Hiller, Klaus Köhler. "The interplay of various catalyst and reaction parameters in the decomposition of N_2O over supported Ru catalysts" (In Preparation)

Dan Chen, Xiaonan Wang, **Xiaoqiao Zhang**, Yan Yang, Yao Xu, Guangren Qian. "Facile fabrication of mesoporous biochar/$ZnFe_2O_4$ composite with enhanced visible-light photocatalytic hydrogen evolution" International Journal of Hydrogen Energy, 44, 2019: 19967-19977.

Dan Chen, Yan Yang, **Xiaoqiao Zhang**, Xiaonan Wang, Yao Xu, Guangren Qian. "Mesoporous composite $NiCr_2O_4$/Al-MCM-41: A novel photocatalyst for enhanced hydrogen production" International Journal of Hydrogen Energy, 44, 2019: 18123-18133.

Zhou, Jizhi, Simiao Wu, Yun Pan, Lingen Zhang, Zhenbang Cao, **Xiaoqiao Zhang**, Shinichi Yonemochi et al. "Enrichment of heavy metals in fine particles of municipal solid waste incinerator (MSWI) fly ash and associated health risk" Waste management, 43, 2015: 239-246.

Conference contributions

Xiaoqiao Zhang, Klaus Köhler. "The interplay of various catalyst and reaction parameters in the decomposition of N_2O over supported Ru catalyst" Poster Presentation, 26th North American Catalysis Society Meeting, Chicago, Illinois, USA, 2019

Xiaoqiao Zhang, Oliver Thomys, Florian Boch, Patrick Bretzler, Klaus Köhler. " Influence of support and dispersion of ruthenium on the catalytic performance in the decomposition of N_2O" Poster Presentation, 51st German Catalysis Meeting, Weimar, Germany, 2018

Chapter 9

References

9 References

[1] Wiberg, N., *Holleman Wiberg Lehrbuch der Anorganischen Chemie*. Walter de Gruyter & Co: Berlin, **2007**; Vol. 102.

[2] Pérez-Ramírez, J.; Kapteijn, F.; Schöffel, K.; Moulijn, J. A., *Applied Catalysis B: Environmental,* **2003,** 44*,* 117-151.

[3] WMO, *Greenhouse gas bulletin No. 13,* **2017**.

[4] Konsolakis, M., *ACS Catalysis,* **2015,** 5*,* 6397-6421.

[5] Vitousek, P. M.; Aber, J. D.; Howarth, R. W.; Likens, G. E.; Matson, P. A.; Schindler, D. W.; Schlesinger, W. H.; Tilman, D. G., *Ecological applications,* **1997,** 7*,* 737-750.

[6] Thomson, A. J.; Giannopoulos, G.; Pretty, J.; Baggs, E. M.; Richardson, D. J., *Philos Trans R Soc Lond B Biol Sci,* **2012,** 367*,* 1157-68.

[7] Shcherbak, I.; Millar, N.; Robertson, G. P., *Proceedings of the National Academy of Sciences,* **2014,** 111*,* 9199-9204.

[8] Seitzinger, S. P.; Kroeze, C.; Styles, R. V., *Chemosphere-Global Change Science,* **2000,** 2*,* 267-279.

[9] Nevison, C., *Chemosphere-Global Change Science,* **2000,** 2*,* 493-500.

[10] Powers, S. E.; DeWaters, J.; Venczel, M., *Journal of Professional Issues in Engineering Education and Practice,* **2011,** 137*,* 55-63.

[11] Rodrigue, J.-P.; Comtois, C.; Slack, B., *The Geography of Transport Systems. New York: Routledge,* **2013**.

[12] Odaka, M.; Koike, N.; Suzuki, H., *Chemosphere-Global Change Science,* **2000,** 2*,* 413-423.

[13] Granger, P.; Dujardin, C.; Paul, J.-F.; Leclercq, G., *Journal of Molecular Catalysis A: Chemical,* **2005,** 228*,* 241-253.

[14] Nevalainen, P.; Kinnunen, N. M.; Kirveslahti, A.; Kallinen, K.; Maunula, T.; Keenan, M.; Suvanto, M., *Applied Catalysis A: General,* **2018,** 552*,* 30-37.

[15] Schindlbacher, A.; Zechmeister‐Boltenstern, S.; Butterbach‐Bahl, K., *Journal of Geophysical Research: Atmospheres,* **2004,** 109.

[16] Schmidt, M.; Glatzel‐Mattheier, H.; Sartorius, H.; Worthy, D. E.; Levin, I., *Journal of Geophysical Research: Atmospheres,* **2001,** 106*,* 5507-5516.

[17] Pérez-Ramírez, J.; Kapteijn, F.; Mul, G.; Moulijn, J., *Chemical Communications,* **2001,** 693-694.

[18] Konsolakis, M.; Yentekakis, I.; Pekridis, G.; Kaklidis, N.; Psarras, A.; Marnellos, G., *Applied Catalysis B: Environmental,* **2013,** 138*,* 191-198.

[19] Van den Brink, R.; Booneveld, S.; Pels, J.; Bakker, D.; Verhaak, M., *Applied Catalysis B: Environmental,* **2001,** 32*,* 73-81.

[20] Melián-Cabrera, I.; Mentruit, C.; Pieterse, J.; van den Brink, R.; Mul, G.; Kapteijn, F.; Moulijn, J., *Catalysis Communications,* **2005,** 6*,* 301-305.

[21] Kustov, L.; Tarasov, A.; Bogdan, V.; Tyrlov, A.; Fulmer, J., *Catalysis today,* **2000,** 61*,* 123-128.

[22] Bulánek, R.; Novoveská, K., *Reaction Kinetics and Catalysis Letters,* **2003,** 80*,* 337-343.

[23] Chen, M.; Wu, J.-L.; Liu, Y.-M.; Cao, Y.; Fan, K.-N., *Catalysis Communications,* **2011,** 12*,* 1063-1066.

[24] Langfeld, K.; Frank, B.; Strempel, V. E.; Berger-Karin, C.; Weinberg, G.; Kondratenko, E. V.; Schomäcker, R., *Applied Catalysis A: General,* **2012,** 417*,* 145-152.

[25] Shimizu, A.; Tanaka, K.; Fujimori, M., *Chemosphere-Global Change Science,* **2000,** 2*,* 425-434.

[26] Pérez-Ramırez, J.; Kapteijn, F.; Schöffel, K.; Moulijn, J., *Applied Catalysis B: Environmental,* **2003,** 44*,* 117-151.

[27] Russo, N.; Mescia, D.; Fino, D.; Saracco, G.; Specchia, V., *Industrial & engineering chemistry research,* **2007,** 46*,* 4226-4231.

[28] Pérez-Ramırez, J.; Kapteijn, F.; Groen, J.; Doménech, A.; Mul, G.; Moulijn, J., *Journal of Catalysis,* **2003,** 214*,* 33-45.

[29] Galle, M.; Agar, D.; Watzenberger, O., *Chemical Engineering Science,* **2001,** 56*,* 1587-1595.

[30] Lee, S.-J.; Ryu, I.-S.; Kim, B.-M.; Moon, S.-H., *International Journal of Greenhouse Gas Control,* **2011,** 5*,* 167-176.

[31] Zeng, H. C.; Pang, X. Y., *Applied Catalysis B: Environmental,* **1997,** 13*,* 113-122.

[32] A. Reimer, R.; S. Slaten, C.; Seapan, M.; W. Lower, M.; E. Tomlinson, P., *Abatement of N2O Emissions Produced in the Adipic Acid Industry*. **1994**; Vol. 13, p 134-137.

[33] Andreini, A.; Facchini, B.; Mangani, L.; Asti, A.; Ceccherini, G.; Modi, R. In *NOx Emissions Reduction In An Innovative Industrial Gas Turbine Combustor (GE10 Machine): A Numerical Study Of The Benefits Of A New Pilot-System On Flame Structure And Emissions*, ASME Turbo Expo 2005: Power for Land, Sea, and Air, American Society of Mechanical Engineers: 2005; pp 235-247.

[34] Eckard, R.; Grainger, C.; De Klein, C., *Livestock science,* **2010,** 130*,* 47-56.

[35] Hu, X.; Zhang, J.-J.; Mukhnahallipatna, S.; Hamann, J.; Biggs, M. J.; Agarwal, P., *Fuel,* **2003,** 82*,* 1675-1684.

[36] Komvokis, V. G.; Marti, M.; Delimitis, A.; Vasalos, I. A.; Triantafyllidis, K. S., *Applied Catalysis B: Environmental,* **2011,** 103*,* 62-71.

[37] Reddy, P. S. S.; Pasha, N.; Rao, M. C.; Lingaiah, N.; Suryanarayana, I.; Prasad, P. S., *Catalysis Communications,* **2007,** 8*,* 1406-1410.

[38] Komvokis, V. G.; Marnellos, G. E.; Vasalos, I. A.; Triantafyllidis, K. S., *Applied Catalysis B: Environmental,* **2009,** 89*,* 627-634.

[39] Marnellos, G. E.; Efthimiadis, E. A.; Vasalos, I. A., *Applied Catalysis B: Environmental,* **2003,** 46*,* 523-539.

[40] Pasha, N.; Lingaiah, N.; Babu, N. S.; Reddy, P. S. S.; Prasad, P. S., *Catalysis Communications,* **2008,** 10*,* 132-136.

[41] Piskorz, W.; Zasada, F.; Stelmachowski, P.; Kotarba, A.; Sojka, Z., *Catalysis today,* **2008,** 137*,* 418-422.

[42] Stelmachowski, P.; Maniak, G.; Kotarba, A.; Sojka, Z., *Catalysis Communications,* **2009,** 10*,* 1062-1065.

[43] Shen, Q.; Li, L.; He, C.; Zhang, X.; Hao, Z.; Xu, Z., *Asia‐Pacific Journal of Chemical Engineering,* **2012,** 7*,* 502-509.

[44] Ma, J.; Rodriguez, N.; Vannice, M.; Baker, R., *Topics in Catalysis,* **2000,** 10*,* 27-38.

[45] Dandekar, A.; Vannice, M., *Applied Catalysis B: Environmental,* **1999,** 22*,* 179-200.

[46] Yuzaki, K.; Yarimizu, T.; Ito, S.-I.; Kunimori, K., *Catalysis letters,* **1997,** 47*,* 173-175.

[47] Huang, C.; Ma, Z.; Xie, P.; Yue, Y.; Hua, W.; Gao, Z., *Journal of Molecular Catalysis A: Chemical,* **2015,** 400*,* 90-94.

[48] Haber, J.; Machej, T.; Janas, J.; Nattich, M., *Catalysis today,* **2004,** 90*,* 15-19.

[49] Centi, G.; Dall'Olio, L.; Perathoner, S., *Journal of Catalysis,* **2000,** 192*,* 224-235.

[50] Shimizu, A.; Tanaka, K.; Fujimori, M., *Chemosphere - Global Change Science,* **2000,** 2*,* 425-434.

[51] Labhsetwar, N.; Dhakad, M.; Biniwale, R.; Mitsuhashi, T.; Haneda, H.; Reddy, P.; Bakardjieva, S.; Subrt, J.; Kumar, S.; Kumar, V., *Catalysis today,* **2009,** 141*,* 205-210.

[52] Boissel, V.; Tahir, S.; Koh, C. A., *Applied Catalysis B: Environmental,* **2006,** 64*,* 234-242.

[53] Panagiotopoulou, P.; Kondarides, D. I., *Catalysis today,* **2006,** 112*,* 49-52.

[54] Fuente, A.; Pulgar, G.; González, F.; Pesquera, C.; Blanco, C., *Applied Catalysis A: General,* **2001,** 208*,* 35-46.

[55] Escandon, L. S.; Ordonez, S.; Vega, A.; Dıez, F. V., *Chemosphere,* **2005,** 58*,* 9-17.

[56] Gurrath, M.; Kuretzky, T.; Boehm, H.; Okhlopkova, L.; Lisitsyn, A.; Likholobov, V., *Carbon,* **2000,** 38*,* 1241-1255.

[57] Dacquin, J.-P.; Dujardin, C.; Granger, P., *Catalysis today,* **2008,** 137*,* 390-396.

[58] Doi, K.; Wu, Y. Y.; Takeda, R.; Matsunami, A.; Arai, N.; Tagawa, T.; Goto, S., *Applied Catalysis B: Environmental,* **2001,** 35*,* 43-51.

[59] Maniak, G.; Stelmachowski, P.; Stanek, J. J.; Kotarba, A.; Sojka, Z., *Catalysis Communications,* **2011,** 15*,* 127-131.

[60] Abu-Zied, B.; Bawaked, S.; Kosa, S.; Schwieger, W., *Catalysts,* **2016,** 6*,* 70.

[61] Abu-Zied, B. M.; Asiri, A. M., *Chinese Journal of Catalysis,* **2015,** 36*,* 1837-1845.

[62] Liu, Z.; He, F.; Ma, L.; Peng, S., *Catalysis Surveys from Asia,* **2016,** 20*,* 121-132.Liu2016

[63] Beyer, H.; Emmerich, J.; Chatziapostolou, K.; Köhler, K., *Applied Catalysis A: General,* **2011,** 391*,* 411-416.

[64] Huang, C.; Jiang, Y.; Ma, Z.; Xie, P.; Lin, Y.; Meng, T.; Miao, C.; Yue, Y.; Hua, W.; Gao, Z., *Journal of Molecular Catalysis A: Chemical,* **2016,** 420*,* 73-81.

[65] Zheng, J.; Meyer, S.; Köhler, K., *Applied Catalysis A: General,* **2015,** 505*,* 44-51.

[66] Pinna, F.; Scarpa, M.; Strukul, G.; Guglielminotti, E.; Boccuzzi, F.; Manzoli, M., *Journal of Catalysis,* **2000,** 192*,* 158-162.

[67] Zabilskiy, M.; Djinović, P.; Tchernychova, E.; Tkachenko, O. P.; Kustov, L. M.; Pintar, A., *ACS Catalysis,* **2015,** 5*,* 5357-5365.

[68] Chang, Y. F.; McCarty, J. G.; Wachsman, E. D.; Wong, V. L., *Applied Catalysis B: Environmental,* **1994,** 4*,* 283-299.

[69] Chang, Y.-f.; McCarty, J. G.; Wachsman, E. D., *Applied Catalysis B: Environmental,* **1995,** 6*,* 21-33.

[70] Tolman, W. B., *Angewandte Chemie International Edition,* **2010,** 49*,* 1018-1024.

[71] Sugiura, M.; Ozawa, M.; Suda, A.; Suzuki, T.; Kanazawa, T., *Bulletin of the Chemical Society of Japan,* **2005,** 78*,* 752-767.

[72] Boaro, M.; De Leitenburg, C.; Dolcetti, G.; Trovarelli, A., *Journal of Catalysis,* **2000,** 193*,* 338-347.

[73] Imagawa, H.; Suda, A.; Yamamura, K.; Sun, S., *The Journal of Physical Chemistry C,* **2011,** 115*,* 1740-1745.

[74] Centi, G.; Dall'Olio, L.; Perathoner, S., *Catalysis letters,* **2000,** 67*,* 107-112.

[75] Imamura, S.; Tadani, J.-i.; Saito, Y.; Okamoto, Y.; Jindai, H.; Kaito, C., *Applied Catalysis A: General,* **2000,** 201*,* 121-127.

[76] Ravishankara, A.; Daniel, J. S.; Portmann, R. W., *Science,* **2009,** 326*,* 123-125.

[77] Olivier, J. G.; Van Aardenne, J. A.; Dentener, F. J.; Pagliari, V.; Ganzeveld, L. N.; Peters, J. A., *Environmental Sciences,* **2005,** 2*,* 81-99.

[78] Cho, C.-M.; Watanabe, Y.; Nunotani, N.; Imanaka, N., *Chemistry Letters,* **2018,** 47*,* 996-999.

[79] Lim, J. B.; Cha, S. H.; Hong, S. B., *Applied Catalysis B: Environmental,* **2019,** 243*,* 750-759.

[80] Kaczmarczyk, J.; Zasada, F.; Janas, J.; Indyka, P.; Piskorz, W.; Kotarba, A.; Sojka, Z., *ACS Catalysis,* **2016,** 6*,* 1235-1246.

[81] Sui, C.; Yuan, F.; Zhang, Z.; Zhang, C.; Niu, X.; Zhu, Y., *Catalysts,* **2016,** 6*,* 173.

[82] Zahaf, R.; Jung, J. W.; Coker, Z.; Kim, S.; Choi, T.-Y.; Lee, D., *Aerosol Air Qual. Res,* **2015,** 15*,* 2409-2421.

[83] Tzitzios, V.; Georgakilas, V., *Chemosphere,* **2005,** 59*,* 887-891.

[84] Arenas-Alatorre, J.; Gómez-Cortés, A.; Avalos-Borja, M.; Díaz, G., *The Journal of Physical Chemistry B,* **2005,** 109*,* 2371-2376.

[85] Crépeau, G.; Montouillout, V.; Vimont, A.; Mariey, L.; Cseri, T.; Maugé, F., *The Journal of Physical Chemistry B,* **2006,** 110*,* 15172-15185.

[86] Hensen, E.; Poduval, D.; Magusin, P.; Coumans, A.; Van Veen, J., *Journal of Catalysis,* **2010,** 269*,* 201-218.

[87] Xu, B.; Sievers, C.; Lercher, J. A.; Van Veen, J. R.; Giltay, P.; Prins, R.; Van Bokhoven, J. A., *The Journal of Physical Chemistry C,* **2007,** 111*,* 12075-12079.

[88] Hensen, E. J.; Poduval, D. G.; Degirmenci, V.; Ligthart, D. J. M.; Chen, W.; Maugé, F. o.; Rigutto, M. S.; Veen, J. R. v., *The Journal of Physical Chemistry C,* **2012,** 116*,* 21416-21429.

[89] Kleist, W.; Haeßner, C.; Storcheva, O.; Köhler, K., *Inorganica chimica acta,* **2006,** 359*,* 4851-4854.

[90] Haeßner, C.; Müller, B.; Storcheva, O.; Köhler, K., *ChemCatChem,* **2013,** 5*,* 3260-3268.

[91] Beyer, H.; Köhler, K., *Applied Catalysis B: Environmental,* **2010,** 96*,* 110-116.

[92] Leonard, A.; Ratnasamy, P.; Declerck, F.; Fripiat, J., *Discussions of the Faraday Society,* **1971,** 52*,* 98-108.

[93] Mardkhe, M. K.; Keyvanloo, K.; Bartholomew, C. H.; Hecker, W. C.; Alam, T. M.; Woodfield, B. F., *Applied Catalysis A: General,* **2014,** 482*,* 16-23.

[94] Phongsawat, W.; Netiworaruksa, B.; Suriye, K.; Praserthdam, P.; Panpranot, J., *Catalysis letters,* **2012,** 142*,* 1141-1149.

[95] Zheng, J. Adsorption and Reactions of COx and NOx Molecules on Heterogeneous Catalysts: Reactivity and in Situ FTIR Spectroscopy Studies. Technische Universität München, 2014.

[96] Lin, Y.; Meng, T.; Ma, Z., *Journal of Industrial and Engineering Chemistry,* **2015,** 28*,* 138-146.

[97] Liu, H.; Ma, Z., *Frontiers of Chemical Science and Engineering,* **2017,** 11*,* 586-593.

[98] Delahay, G.; Coq, B.; Kieger, S.; Neveu, B., *Catalysis today,* **1999,** 54*,* 431-438.

[99] Abu-Zied, B.; Soliman, S., *Catalysis letters,* **2009,** 132*,* 299.

[100] Amrousse, R.; Tsutsumi, A.; Bachar, A., *Catalysis Science & Technology,* **2013,** 3*,* 576-579.

[101] Held, A.; Kowalska-Kuś, J.; Łapiński, A.; Nowińska, K., *Journal of Catalysis,* **2013,** 306*,* 1-10.

[102] Tanaka, S.-i.; Yuzaki, K.; Ito, S.-i.; Kameoka, S.; Kunimori, K., *Journal of Catalysis,* **2001,** 200*,* 203-208.

[103] Parres-Esclapez, S.; Illán-Gómez, M.; De Lecea, C. S.-M.; Bueno-López, A., *Applied Catalysis B: Environmental,* **2010,** 96*,* 370-378.

[104] Wiśniewski, M., *Catalysis letters,* **2014,** 144*,* 633-638.

[105] Hinrichsen, O.; Genger, T.; Muhler, M., *Chemical Engineering & Technology: Industrial Chemistry ‐ Plant Equipment ‐ Process Engineering ‐ Biotechnology,* **2000,** 23*,* 956-959.

[106] Ewald, S.; Standl, S.; Hinrichsen, O., *Applied Catalysis A: General,* **2018,** 549*,* 93-101.

[107] Rynkowski, J. M.; Paryjczak, T.; Lewicki, A.; Szynkowska, M. I.; Maniecki, T. P.; Jóźwiak, W. K., *Reaction Kinetics and Catalysis Letters,* **2000,** 71*,* 55-64.

[108] Imamura, S.; Taniguchi, Y.-i.; Ikeda, Y.; Hosokawa, S.; Kanai, H.; Ando, H., *Reaction Kinetics and Catalysis Letters,* **2002,** 76*,* 201-206.

[109] Luo, X.; Wang, R.; Ni, J.; Lin, J.; Lin, B.; Xu, X.; Wei, K., *Catalysis letters,* **2009,** 133*,* 382.

[110] Zhu, H.; Qin, Z.; Shan, W.; Shen, W.; Wang, J., *Journal of Catalysis,* **2004,** 225*,* 267-277.

[111] Gupta, N.; Kamble, V.; Iyer, R.; Thampi, K. R.; Gratzel, M., *Journal of Catalysis,* **1992,** 137*,* 473-486.

[112] Pilling, N., *J. Inst. Met.,* **1923,** 29*,* 529-582.

[113] Davis, J. R., *ASM specialty handbook: heat-resistant materials*. Asm International: **1997**.

[114] Klabunde, K. J.; Stark, J.; Koper, O.; Mohs, C.; Park, D. G.; Decker, S.; Jiang, Y.; Lagadic, I.; Zhang, D., *The Journal of Physical Chemistry,* **1996,** 100*,* 12142-12153.

[115] Busca, G.; Lietti, L.; Ramis, G.; Berti, F., *Applied Catalysis B: Environmental,* **1998,** 18*,* 1-36.

[116] Li, J.; Chang, H.; Ma, L.; Hao, J.; Yang, R. T., *Catalysis Today,* **2011,** 175*,* 147-156.

[117] Topsøe, N.-Y., *Science,* **1994,** 265*,* 1217-1219.

[118] Boubnov, A.; Carvalho, H. W. P.; Doronkin, D. E.; Günter, T.; Gallo, E.; Atkins, A. J.; Jacob, C. R.; Grunwaldt, J.-D., *Journal of the American Chemical Society,* **2014,** 136*,* 13006-13015.

[119] Kayhanian, M., *Environmental Technology,* **1999,** 20*,* 355-365.

[120] Koebel, M.; Elsener, M.; Kleemann, M., *Catalysis today,* **2000,** 59*,* 335-345.

[121] Chen, L.; Li, J.; Ge, M.; Zhu, R., *Catalysis today,* **2010,** 153*,* 77-83.

[122] Girard, J.; Cavataio, G.; Snow, R.; Lambert, C., *SAE International Journal of Fuels and Lubricants,* **2009,** 1*,* 603-610.

[123] Sitshebo, S.; Tsolakis, A.; Theinnoi, K., *international journal of hydrogen energy,* **2009,** 34*,* 7842-7850.

[124] Sazama, P.; Čapek, L.; Drobná, H.; Sobalik, Z.; Dědeček, J.; Arve, K.; Wichterlová, B., *Journal of Catalysis,* **2005,** 232*,* 302-317.

[125] Shibata, J.; Hashimoto, M.; Shimizu, K.-i.; Yoshida, H.; Hattori, T.; Satsuma, A., *The Journal of Physical Chemistry B,* **2004,** 108*,* 18327-18335.

[126] Fujishima, A.; Honda, K., *nature,* **1972,** 238*,* 37.

[127] Ibhadon, A.; Fitzpatrick, P., *Heterogeneous Photocatalysis: Recent Advances and Applications*. **2013**; Vol. 3, p 189-218.

[128] Beyer, H. Activation of nitrogen oxides by supported noble metal catalysts: Structure-activity relationships. Technische Universität München, 2010.

[129] Lim, T. H.; Jeong, S. M.; Kim, S. D.; Gyenis, J., *Journal of Photochemistry and Photobiology A: Chemistry,* **2000,** 134*,* 209-217.

[130] Kočí, K.; Krejčíková, S.; Šolcová, O.; Obalová, L., *Photocatalytic decomposition of N2O on Ag-TiO2*. **2012**; Vol. 191, p 134–137.

[131] Cunningham, J.; Kelly, J. J.; Penny, A. L., *The Journal of Physical Chemistry,* **1971,** 75*,* 617-625.

[132] Obalová, L.; Reli, M.; Lang, J.; Matějka, V.; Kukutschová, J.; Lacný, Z.; Kočí, K., *Catalysis Today,* **2013,** 209*,* 170-175.

[133] Sano, T.; Negishi, N.; Mas, D.; Takeuchi, K., *Journal of Catalysis,* **2000,** 194*,* 71-79.

[134] Matsuoka, M.; Ju, W.-S.; Anpo, M., *Photocatalytic Decomposition of N2O into N2 and O2 on the Silver(I) Ion-Exchanged ZSM-5 Catalyst*. **2000**; p 626-627.

[135] Kudo, A.; Nagayoshi, H., *Photocatalytic reduction of N2O on metal-supported TiO2 powder at room temperature in the presence of H2O and CH3OH vapor*. **1998**; Vol. 52, p 109-111.

[136] Ouyang, W.; Muñoz-Batista, M. J.; Kubacka, A.; Luque, R.; Fernández-García, M., *Applied Catalysis B: Environmental,* **2018,** 238*,* 434-443.

[137] Ohzu, S.; Ishizuka, T.; Hirai, Y.; Fukuzumi, S.; Kojima, T., *Chemistry – A European Journal,* **2013,** 19*,* 1563-1567.

[138] Subramanian, V.; Wolf, E. E.; Kamat, P. V., *Journal of the American Chemical Society,* **2004,** 126*,* 4943-4950.

[139] Jakob, M.; Levanon, H.; Kamat, P. V., *Nano Letters,* **2003,** 3*,* 353-358.

[140] Khan, M. R.; Chuan, T. W.; Yousuf, A.; Chowdhury, M. N. K.; Cheng, C. K., *Catalysis Science & Technology,* **2015,** 5*,* 2522-2531.

[141] Wang, H.; Zhang, L.; Chen, Z.; Hu, J.; Li, S.; Wang, Z.; Liu, J.; Wang, X., *Chemical Society Reviews,* **2014,** 43*,* 5234-5244.

[142] Chiarello, G. L.; Aguirre, M. H.; Selli, E., *Journal of Catalysis,* **2010,** 273*,* 182-190.

[143] Yoshida, H.; Kato, Y.; Hattori, T., Photoinduced non-oxidative methane coupling over silica-alumina. In *Studies in Surface Science and Catalysis*, Elsevier: **2000**; Vol. 130, pp 659-664.

[144] Yilmaz, B.; Müller, U., *Topics in Catalysis,* **2009,** 52*,* 888-895.

[145] Ardagh, M. A.; Bo, Z.; Nauert, S. L.; Notestein, J. M., *ACS Catalysis,* **2016,** 6*,* 6156-6164.

[146] Sastre, F.; Puga, A. V.; Liu, L.; Corma, A.; García, H., *Journal of the American Chemical Society,* **2014,** 136*,* 6798-6801.

[147] Ip, T. T.-L. Influence of particle size distribution on fluidized bed hydrodynamics. University of British Columbia, 1988.

[148] Hinrichsen, K.-O., Chemical Engineering Principles (CEP 02): Fluidization [PowerPoint slides]. Lecture Notes ed.; München, T. U., Ed. 2017; pp 27-28.

[149] Hinrichsen, K.-O., Fluidization and Pneumatic Transport [PowerPoint slides]. Lecture notes ed.; München, T. U., Ed. 2018; p 9.

[150] Hinrichsen, K.-O., Fluidization and Pneumatic Transport [PowerPoint slides]. Lecture notes ed.; München, T. U., Ed. 2018; p 8.

[151] Huang, C.-P.; Stumm, W., *Surface Science,* **1972,** 32*,* 287-296.

[152] Huang, F.; Yan, A.; Zhao, H., Influences of Doping on Photocatalytic Properties of TiO2 Photocatalyst. **2016**.

[153] Bickley, R. I.; Gonzalez-Carreno, T.; Lees, J. S.; Palmisano, L.; Tilley, R. J., *Journal of Solid State Chemistry,* **1991,** 92*,* 178-190.

[154] Gouma, P. I.; Mills, M. J., *Journal of the American Ceramic Society,* **2001,** 84*,* 619-622.

[155] Kim, A.; Debecker, D.; Devred, F.; Dubois, V.; Sanchez, C.; Sassoye, C., *CO 2 methanation on Ru/TiO 2 catalysts: On the effect of mixing anatase and rutile TiO 2 supports*. **2017**; Vol. 220.

[156] Zhang, H.; Wang, G.; Chen, D.; Lv, X.; Li, J., *Chemistry of Materials,* **2008,** 20*,* 6543-6549.

[157] Hanaor, D. A. H.; Sorrell, C. C., *Journal of Materials Science,* **2011,** 46*,* 855-874.

[158] Minero, C., Surface-Modified Photocatalysts. **2013**.

[159] Beyer, H. Activation of nitrogen oxides by supported noble metal catalysts: Structure-activity relationships. Unpublished Dissertation, TECHNISCHE UNIVERSITÄT MÜNCHEN, 2010.

[160] Zhang, F.; Cheng, Z.; Kang, L.; Cui, L.; Liu, W.; Xu, X.; Hou, G.; Yang, H., *RSC Advances,* **2015,** 5*,* 32088-32091.